Hybridization, Antiferromagnetism, and Hidden Order in URu_2Si_2: Electrodynamics of a Heavy Fermion Material

HYBRIDIZATION, ANTIFERROMAGNETISM, AND HIDDEN ORDER IN URu_2Si_2: ELECTRODYNAMICS OF A HEAVY FERMION MATERIAL

BY

JESSE S. HALL, B.Sc.

A THESIS
SUBMITTED TO THE DEPARTMENT OF PHYSICS & ASTRONOMY
AND THE SCHOOL OF GRADUATE STUDIES
OF MCMASTER UNIVERSITY
IN PARTIAL FULFILMENT OF THE REQUIREMENTS
FOR THE DEGREE OF
DOCTOR OF PHILOSOPHY

Doctor of Philosophy (2015)
(Physics & Astronomy)

McMaster University
Hamilton, Ontario, Canada

TITLE:	Hybridization, Antiferromagnetism, and Hidden Order in URu_2Si_2: Electrodynamics of a Heavy Fermion Material
AUTHOR:	Jesse S. Hall B.Sc., (Honours Physics) University of Ottawa, Ottawa, Canada
SUPERVISOR:	Dr. Tom Timusk
NUMBER OF PAGES:	xvii, 135

For Nathan Cirillo, Justin Stark, and the One Hundred Fifty-Eight. They shall grow not old, but we will remember them.

Abstract

Infrared spectroscopy has been used to study URu_2Si_2. This heavy fermion material exhibits novel behaviour including a phase transition with an unknown order parameter. In spite of many years of study using numerous experimental techniques and theoretical modelling, the nature of this ordering transition remains elusive.

Optical spectroscopy has been applied to study the scattering mechanism of the quasiparticles in the coherent state above the transition. It is found that the scattering is incoherent above the hybridization temperature and gradually develops a Drude peak as the temperature is lowered into the coherent regime. As the temperature approaches the transition from above, the scattering is almost entirely Fermi liquid in character. It is observed that the scaling between the frequency and temperature terms in the Fermi liquid region is anomalous and diverges from the predicted value of 4, with profound implications for the nature of Fermi liquid behaviour generally.

Infrared spectra also clearly show the charge gap in the ordered state. It is found that the gap is anisotropic, with a different character in the c-axis than in the ab-plane of the tetragonal crystal, and that a second small gap appears at lower temperature in the c-axis. The gap does not have a mean-field temperature dependence. The gap is well-modelled by a Dynes density of states with case I coherence factors, typical of a nesting-induced incommensurate density wave.

Doping induces antiferromagnetism in place of the hidden order, and at higher temperatures, which is also studied by spectroscopy. It is found that the Fermi liquid temperature region rises in temperature in tandem with the phase transition, so that the transition is always preceded by Fermi liquid behaviour but with anomalous scaling between frequency and temperature. The character of the charge gap does not change between the hidden order and antiferromagnetic states, indicating that the same mechanism is responsible for the charge gap in both phases.

Acknowledgements

No man is an island, entire unto itself. Throughout the course of my studies at McMaster, I have been greatly assisted by the stimulating environment of the department of physics and the people within it, as well as the people around the world with whom I have been extremely fortunate to have had the opportunity to work on and discuss the material that has ultimately formed the contents of this thesis.

At McMaster, Sarah Purdy took me under her wing and showed me the ropes in the lab, teaching me how to use the equipment and carry out experiments as well as the basics of social interaction among students that were lost on me after returning from Afghanistan so recently. Dr. Paul Dube has been enormously helpful in supplying liquid helium for measurements at low temperature, assistance with repairs and maintenance of equipment, and additional measurements of magnetization using a SQUID and resistivity using a highly temperamental Oxford Maglab PPMS. Alison Kinross performed measurements and helped with lab work that directly contributed to this thesis. Mahsa Rahimi Movassagh did many of the measurements of DC resistivity that are included herein, and her work in the lab and analysis of the data were important contributions to these projects.

International collaborations have made a huge contribution to the success of this work. In particular, the team at the National Institute for Chemical Physics and

Biophysics in Tallinn, Estonia, has provided state of the art facilities and unparalleled experimental expertise as well as patience and hard work that forms the heart of much of this work. Taaniel Uleksin, Urmas Nagel, and Toomas Rõõm worked tirelessly and provided hospitality and support during my many visits throughout the course of my studies. Ricardo Lobo of the ESPCI (confirm) provided measurements, a tour of his facilities, and some very pleasant French cuisine on the occasions I was lucky enough to visit Paris. Pascale Roy at Synchrotron Soleil has been extremely kind and collaborating with her and her team, Jean-Blaise Brubach and Maxime Somethingorother, has been a personal pleasure as well as a professional joy.

The staff at McMaster have likewise assisted greatly in the process of completing this work. The Graduate Secretary Liz Penney, who has since moved on, provided important administrative support without which the process of becoming and remaining a graduate student would have been much more tiresome. The office staff in the department, Cheryl, Tina, Mara, and Rosemary, have similarly kept me in good standing with the various administrative requirements of the powers that be, despite my sometimes less-than-cooperative attention to deadlines. The graduate chairs, Kari Dalnoki-Veress, who made my admission to the university possible and tolerated my need for advice on the program with what now seems like impressive grace, and Alison Sills, who made what would otherwise have been a difficult and embarrassing circumstance into smooth sailing, each helped me out of difficult situations in ways I cant properly express gratitude for.

Hanna Dabkowska and Antoni Dabkowski have both been enormously supportive with their expertise and equipment for sample growth and characterization. Travis Williams, Murray Wilson, and Graeme Luke supplied many of the samples used in the experiments reported herein, as well as important discussions and insights that might otherwise have been overlooked. Marek Kiela is something of an electronics superhero, and his advice and assistance with the equipment has been invaluable. Scott Culbert and Katelyn Dixon both contributed to the lab work by machining parts and maintaining equipment.

Throughout much of my time at McMaster, I have been a reservist at the Argyll and Sutherland Highlanders of Canada (Princess Louise's), and this has provided me a second home and a social connection to the city of Hamilton that I would not otherwise have had. The regiment has been very supportive throughout my program at McMaster and deserves recognition for its commitment to excellence within the military and without. The people I have worked with are too numerous to name, but I owe special thanks to Sgt John Donachie, my first platoon WO in the unit and the course 2i/c of the basic reconnaissance course, for bending over backwards to accommodate my increasingly ridiculous scheduling requirements. WO Glenn Seddon has been running the shooting team and given me the opportunity to improve my marksmanship and compete provincially and nationally in marksmanship. Capt Chris Finbow has been extremely helpful in supporting me and helping me balance my civilian commitments, personal life, and the military. WO Sargon Sarkis has been an outstanding example of everything a non-commissioned officer should be, and I have been fortunate to work under him and benefit from his attitude and dedication. Cpl Alan Murphy and Cpl Abil Tokhai have become among my closest friends, and they've helped keep me grounded and sane throughout the more difficult times, not to mention driving me to the airport for my various trips for experiments and conferences.

My friends and family have been an important source of support throughout my time in the graduate program. Ronan Drysdale, with whom I've been friends for well over twenty years now, is still the closest thing I have to a brother. We've punched each other in the head more times than I can count (possibly on account of the punching), and always go out for pizza afterwards. He keeps me on track with training and in shape, lest he finally defeat me in glorious combat and take back the other half of his soul. Krista Walsh has been a truer friend than I could have asked or hoped for, and has been a great help in keeping me sane throughout the PhD program. Sarah Purdy has been my partner in suffering and adversity pretty much the whole way along, as well as someone that provides the invaluable service of telling me when I'm wrong.

My parents have both been incredibly supportive of me throughout my studies. Possibly, this is because the alternative was a military career and they were eager to keep me away from bullets. My father is always available to help out and chat about things, and his experience and wisdom have both been invaluable. My mother is a wonderful person, and she is as supportive and attentive and kind as anyone I've ever known. My wife, Sadie, has been nothing short of perfect. She is the sweetest and most disarmingly selfless person I can even imagine. Her sense of adventure, her practicality, her intelligence, and her determination have been both an inspiration and a pillar of support. Seeing her move to a new city and start her own business right out school has kept me determined and dedicated, and reminded me that as challenging as a doctorate in physics undoubtedly is, there are harder things in life waiting for me once I finish. And she gave me a beautiful healthy son, so that was nice.

Finally, my supervisor, Tom Timusk, without whom none of the things I have done would have been possible. He has always had time to give me advice, and he has consistently approached me with opportunities to attend conferences or travel for research. Under his auspices I've visited Japan, Estonia, France, and the United States. He has never questioned my ability to overcome challenges or problems and I hope I have rewarded the trust that he has placed in me.

Contents

List of Figures

Chapter 1

Introduction and Problem Statement

This thesis presents the work I have done in pursuit of the degree of Doctor of Philosophy in Physics at the most esteemed and honourable institution of McMaster University. It is primarily focused on presenting the data acquired using optical spectroscopy on the heavy fermion compound URu_2Si_2as well as describing the techniques of infrared spectroscopy. It is designed as a sandwich thesis, in which manuscripts either published or in the process of wending their way thence are included as the body between introductory and concluding chapters.

1.1 Hidden order in URu_2Si_2

Phase transitions are a subject of continuing interest in condensed matter physics. The determination of the ground state of these systems is fundamental to understanding the physics responsible for the behaviour of condensed matter systems at low temperatures. The order parameter of phase transitions is key to understanding the mechanism driving the transition and, therefore, the ground state of the system.

The heavy fermion material URu_2Si_2 is an example of a correlated electron system. Typically, solid state systems are understood by taking the one-electron energy levels and filling them up to the Fermi energy. In correlated systems this approach ceases to be valid, as the one-electron levels no longer describe the system because they neglect the interactions of the electrons with one another and the effects of the electrons on the lattice. The general approach to such systems is to renormalize them so that they can be described in terms of single-particle states where the charge carriers are now composite objects called quasiparticles.

In URu_2Si_2 specific heat measurements (Palstra *et al.*, 1986; Maple *et al.*, 1986) detected a phase transition at low temperatures, and it was assumed to be antiferromagnetic. Studies (Broholm *et al.*, 1987) quickly revealed that the ordered moment was anomalously small, but antiferromagnetic nonetheless and the material was largely consigned to the category of heavy fermion materials with magnetic order and a superconducting transition at low temperatures. On its own, this made it an anomaly in that magnetism and superconductivity were widely regarded as natural enemies. Heavy fermion superconductors were already being studied for violating this presumed rule, but the presence of superconductivity in a magnetically ordered system was particularly curious. Even though superconductivity had been considered ”solved” by the Bardeen-Cooper-Schrieffer (BCS) model thirty years earlier, it was becoming apparent that there was a great deal still to be understood.

It was realized (Mydosh and Oppeneer, 2011) that the tiny antiferromagnetic ordered moment was far too small to account for the entropy change at the transition, and that magnetic ordering wasn't the origin of the phase transition. This began a lengthy process of searching for an order parameter to actually explain what was happening. Complicating matters is the emergence of an unequivocal antiferromagnetically ordered state with modest applied pressure, crossing a first-order phase boundary from hidden order.

Magnetic fields have a fairly small effect on the hidden order state, and it seems quite robust. There is evidence that the magnetic field can destroy hidden order and that it re-emerges at even higher fields (Tripathi *et al.*, 2007), leaving a considerable puzzle about how it interacts with applied magnetism. The tiny ordered moment appears to be extrinsic (Matsuda *et al.*, 2008), caused by impurities in the lattice, and evidence from NMR suggests that hidden order actually suppresses magnetism.

There is unambiguous evidence for the opening of a gap in the density of states at the hidden order transition. Both magnetic and electronic excitations become gapped at the transition, and the density of states is strongly suppressed. The scattering rate drops dramatically as the gap removes scattering states, but the loss of carrier density initially causes a small rise in the resistivity, giving it a bump at the transition.

Optical spectroscopy is an ideal tool for the study of the electronic excitation spectrum in such a system. It is possible to measure transitions down to very low frequencies using fairly simple techniques; 2 meV is not unusual as a low frequency cutoff for infrared spectrometers, and 3 meV is fairly standard with a pumped helium-cooled detector and a mercury arc source. Very fine resolutions are available, with 0.1 meV resolution at low frequencies easily achievable and 0.25 meV resolution standard. It is straightforward to cover several orders of magnitude in frequency using tabletop spectrometers and sources.

Ultimately, the hidden order state remains a mystery to this day, despite much work over the past five years by groups around the world. The possibility of a new quantum ground state, never seen before, lurking before us in an unassuming shard of metallic rock is tantalizing to say the least, and the search continues to identify the physical origin of the ordering. By illuminating the effects of the transition on the charge dynamics of the system, optical spectroscopy promises insight into the nature of this fascinating puzzle.

1.2 Thesis outline

The introductory chapters are broken down into discussions of the basic physics of correlated electron systems in general and heavy fermion systems in particular, a discussion of the methods of acquisition and analysis of optical data, and a review of the current state of experimental understanding of the hidden order state in URu_2Si_2. A detailed description of the modifications and innovations in the measurement of reflectance and the analysis of the data that have been made in the process of completing this work is also included, as in practical terms that is where most of my time over the last five years has been spent.

The body chapters will describe work done over the past five years in understanding the electrodynamics of URu_2Si_2. The first paper included is not chronologically the first paper written; it is an article that was submitted to Philosophical Magazine for a focus issue on hidden order. It summarizes the optical results on URu_2Si_2up to that date, however, and is therefore a useful introduction to the topic. It also attempts a synthesis of disparate results, and attempts to integrate the various optical studies into a coherent whole. It therefore makes a good starting point for what follows. The second paper is focused primarily on the temperatures above the hidden order state and understanding the Fermi-liquid behaviour of the material in its normal state. The third paper studies the anisotropic optical conductivity and discusses the importance of the differences in the optical conductivity between the ab plane and c axis of the tetragonal structure. This was the first report of the optical conductivity of the hidden order state in the c-axis. Finally, the fourth paper describes the enhancement of the hidden order and its change to antiferromagnetism when the crystal is doped with either Os or Fe, and the similarities and differences between the doping-induced antiferromagnetic state depending on the dopant. This is the first study of the electrodynamics of the antiferromagnetism in this material.

The concluding chapters include an attempt to bring the results of the different studies presented in the body together into a coherent picture of the electrodynamics of the hidden order state, and especially how it evolves with temperature, chemical pressure, and electronic doping, as well as the other changes or constants in the conductivity both in and out of the hidden order state. These results are then compared with and integrated into the body of knowledge of the hidden order state from other experimental probes. The final chapter summarizes the conclusions of this work.

Chapter 2

Literature Survey

The hidden order state in URu_2Si_2 has been the subject of intense experimental and theoretical investigation over the past several decades, with a burst of activity in the past six or seven years or so. New techniques as well as improvements in older techniques have allowed experiments that were previously impossible, while a range of new theoretical interpretations have both inspired and been inspired by these new experiments. In this chapter, I will summarize the state of hidden order as it is currently understood, including theoretical investigations and proposals for the hidden order parameter and especially the results of recent experiments and what they mean for the underlying physics as well as the various proposed theories.

The transition at 17.5 K in URu_2Si_2 was observed in the resistivity as a small bump (Palstra *et al.*, 1985) and in the specific heat (Palstra *et al.*, 1986; Maple *et al.*, 1986), which identified it as a second order phase transition. As the interaction between f electron spins is antiferromagnetic, and as antiferromagnetic fluctuations are proposed to be responsible for the pairing in the subsequent superconducting state at low temperature (Palstra *et al.*, 1986; Tripathi *et al.*, 2007) it was naturally assumed that this phase transition was an indicator of antiferromagnetic ordering. However, subsequent neutron scattering measurements (Broholm *et al.*, 1991) demonstrated that the maximum ordered moment was no greater than 0.03 μ_B per U atom. Certainly a tiny ordered moment, but an antiferromagnetically ordered moment nonetheless.

It was apparent, however, that the antiferromagnetism was insufficient to account for the entropy quenched at the transition, which was of the order R ln 2 (where R is the gas constant) (Tripathi *et al.*, 2005). The various alternatives were subsequently sequentially eliminated. The absence of any lattice modulation ruled out static density wave order or a structural transition. Neutron scattering (Broholm *et al.*, 1987) ruled out long-range magnetic ordering. Subsequent work has focused on establishing the characteristics and phenomenology of the hidden order state, while theorists propose models that either guide experiment or are informed or contradicted by it.

This chapter is intended to describe the current state of research on URu_2Si_2 as it stands at the time of writing. I will describe herein the current research efforts and their results with a particular focus on the recent experiments of the last eight years or so; most important experiments prior to that have been described in the introductory chapter (Chapter 1), but where this is not the case the relevant work will be mentioned and cited. I will discuss the salient features of some of the models that have been proposed recently as well. As with any active field with many different groups, both theoretical and experimental, working at once, there is some confusion about results and their interpretation. Experiments do not always agree with each other, and different probes of the same properties find different values for the same physical quantities. Likewise, many of the models that have been proposed are mutually exclusive and have more than one way of being compared with present experimental data. Where such controversy exists and I am aware of it I will draw attention to it without necessarily supporting either argument; the merits of the two positions can be weighed by the reader at their discretion.

2.1 Transport, quantum oscillations, and de Haas/van Alphen

Measurements of the resistivity (Palstra *et al.*, 1986) of URu_2Si_2 show that it is a fairly typical heavy fermion semimetal. At temperatures above T_{coh} ~70 K the resistivity is large and increases with decreasing temperature as expected for a single-impurity Kondo effect. Below T_{coh} the resistivity decreases as the temperature is lowered, as expected for the formation of a Kondo lattice state and the onset of coherence. The resistivity is anisotropic with the c-axis having a much lower resistivity, by a factor of about 3, but the same qualitative overall behaviour. Figure 2.1 shows the resistivity and specific heat of URu_2Si_2.

The transition can be identified in the resistivity by a small bump feature at the transition temperature (Palstra *et al.*, 1986; McElfresh *et al.*, 1987; Zhu *et al.*, 2009). This is caused by a competition between the mobility of the carriers and the gapping of the Fermi surface as the temperature is lowered, carrier density goes down, causing an upturn in the resistivity, before the carrier mobility increases by a larger amount and the resistivity turns down again. In the HO state, the carriers exhibit behaviour typical of a gapped Fermi liquid, and the resistivity can be fit by a Fermi liquid term and an exponential term that goes like $e^{\frac{\Delta}{T}}$. More recent results (Tateiwa *et al.*, 2012) suggest that the Fermi-liquid fit is inadequate, and a generalized power law T^n is

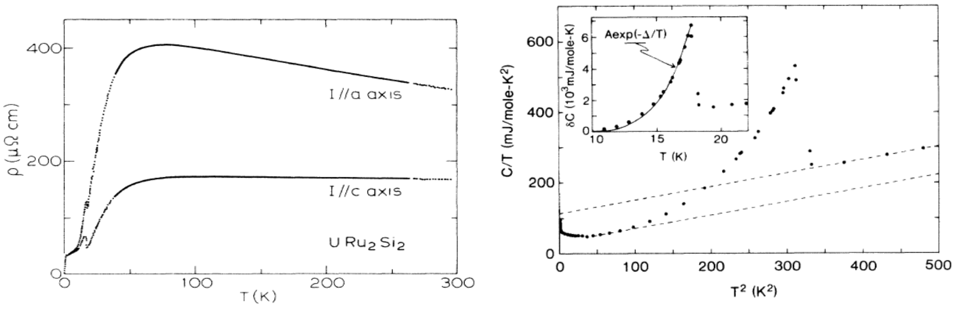

Figure 2.1: Left panel: the resistivity of URu_2Si_2 in both the ab plane and c axis. The resistivity is anisotropic, and there is a small anomaly at the HO transition temperature, at T_{HO}=17.5K. The high-temperature resistivity rises as the temperature is lowered due to the single-impurity Kondo effect. At the coherence temperature the resistivity starts to decrease as the temperature continues to fall, as the magnetic impurities are screened out by the conduction electrons and cease contributing to scattering. After Palstra *et al.* (1986). Right panel: the specific heat anomaly at the HO transition, showing the second order character of the transition and exponential decrease below the transition. After Maple *et al.* (1986).

required to fit the data in the HO state. The exponent n varies from 1.5 at zero pressure up to the Fermi liquid value of 2 in the AFM state under pressure.

Specific heat measurements (Palstra *et al.*, 1985) show a clear signature of a second order phase transition at the ordering temperature. The right panel of figure 2.1 shows the specific heat of URu_2Si_2. The effective mass of the carriers can be estimated (Maple *et al.*, 1986) to be around 25m$_e$, where m$_e$ is the bare electron mass. This is not compatible with later optics (Nagel *et al.*, 2012) and STM (Schmidt *et al.*, 2010) measurements, which see an effective mass of ∼5m$_e$. Similarly the gap observed in specific heat is inferred to be on the order of 11 meV, which is much larger than the gaps observed in conventional spectroscopy techniques such as optics and ARPES. It is at present not well understood how to resolve this discrepancy, but it is presumably related to the way that specific heat averages over all the electronic states and bands.

2.2 Spectroscopy: Optics and Raman

Much work on the study of the charge dynamics of URu_2Si_2 has been done by using the various electronic spectroscopy techniques, each with its advantages and limitations. The results offer complementary information about the behaviour of URu_2Si_2 as it crosses from the heavy-fermi-liquid regime to the hidden order state.

The optical conductivity of URu_2Si_2 was first studied in the 1980s by Bonn *et al.* (Bonn *et al.*, 1988). Figure 2.2 shows the optical conductivity and reflectance data on URu_2Si_2 from Bonn *et al.* It shows a distinct energy gap developing below the hidden order transition, visible as a sharp absorption line in the reflectance spectrum, that appears only below 17.5 K. There is a broader suppression of the reflectance in the region above ∼12 meV with an onset below the hybridization temperature of 70 K, where the resistivity turns over and begins to decrease as the temperature is lowered. The optical conductivity, which Bonn *et al.* obtain from their low frequency measurements by extrapolating the reflectance to higher frequencies by simulating with Lorentzian oscillators and then performing Kramers-Kronig inversion, shows that the behaviour of the energy gaps is qualitatively different. The higher-energy, higher-temperature gap, hereafter referred to as the hybridization gap, is broad, has no distinct onset, and the spectral weight lost in the gap is not recovered at low frequency. The lower energy, lower temperature gap, hereafter referred to as the hidden order gap, is sharp, well defined, and shifts the spectral weight to a peak in the conductivity that appears immediately above the gap energy.

More work has been done on the optical conductivity of URu_2Si_2; much of it has been done by me, however, and forms the body of this thesis, so I will leave the discussion of this work for subsequent chapters. Likewise, much of the work of other

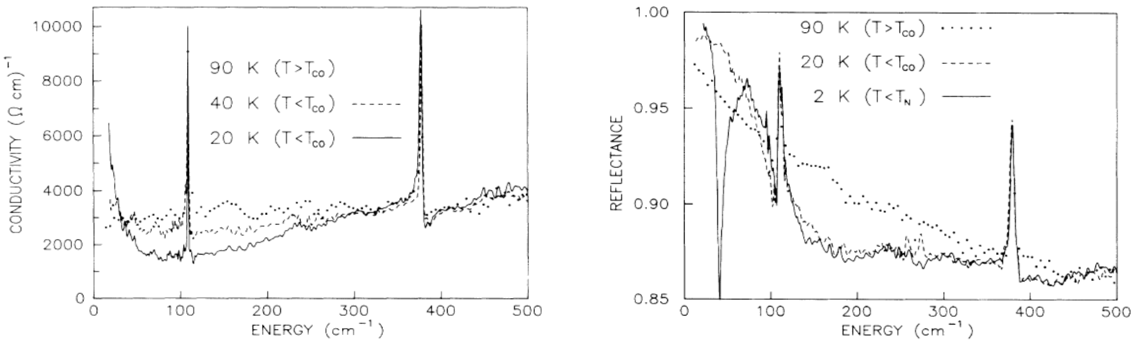

Figure 2.2: The optical conductivity (left panel) and reflectance (right panel) of URu_2Si_2. The hybridization can be seen as a suppression of the conductivity and reflectance above 100 cm^{-1} between 90 K and 20 K. The hidden order is characterized by a sharp absorption feature in the reflectance at 40 cm^{-1} that corresponds to the opening of a gap in the Fermi surface with spectral weight recovery in a peak that appears immediately above the gapped region in the HO state. After Bonn *et al.* (1988).

groups on the optical properties of URu_2Si_2 is discussed and key points summarized in chapter 4, and I don't wish to spoil the narrative flow of my thesis by giving away the game prematurely, so I will leave further consideration of the work of Guo *et al.* and Levallois *et al.* for later.

Time-resolved terahertz measurements performed on URu_2Si_2 by Liu *et al.* (Liu *et al.*, 2011) show evidence for the existence of two distinct gapping processes, both with onsets above the hidden order transition. One seems to be associated purely with the hybridization gap, while tother onsets around 25 K and increases in magnitude (both delay time and amplitude) as the temperature is lowered. This only adds to the confusion surrounding the issue of order parameter fluctuations, as the authors attribute the onset of the second decay process with the appearance of the order parameter fluctuations suggested by Balatskys team (Haraldsen *et al.*, 2011; Dubi and Balatsky, 2011). It makes more sense to attribute this second lifetime to the other electronic structure changes occurring in the temperature range immediately above the hidden order transition due to hybridization.

Recent Raman measurements have raised the question of whether and in what manner the lattice symmetry changes upon entering the hidden order state. The well-known A_{2g} mode that appears as the hidden order state is entered and roughly tracks the strength of the transition (Cooper *et al.*, 1987; Buhot *et al.*, 2014; Kung *et al.*, 2014). It is associated with the D_{4h} space group of the body-centred tetragonal lattice. Controversy has erupted, however, over whether this mode is pure in the HO state or leaks into the other polarizations, indicating the weakening of the symmetry. The nature of the symmetry in the hidden order phase, and whether the tetragonal symmetry of the crystal is preserved or rendered orthorhombic (Tonegawa *et al.*, 2014), is still an open question. The suggestion that the very weak orthorhombicity deduced from x-ray measurements is responsible for the Raman signals in the A_{1g} and B_{1g} channels (Kung *et al.*, 2014) supports this notion, but its absence in the same measurements performed by a different group (Buhot *et al.*, 2014) and the extreme weakness of the signal relative to the scatter of the data points makes me extremely hesitant to commit one way or the other on this issue. I will note that the weakness of the signal in Raman scattering is consistent with x-ray measurements, in which the orthorhombic distortion is on the order of 10^{-5} (Tonegawa *et al.*, 2014), so I'm not prepared to throw out the observation as wishful thinking just yet.

2.3 Scanning-tunneling microscopy and angle-resolved photoemission spectroscopy

STM measurements have done much to illuminate the electronic structure changes that URu_2Si_2 undergoes at the HO transition. A light band that crosses the Fermi surface above the transition is seen hybridizing at the transition and becomes a much heavier band with a gap just above E_F. This can be seen in figure 2.3. This observation strongly implies that the hybridization and the formation of the heavy fermion state (or Kondo lattice state, alternatively) is not complete until the hidden order transition. The fact that the heavy quasiparticles involved in the transition are known from specific heat to have an effective mass of $\sim 25 m_e$ while the heavy band that forms at the transition has an effective mass of $\sim 5 m_e$ raises further questions about exactly which quasiparticle bands, and therefore which parts of the Fermi surface, are involved in the transition. The observation from quantum oscillations that there is no significant change from the hidden order state to the large-moment antiferromagnet state implies that the electronic restructuring must be similar across both transitions. Two questions are thereby raised: why is the hybridization in this material, and none of the many other heavy-fermion materials, associated with a second-order phase transition? And why does this lead to hidden order at zero pressure, but to antiferromagnetism under so many other sets of conditions (doping, pressure, etc.)? These questions will, one hopes at any rate, be answered by the final explanation of the order parameter (whatever that may turn out to be).

A number of other interesting points are raised by the STM measurements of Schmidt *et al.* and Aynajian *et al.* with implications for possible theoretical models

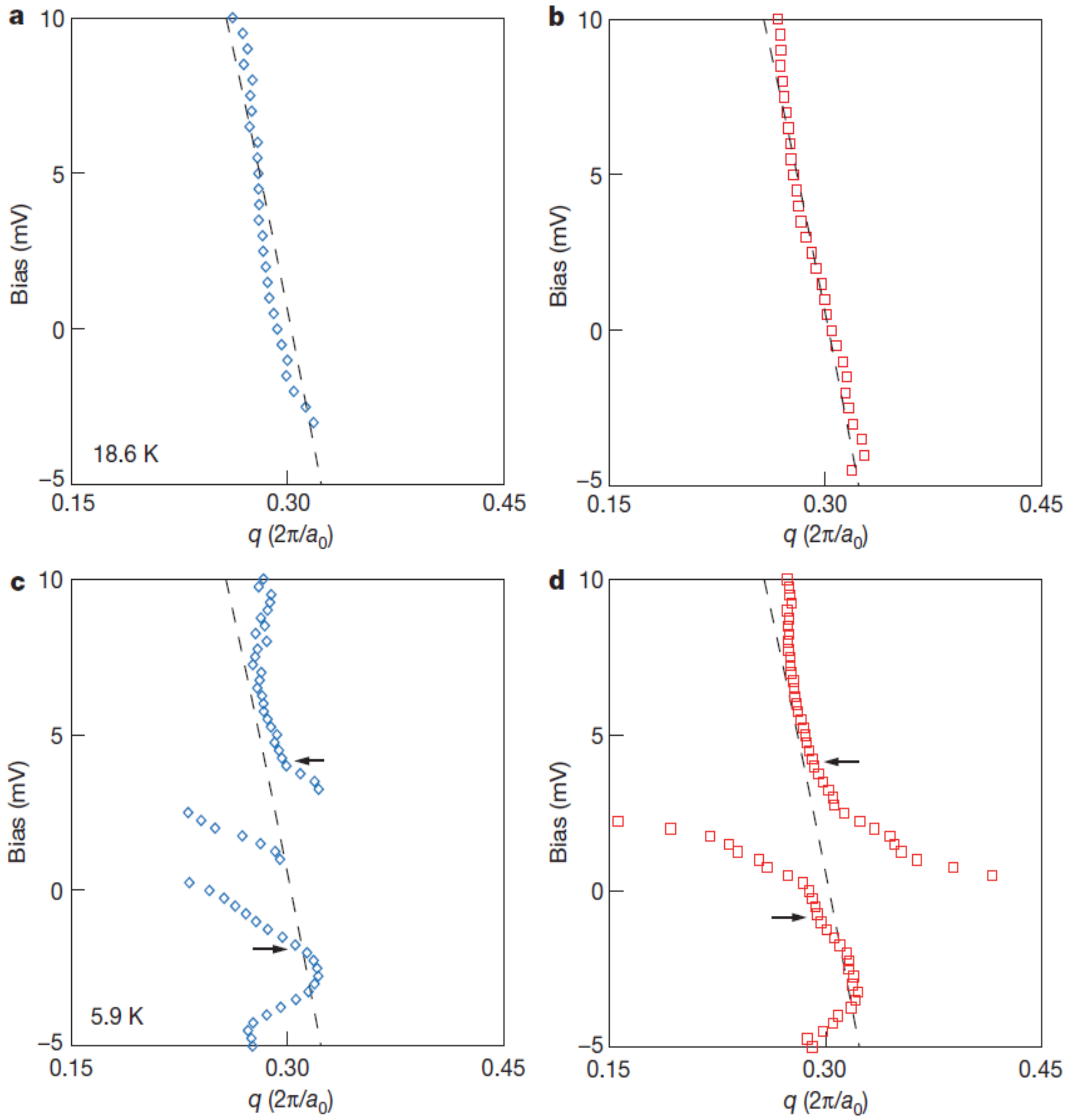

Figure 2.3: The hybridization of the light and heavy bands occurring at the hidden order transition in two primary directions in k space. Above the transition (top panels), light hole bands are seen crossing the Fermi surface. Below the transition (bottom panels) in both directions the light bands have each evolved into two heavy bands. After Schmidt *et al.* (2010).

and proposed order parameters (Schmidt *et al.*, 2010; Aynajian *et al.*, 2010). Neither sees any evidence for a conventional density wave state, nor any evidence of crystal field splitting. Aynajian *et al.* fit their energy gap to a mean-field prediction and find that it fits nicely, with the caveat that their fit has the gap closing at 16 K instead of 17.5 K. This they ascribe to their measurements being performed on the surface of the material and assume that in the bulk it will match specific heat measurements. However their fit of the gap matches that in the optical conductivity (Hall *et al.*, 2012) very well, which is certainly a bulk probe. Their measurements therefore in fact lend support to the energy gap deviating from mean-field behaviour at temperatures close to the transition.

ARPES measures both the energy and momentum dependence of the quasiparticles, allowing full imaging of the electronic excitation spectrum, with the caveat that they cannot directly measure states above the Fermi level (as no charges exist to be excited at these energies) and they are limited to performing surface measurements on cleavage planes. ARPES therefore is an extremely useful probe for determining the exact shape of the Fermi surface. Measurements on $\mathrm{URu_2Si_2}$ reveal a number of interesting details (Santander-Syro *et al.*, 2009; Boariu *et al.*, 2013; Dakovski *et al.*, 2014). Among these is the momentum dependence of the energy gap both in the hybridization temperature regime and in the hidden order state, the characteristics of the bands crossing the Fermi level and their evolution with temperature, and the nature of the quasiparticle scattering above and below the transition temperature.

The nature of the bands crossing the Fermi level at the HO transition is a question that ARPES is particularly well-suited to answering. Early measurements from the late nineties (Yang *et al.*, 1996; Ito *et al.*, 1999) were able to identify the itinerant U-5f character of the bands in the hybridization regime, suggesting that the hybridization of these electrons was responsible for the increase in effective mass. These results did not probe the HO state, however, as they were unable to reach sufficiently low temperature, and the correspondence between band-structure calculations and observations was lacking, leading to a necessary openness of the conclusions to interpretation (Ito *et al.*, 1999; Mydosh and Oppeneer, 2011). The localized or itinerant character of the carriers remains a point of contention between competing models of the order parameter (Mydosh and Oppeneer, 2014), as most measurements are suggestive of an itinerant character but it is difficult to account for the Ising anisotropy in itinerant models.

More recent ARPES measurements have illuminated the characteristics of the electronic structure as the hidden order transition establishes itself in the material. High-energy ARPES measurements (Santander-Syro *et al.*, 2009) observe a heavy quasiparticle band cross the Fermi surface and become coherent at T_HO. This suggests that coherence does not develop in the carriers until the hidden order transition occurs. This is in contrast to the usual understanding of the resistivity drop in heavy fermion materials as being the result of the development of coherence as the magnetic impurities are screened out by conduction electrons, but is in agreement with STS measurements (Schmidt *et al.*, 2010) (which see hybridization occur only at the transition) and optics (Nagel *et al.*, 2012) (which sees a strong incoherent background become gapped at the transition). Further measurements (Chatterjee *et al.*, 2013) reveal the presence of incoherent heavy bands that hybridize at the HO transition with lighter conduction bands, forming a heavy Fermi liquid in the HO state.

Time-resolved measurements (Dakovski *et al.*, 2014) indicate that short-lived

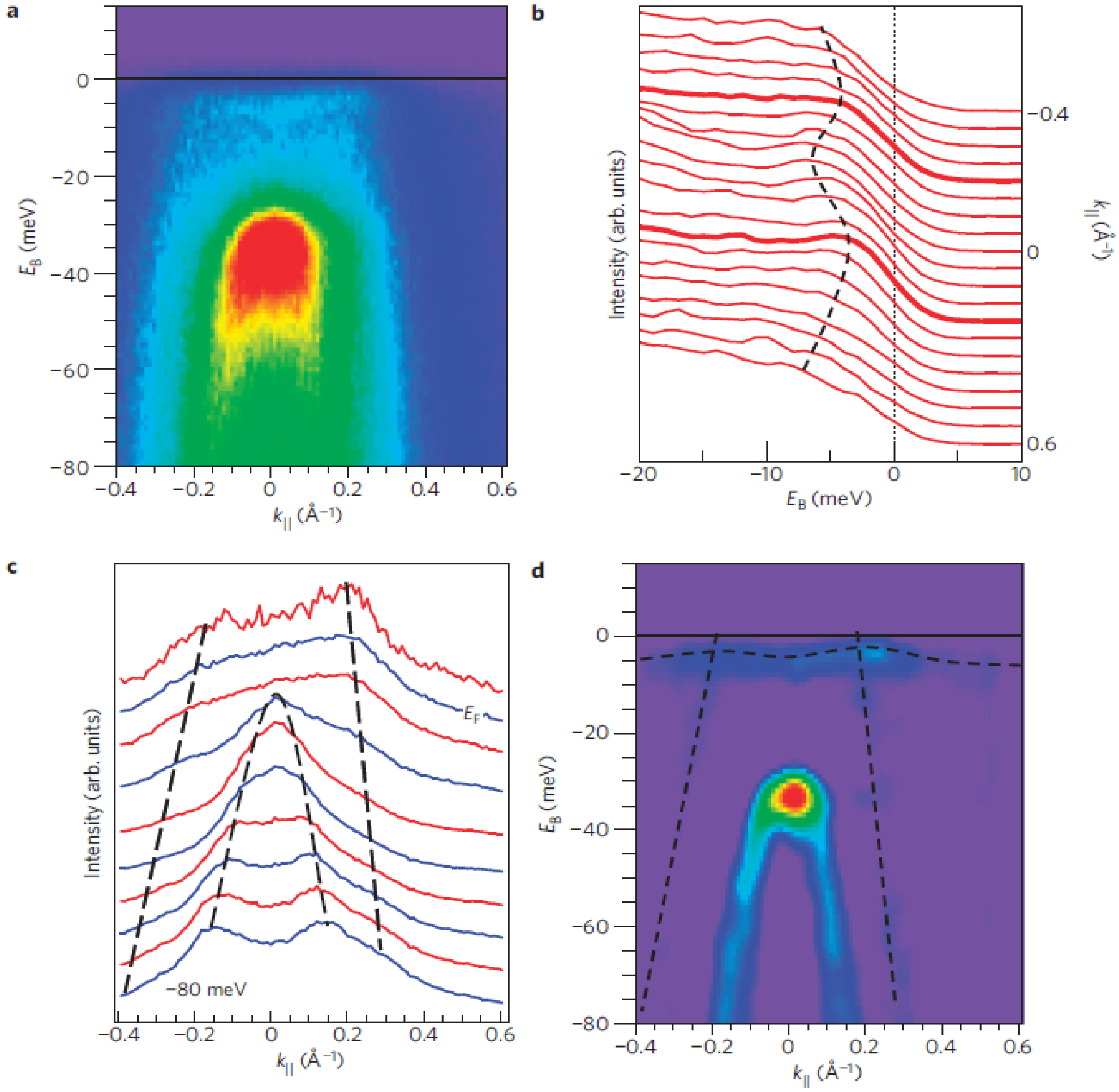

Figure 2.4: ARPES data shows the heavy bands dispersing below the Fermi level in the HO state. Panel b) and c) show the energy and momentum distribution curves, respectively, from the integrated intensity in panel a). Panel d) shows the heavy band near E_F that crosses the Fermi level at the transition, as well as the conduction bands. After Santander-Syro *et al.* (2009).

quasiparticles at the Fermi-surface hot spots become much longer lived upon entering the hidden order state. Measurements comparing the behaviour of the electronic structure in different crystal directions (Boariu *et al.*, 2013) suggest that the hybridization and hidden order affect different parts of the Fermi surface; a gap of ∼11 meV exists at the X-point above T_{HO} and remains unchanged upon entering the HO state. This is compatible with optical measurements, which put the hybridization gap around 12 meV. The HO gap, by contrast, opens at the Γ and Z points, and exists only below the transition temperature. Further measurements (Chatterjee *et al.*, 2013) once again show hybridization occurring only at the HO transition and as a sharp change rather than a gradual crossover to a heavy Fermi liquid with a much lower scattering rate. This further begs the question of why this phenomenology, which is relatively common in f electron materials, is so different in URu_2Si_2 and is associated with a second order phase transition here but nowhere else. The question remains unanswered, although several ways of addressing it have been advanced such as hybridization between non-Kramers and Kramers bands (Chandra *et al.*, 2015).

2.4 Neutron scattering

The first neutron scattering results (Broholm *et al.*, 1987) showed that there was a tiny ordered moment in the HO state, about 0.04 μ_B per U, ordered antiferromagnetically along the c direction. This order has subsequently been shown to be extrinsic to the HO state (Matsuda *et al.*, 2008). More recent neutron scattering measurements have illuminated the magnetic excitation spectrum above(Janik *et al.*, 2009) and below (Wiebe *et al.*, 2007) the transition. Figure 2.5 shows the excitation spectrum in the left panel. Above T_{HO}, there is a continuum of magnetic fluctuations at

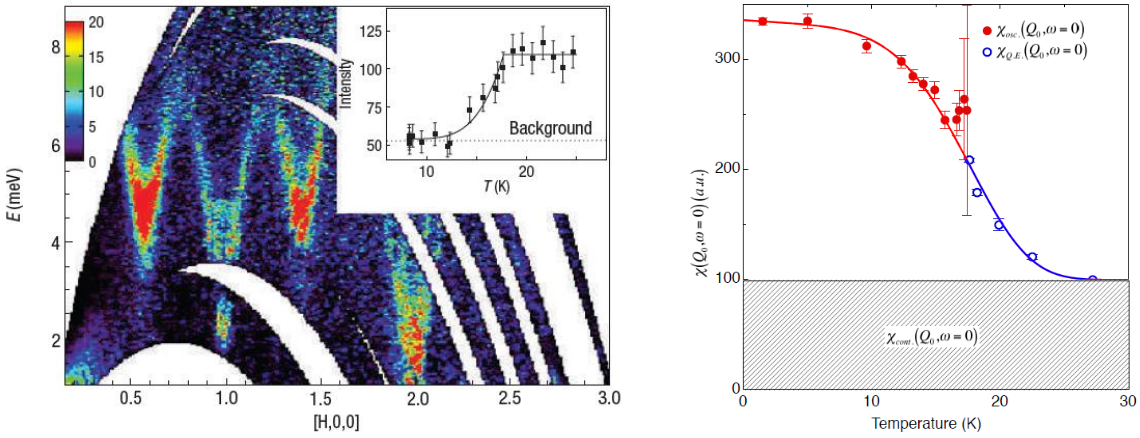

Figure 2.5: Neutron scattering data on URu_2Si_2 after Wiebe *et al.* (2007) (left panel) and Bourdarot *et al.* (2010) (right panel). The left panel shows the modes at the commensurate and incommesnurate wave vectors corresponding to spin fluctuations. It also shows that the commensurate and incommensurate excitations in the HO state develop different sized energy gaps. The right panel shows the OP behaviour of the dynamical susceptibility, suggesting that it tracks the order parameter. However, as it does not become critical (that is, it does not go to zero at the transition) it cannot itself be directly related to an order parameter.

the commensurate wave vector Q_0=(1,0,0) and at the incommensurate wave vector Q_1=(1±0.4,0,0). At the HO transition these become gapped, with gaps of 2 meV and 4 meV respectively. The gapping of the incommensurate modes is responsible for much of the loss of entropy at the transition.

Further neutron scattering measurements Villaume *et al.* (2008) identified the gapped inelastic excitations along the commensurate wave vector as a signature of the HO state. Under pressure, the mode collapses into an antiferromagnetic Bragg peak. The commensurate excitation spectrum remains gapped and inelastic in the AFM state, with the gap rising to higher energy. As the commensurate excitations are associated with the of AFM order, this is reasonable, but it leaves unanswered what role it plays in the HO state as the nesting is present in both but only in the

AFM state does it lead to magnetic ordering.

The dynamical spin susceptibility (Bourdarot *et al.*, 2010) at the commensurate wave vector was measured carefully across T$_{HO}$, and found to have mean-field-like order parameter behaviour. This can be seen in the right hand panel of figure 2.5. It does not go to zero at the transition, but rather relaxes slowly as the temperature is raised. The energy gap of the excitations, meanwhile, has a sudden onset at the transition, increasing from zero above T$_{HO}$ to nearly its full value directly below. The origin of the gapping, and whether the spin gap drives the charge gap or vice versa, remains unclear; the authors suggest a dual picture of itinerant electrons responsible for the spin gap and localized bands gapping at the Fermi level. Bourdarot *et al.* extract a Fermi surface gap of $\sim$7.7 meV, larger than the spin gaps and in rough agreement with specific heat but much larger than is seen by charge spectroscopies (Schmidt *et al.*, 2010; Hall *et al.*, 2012). This gap increases suddenly at the onset of AFM ordering and is then constant in the AFM phase.

2.5 Nuclear magnetic resonance, torque magnetometry, and polar Kerr effect

Nuclear magnetic resonance measurements have focused on the magnetism and the density of states in URu$_2$Si$_2$. Unlike neutron scattering, NMR is a local probe of magnetism that can identify regions of magnetism and investigate the magnetism at specific lattice sites. Early NMR work (Matsuda *et al.*, 2001) showed that the AFM moment in the HO state was the same as in the HO state, and the volume fraction increased with applied pressure. This indicated that the small antiferromagnetic moment seen in the HO state is caused by strain regions in the lattice due to impurities rather than being a feature of the ordered state. Subsequent work (Takagi *et al.*, 2007) has confirmed that the SMAFM state is extrinsic and not a characteristic of the HO order parameter, and further that the HO actually suppresses magnetism at the Si sites in the lattice, indicating that the HO state is actually incompatible with magnetic order.

New susceptibility measurements (Okazaki *et al.*, 2013) dubbed torque magnetometry detect a susceptibility anisotropy in the basal plane of the tetragonal crystal structure in the HO state that is not present in the normal state above the transition, indicating a breaking of the four-fold rotational symmetry present in the crystal structure. They attribute this to an electronic-nematic state. The anisotropy is not present in larger samples, however, which they attribute to domain formation. NMR measurements investigating this feature (Kambe *et al.*, 2011) find an anisotropy that is much smaller, ∼15 times smaller, in a much larger sample. They exclude domain formation, since NMR is insensitive to domains as it is a local probe. Instead they propose a sample-size dependence to the anisotropy, a proposal whose implications are not yet understood and which requires further investigation. The breaking of rotational symmetry in the HO state is under theoretical investigation for its implications for the various models that have been proposed (Mydosh and Oppeneer, 2011).

The question of time-reversal symmetry breaking in the HO state arises naturally from the question of multipoles and magnetic ordering. Although the AFM state is found to be extrinsic and not related to the hidden order, and that the hidden order is in fact hostile to magnetism, nonetheless time-reversal symmetry breaking is a way to differentiate between proposed models of HO. Polar Kerr effect measurements (Schemm *et al.*, 2015) detect time-reversal symmetry breaking in the superconducting state of URu_2Si_2 but no evidence for TRS breaking in the HO state was seen. This is in contrast to the NMR and μSR measurements, which see evidence for TRS breaking; the difference could be the local versus bulk nature of these probes (Mydosh and Oppeneer, 2014).

More recent NMR results (Shirer *et al.*, 2012, 2013) suggest that the hidden order produces a suppression of the density of states well above the transition temperature. This is compared with pseudogap data caused by precursor fluctuations in other materials. However it is not clear that they can resolve the difference between precursor fluctuations and the expected behaviour caused by the hybridization and coherence, as optical data has already shown that the density of states becomes suppressed above the transition as expected for a heavy fermion material. The question of precursor fluctuations is similarly controversial, with ARPES detecting no evidence for it (Boariu *et al.*, 2013) and at least one PCS paper that is typically taken as evidence for the opening of a gap above the transition (Park *et al.*, 2012) is considered discredited (Lu *et al.*, 2012) by others in the field and doesn't agree with other PCS measurements or any other electronic spectroscopy measurements.

2.6 Antiferromagnetism: Pressure and doping

The tiny antiferromagnetic moment of $\sim$0.03 μ_B per U increases to 0.4 μ_B per U atom at a pressure of 0.5 GPa at low temperature (Amitsuka *et al.*, 1999). A first-order phase boundary separates the HO and LMAFM states. μSR (Luke *et al.*, 2004; Amato *et al.*, 2004) and NMR (Matsuda *et al.*, 2001, 2003) measurements demonstrate that the small AFM moment in the HO state is constant but that the volume fraction increases with pressure across the HO/AFM phase boundary. This led to the understanding that the tiny AFM moment in the HO state is extrinsic and caused by stress regions due to impurities creating puddles of LMAFM in the HO state (Matsuda *et al.*, 2008).

Quantum oscillation measurements (Hassinger *et al.*, 2010) show very similar frequencies in both the antiferromagnet phase and the HO phase, implying similar Fermi surfaces. The measurements performed at relatively modest pressures and fields are probably applicable at higher pressures, and other evidence which sees a field-reentrant hidden order phase under pressure (Aoki *et al.*, 2009) puts the SdH measurements squarely in the AFM state. This suggests that the lattice doubling present in the AFM state exists in the HO state, though the magnetic ordering itself is absent, and that the order parameter reorders the Fermi surface in the same way regardless of whether underlying magnetic ordering occurs or not.

The LMAFM state is associated with the AFM wave vector Q=(1,0,0) and the excitations at this wavevector are not gapped in the LMAFM state (Bourdarot *et al.*, 2005). In contrast, the excitations at the incommensurate wavevector Q*=(1.4,0,0) remain gapped in the LMAFM state and the gap increases from ∼4 meV to ∼6.5 meV at a pressure of 1.67 GPa (Villaume *et al.*, 2008). This is accompanied by an increase in the temperature of the HO/AFM transition, from 17.5 K in vacuum to over 20 K at 2 GPa pressure, as seen in the specific heat (Fisher *et al.*, 1990) and resistivity (Jeffries *et al.*, 2007). The gap inferred from both resistivity and specific heat increases with increasing pressure, and there are no changes to the behaviour of the transport properties as HO gives way to LMAFM with increasing pressure.

Recent point contact spectroscopy measurements (Lu *et al.*, 2012) show the same increase in the transition temperature with pressure that other measurements do. Notably, the high temperature onset of the transition suggested by other PCS measurements (Park *et al.*, 2012) was absent in their low pressure data and the asymmetric twin peak structure emerged only below the transition temperature both in vacuum and under hydrostatic pressure; the authors attribute this to the softness of their contact using silver epoxy. They do note that after pressure cycling, they observe the onset of hidden order persisting up to higher temperatures, indicating an extrinsic effect. In spite of the increased transition temperature under pressure, no increase in the gap associated with the formation of the ordered state is observed, in contradiction of specific heat and resistivity measurements as well as the behaviour of the incommensurate neutron mode (Villaume *et al.*, 2008) and, as will be shown, optical spectroscopy.

Neutron scattering experiments under pressure track the evolution of the magnetic modes into static order in the AFM state. The Q=(1,0,0) Bragg peak associated with antiferromagnetic order is strongly enhanced (Amitsuka *et al.*, 1999) by the application of pressure, while the gapping of this mode in the HO state disappears upon entering the AFM phase (Bourdarot *et al.*, 2005). The incommensurate excitations at Q*=(1.4,0,0) remain gapped, by contrast, and indeed the size of the gap is considerably enhanced by the application of pressure (Villaume *et al.*, 2008).

Recent studies have shown that isoelectronic doping of Fe (Kanchanavatee *et al.*, 2011; Das *et al.*, 2015) or Os (Kanchanavatee *et al.*, 2014; Wilson and Luke, 2015) onto the Ru sites induces antiferromagnetism without the need for hydrostatic pressure.

The question of whether this antiferromagnetic state is equivalent to the pressure-induced one is undecided. Simple chemical pressure seems not to be the mechanism responsible for the antiferromagnetism in even the Fe-doped material (Wilson and Luke, 2015) but, unlike the antiferromagnetism induced by doping with Rh (Yokoyama *et al.*, 2005) which reduces the transition temperature, both Os and Fe doping raise the transition temperature before crossing a phase boundary to antiferromagnetism, just like hydrostatic pressure does. The most reasonable conclusion at this point is that the doping induces antiferromagnetism by the same mechanism that hydrostatic pressure does, even if the magnetic moments are not the same (Das *et al.*, 2015; Wilson and Luke, 2015) as the hydrostatic pressure case.

2.7 Comments on theoretical models

A number of different models have been proposed to explain the phase transition in URu_2Si_2. Sometimes, proposals for the order parameter come directly from experiment, when some quantity or other is found to have the temperature dependence expected of an order parameter from mean-field theory (the hybridization observed by Schmidt *et al.* for example (Schmidt *et al.*, 2010)). Most, however, are proposals based on some sort of calculation, showing that the properties of a proposed model fit those of the HO state.

Band structure calculations (Elgazzar *et al.*, 2009; Oppeneer *et al.*, 2011) have recently focused on identifying the nesting vectors and hot spots in the Fermi surface associated with the hybridization-to-antiferromagnetism transition under pressure. This allows calculations to be done on well-understood states involving long-range magnetic order, which means the tools of conventional condensed matter theory can be brought to bear on the problem of URu_2Si_2. As the Fermi surface is believed to be the same (Hassinger *et al.*, 2010) in the LMAFM state and the HO state the calculated band structure and Fermi surface should be applicable in the HO state. As a result, the electronic band structure is well understood in the HO state, even though what creates the ordering is still unknown.

As long-range magnetic dipolar ordering has essentially been ruled out as the driver of the transition, perhaps naturally several theories have proposed higher order multipoles as being responsible for the hidden order state, including quadrupolar, octupolar, dotriacontadipolar, and hexadecapolar ordering (for a summary, see Mydosh and Oppeneer (Mydosh and Oppeneer, 2014)). Most of these have been excluded experimentally; hexadecapolar ordering remains a possibility though there is no direct evidence for it.

At present, theories of the HO are divided into categories of either itinerant or localized models. The localized models face the difficulty that there is no evidence for local moments or crystal fields, while the itinerant models have difficulty explaining the Ising anisotropy and the absence of any in-plane magnetic moment (Mydosh and Oppeneer, 2014). Among the itinerant models, the difference between the incommensurate and commensurate wavevectors as the ordering wavevector is a distinguishing feature between several of them, although several others have been shown not to require in-plane magnetic moments that have not been detected. Among the localized models, of particular interest from the point of view of interpreting optical data are the models of Haule and Kotliar (Haule and Kotliar, 2009) and Chandra *et al.* (Chandra *et al.*, 2013, 2015).

The model of Haule and Kotliar proposes an arrested Kondo hybridization leading to a hexadecapolar ordering at low temperatures. Their complex order parameter has a real part associated with the HO state and an imaginary part that leads to an antiferromagnetic state; as there is no mixing between the real and imaginary parts there must be a phase transition from one to the other. Both of their order parameters have Q=(1,0,0) as their ordering wavevector. Aside from the absence of any crystal fields in the system (or at least their ability to elude detection so far), resonant x-ray scattering may be the only way to confirm or refute this model for certain; circumstantial evidence from optics may support it, however, as we shall see.

The model of Chandra *et al.* has been dubbed hastatic order, from the Latin ”hasta” for spear. They suggest that hybridization of a non-Kramers doublet leads to broken double-time-reversal symmetry in the HO state. This leads to a second-order phase transition upon hybridization, rather than the usual gradual crossover from hybridization of a Kramers doublet. This proposal naturally explains the large Ising anisotropy as well as the origin of the hybridization at the transition. It further naturally accommodates the antiferromagnetism induced by applied pressure, as both result from the same order parameter. The trouble is that hastatic order predicts a small in-plane magnetic moment that has been ruled out by neutron scattering measurements (Das *et al.*, 2013). Current questions surrounding whether purely itinerant models can fully explain the Ising anisotropy and whether domain formation is possibly responsible for the absence of an in-plane moment in neutron scattering are yet to be resolved, but the theory remains promising.

The model of resonant impurity scattering proposed by Maslov and Chubukov (Maslov and Chubukov, 2012) deals specifically with the case of Fermi-liquid-like scattering of carriers in the case of URu_2Si_2. In this picture, it is not only the usual electron-electron scattering that leads to an observed quadratic dependence of the scattering on temperature and frequency, but the presence of resonant impurities also contributes and gives a quadratic dependence to the scattering in both T and ω. The proportionality constant between the T and ω terms then gives the relative strength of each effect. This issue is explored in more detail in subsequent chapters.

Chapter 3

Experimental techniques and methods of analysis

3.1 Infrared reflectance spectroscopy

Infrared spectroscopy presents its own challenges, both in managing frequency ranges and in performing measurements. In these experiments, the technique used was normal-incidence reflectance Fourier-transform spectroscopy.

3.1.1 Fourier transform infrared spectroscopy

Optical measurements are useful because they give the energy-dependence of the optical properties of the material being examined. Spectroscopy requires, therefore, measuring the reflectance at every frequency of light incident on the sample. The simplest way to do this is by shining light of discrete frequencies on the sample and measuring the reflectance; in practice, finding enough lasers or LEDs to cover the entire spectrum is impractical. An alternative would be to take a beam of white light and decompose it into different frequencies using a prism or a diffraction grating. There is, however, a better way.

Fourier-transform spectroscopy uses a Michelson interferometer to project an interferogram onto the sample. A coherent beam of light is passed into the interferometer cavity, where it is divided into two beams by a beamsplitter. These beams travel down the "arms" of the interferometer, reflect off of mirrors (a scanning mirror and a fixed mirror, respectively) and then are recombined and pass into the sample compartment.

The position x of the scanning mirror along its track is recorded along with the intensity I of light at the detector. This is then plotted as an interferogram. As the mirror scans, each frequency gives a minimum in its intensity when the scanning mirror is at a position that causes the optical path to differ from that passing through the other arm of the interferometer by a factor of $\lambda/2$ where λ is the wavelength. When the path lengths are equal, the intensity is at its maximum value as all frequencies interfere constructively. The interferogram is built of many different signals, each with a different wavelength. This fact allows the interferogram to be Fourier transformed to give the frequency dependent power spectrum $P(x)$ using the equation

$$P(\omega) = \frac{1}{2\pi} \int_0^\infty I(x) e^{-i\omega x} dx \tag{3.1}$$

FTIR offers a number of advantages over conventional diffraction grating spectrometry. There is no loss due to the grating and no higher-order diffraction effects. Stray light is much less of a problem as only the modulation of the light contributes to the signal. The resolution is controlled by the length of the scan and can be increased simply by increasing the distance that the mirror moves. Interpolation is easy; the edges of the interferogram can have zeros added to them to provide additional data point density.

A concern is the apodization, or the process by which the signal, which will typically be close to zero but not exactly zero at the edges of the interferogram, is brought down to zero for the Fourier transform. Simply adding zeros to the edges of the interferogram will introduce a sudden discontinuous jump, which in general has a broad spectral component and can show up as additional, spurious noise in the spectrum. A variety of methods for apodization exist, in practice for the larger samples studied here they were not found to give any difference to the noise.

3.1.2 The Bruker IFS 66v/s measurement system

Many of the measurements included in this thesis were performed using a commercial Bruker IFS 66 v/s spectrometer (hereafter referred to simply as ”the Bruker”). The Bruker can be seen in Figure 3.1. It includes sources for the frequency ranges from the far infrared to the ultraviolet, and a variety of useful optical components. It includes a He-Ne laser for proper calibration of the position of the scanning mirror so that each scan is measured to a high accuracy.

The Bruker uses water-cooling to keep the sources from overheating, and an air track for the scanning mirror. The source is selected by the OPUS program but must be turned on manually with the external power supply. Four sources are available: mercury arc lamp, Globar blackbody source, a tungsten filament source, and a deuterium lamp, for the far, mid, and near infrared and the ultraviolet, respectively. The image size is controlled by a rotating aperture wheel and a plane mirror directs the

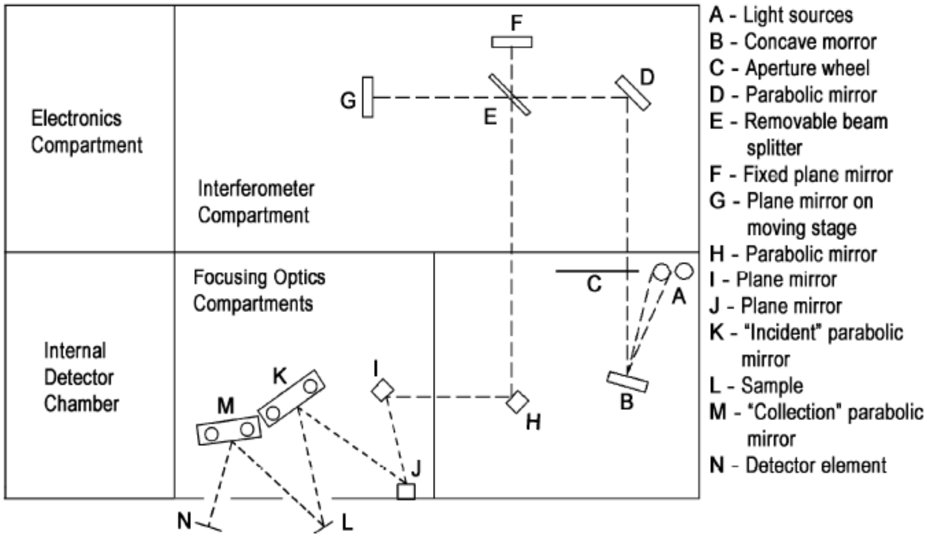

Figure 3.1: Schematic representation of the Bruker IFS 66 v/s spectrometer. The light path is shown by the dashed line and the individual components are labelled. After Purdy (2010).

light into the interferometer compartment.

One of the most important features of the Bruker system is the beamsplitter. Each frequency region has a beamsplitter optimized for those wavelengths. The far infrared region uses two different beamsplitters, both made with a mylar (polyethylene terephthalate) coating of different thicknesses. The 50 micron mylar beamsplitter is used for the very low frequencies, with energies between 2 meV and 6 meV, while a 6 micron beamsplitter with a germanium coating used from 5 meV to 60 meV. The thin mylar beamsplitter produces fringes that interfere with the measurements and so are somewhat limited in their frequency ranges. A KBr beamsplitter and a quartz beamsplitter are used in the middle infrared and near infrared/visible/ultraviolet, respectively.

Within the Bruker the light is controlled by a series of mirrors that can be used

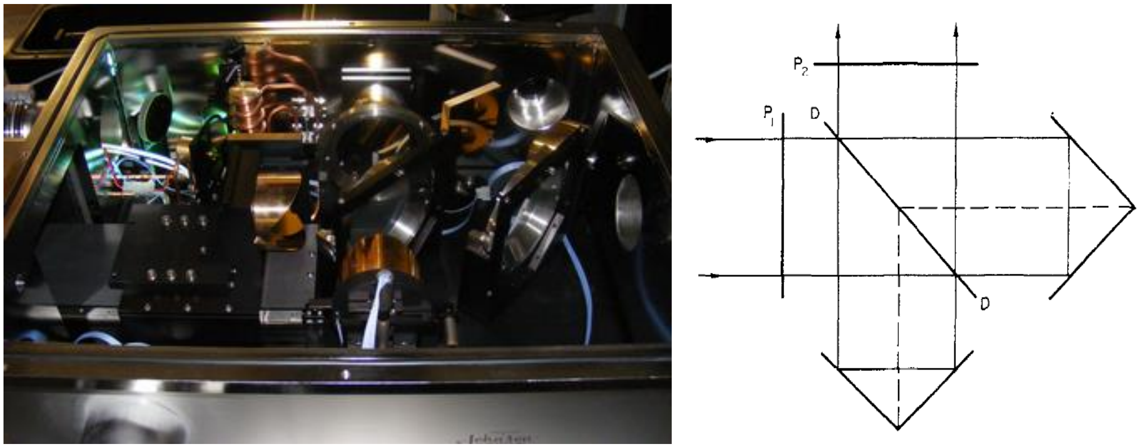

Figure 3.2: The Sciencetech SPS 200 spectrometer (left) showing the gold roof mirrors and the wire grid polarizers. The geometry of the Martin-Puplett spectrometer is shown in the right panel (from Martin and Puplett (1970)).

to focus the light onto the sample. The light enters the main compartment from the interferometer by reflection off of an ellipsoidal mirror. It is directed by two plane mirrors onto a parabolic collection mirror that focuses the light at the sample. The sample acts as a plane surface that reflects the light back to another parabolic mirror that focuses the light at the detector. The width of the light beam reaching the sample is controlled by an aperture in front of the first collection mirror at the focal point of the ellipsoidal mirror to eliminate stray light.

3.1.3 The Sciencetech SPS 200 measurement system

The Sciencetech SPS 200 polarizing interferometer ("the SPS" hereafter) operates on a slightly different principle to the Bruker's Michelson interferometer. The SPS is a polarizing roof-mirror interferometer that uses wire-grid polarizers and polarizing beamsplitters as its optical components. It is optimized for use in the far infrared, with large mirrors that use a gold coating. The SPS is shown in Figure 3.2.

The SPS includes a scanning-mirror interferometer but with additional polarizers for use in Martin-Puplett mode. The input polarizer is at 45 degrees to the beamsplitter. The roof mirrors flip the polarization of the light, and the output polarizer is once again at 45 degrees to the beamsplitter polarizer. The result is that the light is elliptically polarized with ellipticity dependent on the path difference between the two arms of the mirror when it reaches the output polarizer. The beam that passes through the output polarizer is linearly polarized with intensity varying with path difference, as in a Michelson interferometer.

3.2 Experimental procedure

Actually carrying out the experiments is a complicated process that often takes many hours at a time and that cannot, sadly, be spread out over several working days because of the limitations of the detectors. Over the past five years, I've spent a great deal of time tweaking and optimizing the experimental procedure, and then doing it all over again for a new measurement system. Fortunately, I was not called upon to make my own samples, and I am indebted to those who provided the materials that have been used to get the data that is now in this thesis. I will, therefore, not dwell on the procedure of actually growing crystals, which is described briefly in the manuscripts that form the body of this thesis.

3.2.1 Preparing and aligning the samples

Preparing samples for optical measurements involves preparing and mounting the samples themselves on brass cones, aligning the cones so that the light reflected by the sample actually hits the collection mirrors, and then aligning the mirrors so that the light hits the sample and then hits the detector. Sample preparation begins when the sample enters the lab. It is logged, its size and shape are recorded, and it is stored in a desiccator in a clearly-labelled container. If it is not atmosphere-sensitive it can be stored in an appropriate box, such as a toolbox or fishing-tackle box.

In order for a sample to be useful for optical measurements, it must have a few key characteristics. Ideally, it will be a large single-crystal. It will have a flat, smooth surface suitable for reflectance measurements on one side, and a parallel flat surface that need not necessarily be smooth on the other side. The reflecting surface will need to be either a cleavage plane or, where this is not possible, it will need to be polished smooth. Typically this will be smoother than half the wavelength of the light that is being used. Different powders of Al_2O_3 act as an abrasive to smooth out the roughness of the surface caused by cutting.

In the case of URu_2Si_2, polishing the sample seemed to destroy the optical signature of the hidden order for some reason. Small fissures in the surface or other surface damage seems the likely culprit, but despite being mirror-smooth in the visible the infrared reflectance no longer even showed the phonons characteristic of the material. To a lesser extent cutting the sample had the same effect, though not as strong. As URu_2Si_2 has a cleavage plane in the ab-plane this is the one that typically gets the most attention but in order to measure the c-axis, the samples needed cutting. A solution was required. In the end, it turned out that simply cutting the sample and then washing the surface in HF acid was sufficient to restore the optical properties of a clean surface. Discovering this took considerable trial and error, many failed experiments, a lot of time trying different acids, and a half-dozen melted pairs of

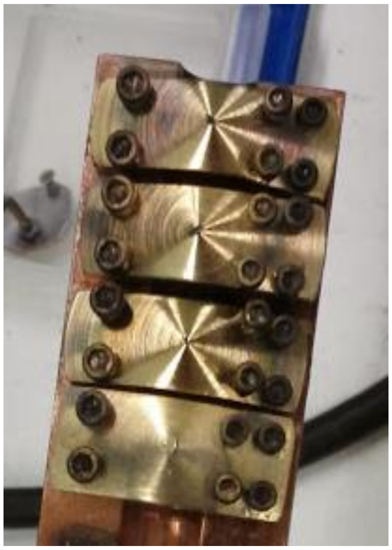

Figure 3.3: The samples, mounted on cones, which are in turn mounted on the copper sample holder that is attached to the cryostat. The aligning screws are visible on the cones. The samples depicted here are Sr_2IrO_4 and are less than 1 mm^2 in size.

tweezers.

The sample is washed with acetone to remove any surface contaminants (as URu_2Si_2 does not react with acetone and acetone evaporates without leaving any residue) and then attached to a brass cone using five-minute epoxy. The samples mounted on cones are shown in figure 3.3. The purpose of the cone is to direct any light that does not hit the sample away from the collection mirror, so any surface not covered by the cone must be at an angle, sloping away from the light path. This means that the flat surface on top of the cone where the sample is mounted should be approximately the size of the sample to maximize the area of contact for the epoxy but no larger than necessary. As a result, each cone must be machined specifically for the sample with which it is to be used. A CNC milling machine and lathe are used to make the cones out of brass rods.

In each cone, there are six screw holes, two of which are threaded. The holes that are not threaded are used to screw the brass cone into the copper sample holder. The threaded holes are used for set screws. The angle of the cone can be adjusted using the screws.

The alignment procedure is as follows. First, the reference mirror on its cone is mounted onto the copper sample holder. The cone must be in a neutral position vertically (the surface of the sample is not tilted up or down relative to the sample holder) and should be about the mid-point of its range of motion horizontally. The set screws are tightened enough that the cone is held firmly in place and cannot move. The cryostat is then mounted onto the translating stage and positioned so that the reference is directly in the light path. The copper sample holder is then rotated carefully on the cryostat until the image from the reference is centred on the collection mirror and screwed into place.

At this point, the sample cones are mounted onto the sample holder, loosely and without tightening the set screws. The cryostat is then mounted in a bracket that can translate forwards and backwards, and a laser is shone onto the reference so that the reflected beam hits a paper target. The location of the reflection is marked, and the cryostat is translated so that the laser now hits the first sample at the same location that the reference was previously. The reflected beam should be coincident with the mark from the reference reflection; if it is not, the screws are tightened or loosened in order to move the image onto the target. This procedure is repeated for the remaining samples.

Once it is time for the measurements, an Al cylinder used as a radiation shield is screwed into place covering the copper sample holder. This shield has holes in it through which light can reach the samples but which will reflect any other radiation that would be incident on the copper. The cryostat is then mounted onto the translating stage with a rubber o-ring to seal the vacuum. This o-ring should be carefully inspected for damage as it tends to wear at the edges, and greased lightly before each use. The cryostat is held in place by six threaded rods that are bolted on each side. As the cryostat arm that includes the sample holder and the flange that seals the vacuum are not perpendicular to each other for some reason, the bolts must be left loose on one side so that the cryostat arm and sample holder remain centred in the sample chamber.

With the cryostat installed and sealed, the evaporator plate is screwed into the evaporator (see below) and the leads tested for grounds. The evaporator box is mounted onto the bottom of the sample chamber and sealed into place. At this point, the sample chamber can be evacuated using the mechanical pump and the turbopump. There is a window between the sample chamber and the spectrometer itself to keep the two vacua isolated; this window must be correct for the spectral region of interest to ensure that it is both transparent and contains no absorption features in these frequencies.

With the pumps switched on, the sample chamber must be pumped for at least three hours to ensure good vacuum, or until the pressure gauge reads below 5 mTorr. The transfer line to the liquid helium storage dewar can then be inserted into the cryostat to begin cooling. Once this is done, with the detector in position, the correct beamsplitter for the spectral region of interest installed in the spectrometer, and the source activated, the reference is moved into the light path and the collection mirror adjusted so that the signal at the detector is maximized. At this point, the elliptical mirror that shines the light onto the mirror should be moved as little as possible to avoid having light fall on the aluminium radiation shield.

If the spectral region under consideration is the mid-infrared (MIR) or above, the auto-align function of the Bruker can be used to align the fixed mirror in the interferometer to maximize the signal. This tilts the mirror to ensure the greatest overlap of the two beams in the interferometer at the sample, and uses the detector interferogram signal to determine when it has the optimal alignment. The sample positions are then optimized: the cryostat is moved so that the next sample passes the light path, and then is slowly lowered into the beam until the detector signal is maximized. The motor position for each sample is recorded and will be fixed from this point on, though this step will be repeated for the reference at each temperature point down to 50 K (below which thermal expansion effects are negligible).

Once the signal has been maximized at the detector, the alignment is complete.

3.2.2 Temperature dependent measurements and the self-reference method

The measurement system used for these experiments is capable of achieving low temperatures with high stability. Temperature stability is not crucial in many cases as reflectance changes in the far infrared at very low temperatures are generally negligible over a degree or two. In the case of URu_2Si_2 however, in the HO or AFM state the depth of the absorption can change by a factor of 2 or more depending on how close to the transition the measurement is. Temperature stability must be better than 0.1 degrees.

A large dewar of liquid helium is used to cool the sample. A transfer line is inserted into the dewar, carefully controlling the pressure in the storage dewar as the transfer line is lowered into the liquid. The other end of the transfer line is inserted into the cryostat so that the liquid helium contacts the metal surface of the cryostat base. Into this is screwed a large copper sample holder that exchanges the heat between the sample cones and the liquid helium cryogen. A helium return line is connected to the storage dewar in order to release the pressure that slowly builds up, and another is connected to the cryostat exhaust port.

The temperature is controlled by means of balancing the heat applied by the heater and the cooling provided by the helium. Stabilizing the temperature is done using a PID controller attached to the heater. The PID settings are adjusted according to the temperature desired, as the response to changing heat input depends on the temperature. The response to greater heat input is much faster at low temperatures, both because of the small heat capacity and the much smaller temperature gradients once equilibrium has been achieved at low temperature.

In order to get good data at low temperatures that show the temperature-dependence of the material, two competing priorities need balancing. The first is that, on the one hand, scanning for longer times reduces noise. On the other hand, scanning for too long can introduce drifts to the system, as tiny changes in the equilibrium temperature of the detector can shift the baseline of the measurements; small changes in temperature slightly affect the optical path, and so on. The length of time spent scanning needed to achieve low noise also depends heavily on the physical size of the sample. For most samples with areas on the order of 5-10 mm^2 as little as five minutes scanning time yields noise less than 0.2%, but for smaller samples or when greater accuracy is needed scanning times as long as 15 minutes can be used.

The translating stage that moves the samples into the measurement position can accurately reproduce the position of the motor, but the sample itself can have tiny variations in its position due to the looseness of the chain that turns the threaded rods, slipping of the stage on the rods, or other factors. Because of this, there is inevitably greater noise in the measurements of a sample after motion. In order to avoid this problem, temperature ratios are measured using what I call the "self-reference" method.

The procedure for doing this is as follows: the sample position is held fixed while a complete reflected spectrum is measured on the sample at a chosen reference temperature. When measuring a phase transition, this reference temperature must be above the transition temperature but not so high that thermal expansion of the sample holder becomes important. The temperature is then lowered to the base temperature of the apparatus, around 8 K depending on the stability desired. A complete spectrum is measured on the sample at the lower temperature, taking care to allow the temperature to stabilize within at most 0.1 K. The sample is then warmed back up to the reference temperature and another complete spectrum is measured.

The only variations between the spectra at the reference temperature and lower temperature will be due to real physical effects and "drifts" in the system (drift being a catch-all term for the various ways the baseline can shift due to temperature variations, optical path changes, and so on). Measuring the sample at the reference temperature twice, before and after the lower temperature of interest, allows me to eliminate the effects of drifting by averaging the two and using the average as the reference spectrum. In this way, the sample at a fixed temperature acts as its own reference sample. This is what is meant by "self-reference".

By using the self-reference method, I achieved signal-to-noise ratios of 500:1 or better on samples as small as 2x2 mm. It also considerably reduces the length of time required for the measurements, by cutting down to a minimum the number of times the mirror needs to be scanned to only when the sample being measured is changed, and cutting down on the number of measurements needed after evaporation (see next section) to only one temperature below 50 K.

The self-reference temperature ratio method works only below about 50 K for several reasons. One is that the thermal expansion of the copper sample holder starts to become important above about 50 K compared with the lowest temperatures. Another is that above 50 K controlling the temperature becomes much more difficult, as the amount of heat required to change the temperature by a few degrees becomes large compared with how quickly helium can be applied to cool the sample.

The difficulty can be mitigated somewhat by changing the temperature very slowly to avoid strong temperature gradients, but above 50 K the time needed to achieve temperature stability becomes much longer than the time over which systematic drifts become important. As a consequence, measurements of the gold mirror are needed at every temperature and the self-reference method no longer works. In addition, the position of the sample in the light beam shifts and the new optimal position must be found by repeating the optimization procedure described above.

3.2.3 The evaporation of a known-reflectance material and the absolute reflectance

In order to account for the variable geometry of the sample, some sort of reference correction is needed. In transmittance measurements this is easy to do; one need only shine the same light through an aperture of the same size without an absorbing

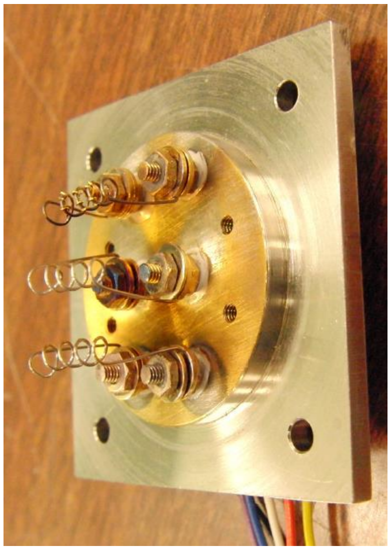

Figure 3.4: The evaporator plate with tungsten filaments wound into coils attached to the mounting screws. Gold wire can be seen wrapped around the coils of the topmost tungsten filament.

sample in the way and the job is done. In reflectance measurements, the challenge is somewhat greater as in practice it is generally not feasible to prepare samples with a specific convenient geometry or to prepare a reference the same size and shape as the sample.

In order to solve this problem, it is convenient to evaporate a material of known reflectance onto the surface of the sample. In most cases, gold is a suitable choice because it evaporates easily and does not bond to the surface of the sample, so it can be removed with a piece of scotch tape and the sample can be re-used without any further work. However, the reflectance of gold, while >99% in the far infrared, falls to ~98% by 10^4cm^{-1} and to only 37% by 2.2 $\times 10^4$cm^{-1}. In measurements of the ultraviolet, then, Al is used instead. Because this is much harder to remove from sample surfaces (and on some samples impossible without polishing) the UV measurements are typically only done after all other measurements are complete.

To evaporate gold onto the sample, a special evaporation chamber is used. Figure 3.4 shows the evaporator plate with tungsten filaments. The evaporator consists of a metal plate through which screws are threaded. The screws are electrically isolated from the metal plate with a vacuum-tight epoxy. Outside the box, wires are attached to the screws that lead to the power supply. On the inside of the box, tungsten filaments that have been wound into coils are held in place around the screws by a pair of washers sandwiched between two nuts.

Preparing the evaporator coils involves considerable work. First, the carbon coating on the tungsten wire must be sanded away, along with any oxidized tungsten. Then, three pieces of gold wire measuring 6 mm in length are tightly wound a minimum of three times each around the tungsten filament approximately 5 mm apart. The tungsten wire is then wound around a hexagonal hex key 3 mm in diameter to make a coil. The ends of the coil must be parallel, and must be bent to wrap around the screws in the evaporator plate. No part of the coil can touch the plate, another screw, or the sides of the evaporation chamber.

There are two principle challenges with the evaporation. The first is determining the correct current to use; the tungsten must heat up enough to melt and evaporate the gold in vacuum, but not so much that the evaporation happens at the wire rather than on the surface of the droplet. If the gold is heated too much the vapour will detach the droplet from the wire before the evaporation can complete.

The second challenge is ensuring that the gold droplets do not run together and fall off of the wire under their own weight. Through careful testing, we determined that for tungsten wire measuring .005 inches thick the procedure should be to use 3 pieces of gold wire separated by approximately one half of a full turn of the coil, and an applied current of 3 A for 20 s followed by 4 A for 10 s. This ensures complete evaporation of the gold. If this procedure is done incorrectly, solid beads of gold will be found in the sample chamber or evaporator box after the experiment is complete.

In order to evaporate gold, the sample must be warmed up. Typically it is warmed to room temperature. This allows temperature stability to be easily maintained while measurements before and after the gold evaporation are carried out to ensure that it has been successful. Occasionally, the reflectance of the reference sample will change slightly after the evaporation. This may be due to a small amount of light hitting the radiation shield that now has gold on it, or to some amount of tungsten being deposited on the reference during the evaporation.

Once the evaporation is complete, the sample is cooled back down and the gold spectrum is measured on the sample at the original reference temperature. The absolute reflectance at the reference temperature is then computed using the following equation:

$$R_{abs}(sample) = \frac{R(sample)}{R(mirror)} \times \frac{R_{evap}(mirror)}{R_{evap}(sample)} \times R_{corr} \tag{3.2}$$

where R_{abs} is the absolute reflectance, R_{evap} indicates the reflectance is measured after gold evaporation (or Al as the case may be), R(sample) is the spectrum reflected by the sample, and R(mirror) is the spectrum reflected by the gold reference mirror. R_{corr} is a correction given by the equation

$$R_{corr} = \frac{R(ref, 295K)}{R_{evap}(ref, 295K) \times R_{abs}(Au, Al)} \tag{3.3}$$

which corrects for any changes in the mirror spectrum due to the evaporation as well as the reflectance of the material evaporated onto the sample surface. The temperature-dependent absolute reflectance of the sample is obtained by multiplying the temperature ratios by the absolute reflectance at the reference temperature:

$$R_{abs}(T) = \frac{R(T)}{R(T_{ref})} \times R_{abs}(T_{ref}) \tag{3.4}$$

It is possible to forego the measurements at room temperature when time is the determining factor, such as a long experiment when helium in the detector is running out. In this case, the evaporation can be done as low as 180 K, the temperature at which water ice sublimates in vacuum (water ice is the last contaminant to sublimate as the sample warms). It is advisable, however, to do the evaporation no lower than 200 K as the rapid warming of the system creates strong temperature gradients and it is impossible to ensure that the sample temperature is the same as the thermometer temperature. Doing this saves an hour or two over warming to room temperature at the cost of being unable to track the success of the evaporation and stability of the reference signal.

3.2.4 Detector preparation and spectral range considerations

Each region of the spectrum has its own combination of beamsplitters, windows, filters, sources, and detectors. Preparing the detectors can range from the relatively straightforward (plug it in, turn it on) to a process that takes up as much as half of the experiment time.

For the mid-infrared and near-infrared, a mercury-cadmium-telluride (MCT) detector is used. MCT is a semimetal with a tunable bandgap, making it ideal for infrared detectors since the bandgap can be tailored specifically to the frequency region of interest and the material is transparent at lower frequencies. In order to use the MCT detector, it is cooled with liquid nitrogen and biased with a pair of large boat batteries. A preamplifier connects the detector to the power supply, and its output is fed into the Lakeshore electronic low-noise lock-in preamplifier.

With the MCT detector, the frequency ranges of interest necessitate the use of a KBr window rather than the polyethylene window used in other parts of the spectrum. This window separates the sample chamber from the spectrometer and must be fully transparent in the frequency range being studied. The KBr window is hygroscopic, however, and must be stored in a desiccator when not in use. If it absorbs water from the air it becomes opaque and must be replaced. The KBr beamsplitter is also used in the MIR region; in the NIR a quartz beamsplitter is used as it is more efficient in the higher frequencies.

The two Si bolometers used in the experiments are very similar, with the exception that one is designed to work at 4.2 K and the other is designed to work at 1.2 K. The IR Labs bolometer is shown in Figure 3.5. Both are cooled with liquid helium (LHe) and the 1 K bolometer is pumped down to lower temperature. The procedure for using them is the same up until pumping the LHe starts.

The bolometer jacket must be pumped until the pressure inside as measured by a vacuum ionization gauge reads 4 x 10^{-5} Torr or lower; using the diffusion pump with the liquid nitrogen trap, however, it should be possible to achieve a vacuum approximately ten times better. It is important that the jacket be opened to the pump as slowly as possible to ensure that the sudden pressure change does not damage the Al foil radiation shielding or the sensitive wiring within.

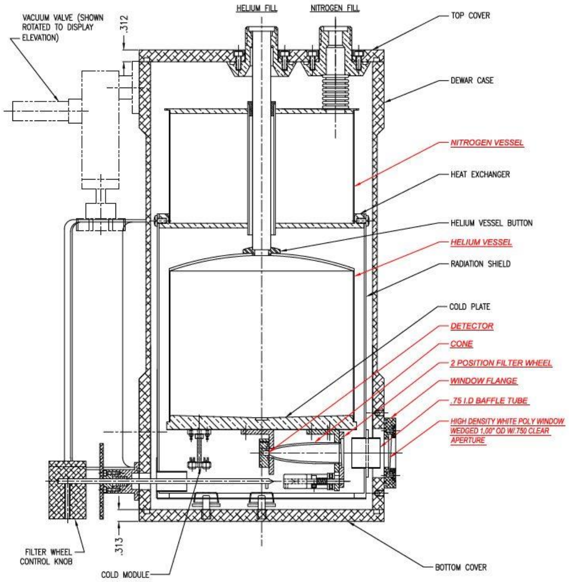

Figure 3.5: The IR Labs bolometer system. This is a representative example, the actual bolometers used vary slightly in model design as well as in modifications (the system depicted here does not have a resistance thermometer on the cold plate, for example). The image is taken from the IR Labs website.

Once the pressure is low enough, the precooling can begin. First the bottom pot (see Figure 3.5) is filled with liquid nitrogen using a long, thin tube that reaches down to the bottom. Once this is filled, the top pot can be filled with liquid nitrogen. The thermometer on the cold plate is used to monitor the cooling; once the resistance is high enough, typically ∼140 Ω, and is no longer climbing, the system has reached thermal equilibrium at liquid nitrogen temperature. The liquid nitrogen is now expelled from the bottom pot using pressurized helium gas; it is essential that the tube used to fill the pot with nitrogen reaches the bottom of the pot so that all of the liquid is expelled. The helium pot is then filled with liquid helium, with the resistance thermometer reading at least 800 Ω once liquid has begun to collect in the pot.

Once the bottom pot is full, the procedure diverges for the two detectors. The 4 K detector has a short piece of rubber hose connected to its exhaust port, to stop any air from getting into the helium pot. The 1 K detector must be pumped, which means connecting the pumping port and slowly opening the helium volume to the floor pump. The resistance thermometer will then climb from 860 Ω to between 7.5 and 11.5 kΩ. It takes several hours for the detector to stabilize at its lowest temperature, and so for the 4 K detector it is usually advisable to let it settle overnight. With the 1 K detector this is not always practical as the holding time is typically only about 20 hours, so for longer experiments repeated scans are used to assess the stability. If the stability is within 0.1% over half an hour, that is sufficient for measurements to begin.

3.2.5 Fault identification and repair

As with so many things, there are more ways for an optical experiment to fail than there are ways for it to succeed. Because of this, a good deal of my time in the lab was spent identifying problems and then fixing them. It is easy to underestimate the difficulty of doing this. In practice it is rarely so simple as looking at an obviously malfunctioning piece of equipment, seeing a broken wire, exclaiming ”well, there’s your problem”, and resolving the deficiency to the cheers of the adoring public. What actually happens is that the noise is too large, or the stability too poor, or the evaporation doesn’t work, or the motor for the translating stage seizes up for no apparent reason. A test protocol must then be designed, the system rigorously and carefully tested, the fault painstakingly isolated, and the defect corrected. Fixing the problem may be as simple as replacing a faulty component or as complex as re-designing part of the measurement system.

Temperature control difficulties are the most persistent and also the easiest to address. One such problem is that over time, the base temperature will gradually creep upwards, so that while once you could achieve 7 K with decent stability, now 12 K is a lucky break. The culprit here is oxidization of the copper sample holder, which over time turns dull and black. Removing the surface oxide with metal polish until it is smooth and shiny immediately corrects the problem.

Stable low temperature measurements often depend on how much liquid helium is actually in the storage dewar. If it is full, the volume available for boil-off gas is small and the pressure inside the dewar rises very quickly, increasing the flow rate of helium in the transfer line. As the flow rate increases, the pressure at the end of the line pushes back on the flowing liquid, creating pressure oscillations that result in wildly swinging temperatures. The heater tries to compensate for this but is unable to change the applied heat quickly enough, and the helium boiling at the heater makes the problem worse. If this happens, the only solution is to reduce the pressure in the storage dewar to $\sim$2 psi or so, raise the temperature of the sample above 20 K, and allow the oscillations to die off before trying to slowly cool the sample to base temperature again, monitoring the pressure in the storage dewar carefully.

Systemic drifts are also a problem that must be overcome for successful measurements. In theory, the reference mirror corrects for drift. In practice, due to non-linearities in the detectors, the correction is imperfect and the reference mirror can only compensate when the drift is at most 4-5%. Initially, when the translating stage system was installed, drifts as high as 20% were observed. This, clearly, simply would not do.

One factor turned out to be poor alignment of the mirrors inside the Bruker. We would align the mirrors on the sample, but when the transfer line was installed it would shift the position of the cryostat slightly and throw the alignment off. Another problem was the position of the storage dewar relative to the cryostat. As the pressure in the storage dewar varies, the transfer line flexes slightly, applying a force to the cryostat and moving the samples. If the transfer line pushes the cryostat in the plane of the light path, the effect is easily ignored. If it pushes side-on, however, part of the reflected image of the sample can shift off of the collection mirror, causing a significant decrease in the amount of light reaching the detector. This appears as a change in the baseline that is not generally constant with time and cannot be effectively canceled out with the mirror.

The alignment of the samples to the reference must be done painstakingly and carefully; this will almost always be the largest source of instability and often doesn't show up as a constant "drift" but rather as an overall inconsistency of the baseline. If the sample image lands on the collection mirror off-centre, so that part of the image is at the edge or even off of the mirror, then tiny shifts in sample position with temperature, dewar pressure, etc. will result in less light reaching the detector. It is crucial that the sample image be centred and be small enough that it does not extend beyond the edges of the collection mirror.

One possible source of trouble is inevitably that the light hits the Al radiation shield that covers the samples. It is usually desirable to have as large a beam of light as possible; this "overfills" the sample, especially for small samples, so that small movements of the system do not significantly change the amount of light reaching the sample. However, if the light beam is too broad, the light will hit the radiation shield. For large samples this will represent a small fraction of the total reflected light and can be largely ignored, but for small samples even a tiny amount of reflection from the shield will result in the reflectance of the Al overwhelming the signal from the sample. There is therefore a delicate balancing act between getting as much light as possible and getting as much light from only the sample as possible. The width of the beam is controlled by an aperture.

Another problem with the beam being too broad is that finding the optimum position for the sample is difficult. As the sample is moved, less light hits the sample itself, but more light hits the shield. The shield is cylindrical so it reflects light in all directions, unlike the flat sample that reflects it straight back towards the collection mirror. But if the sample is small compared to the beam size, the two can result in a comparable signal at the detector. In some cases, it becomes necessary to do the sample positioning entirely by eye, or to move between the theoretical optimal position for each sample (the samples should be 1.008 cm apart by design specification).

Carefully maintaining the detectors is crucial. The MCT detector, used in the MIR and NIR measurement, must be pumped frequently (roughly every four months) with the diffusion pump, as the water ice absorption line at $\sim$3200 cm^{-1} appears in its sensitivity region. The MCT detector is powered by a pair of batteries intended for use in a motor boat and connects to them using a large power box that also serves to charge the batteries. It is vital that the batteries remain fully charged, as they lose their voltage very quickly below full charge and this introduces significant drifts to the system that are not fully compensated by the reference mirror. At low battery voltages the bias too low and the detector ceases to function entirely.

The IR Labs bolometers each have their own unique ways of failing as well. The batteries that are used to bias the detector and the JFET, respectively, can fail and need replacing frequently. The JFET becomes very noisy when the battery begins to fail; the bolometer begins to drift and the non-linearities become even more pronounced. This shows up as "intensity following": two measurements of the reference mirror at different times will have the same characteristic peaks as the spectrum with the beamsplitter fringes. Variations in the temperature of the detector, by as little as a few hundredths of a Kelvin, also cause this effect. For this reason, it is very important to let the temperature of the detector stabilize before measuring, and to keep the liquid nitrogen level as close to full as reasonably possible. At the same time, refilling the nitrogen destabilizes the system for several minutes afterwards, so it must be done during a break in the measurements.

The detectors can fail in more obvious ways as well. Probably the most common fault is a failure to hold liquid helium after filling. If the helium lasts less than an hour, there is a heat leak somewhere and the detector needs to be taken apart. Usually, a piece of foil tape or radiation shielding has come loose and made a contact either between the nitrogen-temperature shield and the outer jacket or between the helium pot and the nitrogen-temperature shield. If the liquid helium lasts for more than an hour, it is more likely that the fill was done incorrectly and there was not very much helium in the pot.

The 4 K detector typically holds helium for at least 40 hours, but when I first started using it the maximum holding time was closer to ten hours. It turned out that the culprit was the Teflon pins that hold the nitrogen shield centred inside the detector. These had broken, and the nitrogen shield was hanging at an angle, very close to one of the jacket walls (though not quite touching). There are also three Teflon rods that hold the helium pot centred inside the nitrogen shield. These had broken as well in both the 1 K and 4 K bolometers. This manifested itself as an extreme sensitivity to external vibrations and a rapid boiling of the liquid nitrogen. The rods were replaced and tightened to hold the helium can (and by extension the detector) stable.

Probably the most frequent point of failure in the experimental system was the evaporation, or at least this has been the case historically. Everything from gold failing to fully evaporate to depositing a purple residue which was probably tungsten on the samples has interfered with the evaporation process. Another problem was trying to ensure an even coating of gold on the samples, without getting any more gold than necessary on them or getting any on the reference mirror. Getting any evaporation products on the reference mirror significantly shifts its reflectance and can affect the baseline considerably.

Initially, shields were used between the tungsten filaments to stop the gold from contaminating the reference, which was made of stainless steel. This caused problems with grounding, however, as the heated tungsten wires would flex slightly, contact the brass shields, and fail to reach sufficient temperature to evaporate the gold. An attempt to solve this using glass or pyrophyllite clay washers to isolate the brass shields from the evaporator plate proved to be too cumbersome and temperamental. Eventually, the shields were removed completely and the evaporation was done without them. The stainless steel reference was swapped for a pure gold one, reducing the change observed after evaporation to typically less than 2%.

The ability to attain and maintain a good vacuum is also a consideration. There are three independent vacuum systems in the experiment: the spectrometer, the sample chamber, and the detector. The detector vacuum can be assessed during pumping for the bolometers, as failure to reach low pressure can mean a leak. The obvious culprit is the window, which is also the most difficult to test as it is permeable to helium and so cannot be leak-checked. Replacing the window is a considerable hassle and so other leaks should be eliminated before doing this. The spectrometer can leak but if the leak is small this is usually not a significant problem, and an easy fix as greasing the o-rings, tightening the lid screws, etc., will usually resolve it.

The sample chamber vacuum is important as a poor vacuum results in ineffective evaporation. It must, therefore, be carefully monitored and maintained. The chief culprit is often the o-ring at the flange connecting the cryostat to the sample chamber. Because of the careful process of tightening the nuts to ensure that the cryostat is properly aligned, it is easy to wind up with a small leak. Another possibility is a tiny leak in the bellows that connects the two parts of the translating stage together. A leak in the sample chamber will make itself known by a sudden jump in the pressure inside the sample chamber upon warming up from low temperature, typically around 60-80 K.

3.3 Measuring the DC resistivity

The zero-frequency limit of the optical conductivity is the same DC conductivity that is measured by transport experiments. As in practice it is not possible to measure light with zero frequency, transport measurements are useful to ensure an accurate extrapolation to zero frequency of the optical data. The measurements were performed using an Oxford Maglab system.

A 4-point contact geometry for measuring DC resistivity was used. This involves using four wires connected to the sample in order to measure the resistance by running a current through the sample and then measuring the voltage. The resistance of the material is then computed using the formula

$$R = \frac{V}{I} \tag{3.5}$$

from Ohm's law, with R the resistance, V the voltage, and I the frequency. The resistivity is a property of the material, however, while the resistance that is measured depends on a number of other factors like sample thickness, applied current, and so on. The resistivity can be computed from the resistance and the size and shape of the sample as

$$\rho = \frac{R \cdot A}{l} \tag{3.6}$$

where A is the cross-sectional area of the sample and l is the distance between the contacts where the voltage is measured.

In order to perform these measurements, thin silver wires must be attached to the sample using either silver epoxy or silver paint. The epoxy or paint must be very carefully applied in order to ensure an even contact and that any stray epoxy does not contaminate the result by giving the current an easier path to flow or changing the sample thickness. In the case of 4-wire measurements, the contact should run the entire thickness of the sample so that the current travels evenly through the sample. If it isn't practical to connect the wires to the entire thickness, epoxy can be used to ensure that the contact covers the side of the sample.

Temperature dependent measurements are taken by cooling the sample to base temperature and then warming it up by applying heat. The temperature is stabilized before the measurements are taken. The challenge here is setting the stability conditions for the temperature. If the computer is over-eager and the time it checks the stability is too short, the measured resistivity will not be at the temperature recorded by the measurements system. Waiting too long for stability, however, makes the stability worse as well as making the measurements take far too long. It is more important to have good stability when the resistivity changes with temperature are large, as is the case in URu_2Si_2.

As the resistivity and the derivative are both desirable quantities, the temperature steps should be very small, especially in regions where the resistivity changes rapidly such as near the phase transition. Taking data too often, however, achieves good temperature resolution but gives larger noise in the derivative and takes far too long (it is not practical to measure for more than a day). In general, T steps were 0.5 K in regions of interest and 1 to 2 K at higher or lower temperatures.

Even once the measurements are complete there will in general be some variation compared with the literature values for both the resistivity and the temperature. Temperature variations are easily fixed, as the transition can be pinned to the known value of 17.5 K for URu_2Si_2, and everything shifted linearly by a degree. Resistivity errors are not so easily fixed, and even within the literature the values typically vary by 20% or more. This is due to uncertainty in the geometry of the contacts and variations in sample thickness. In practice, therefore, some variation in the resistivity (and therefore the height of the Drude peak in optical conductivity) between measurements is unavoidable.

3.4 Analysis of the data

Once the data has been measured, the analysis process can begin. At this point it is still far from being useful for the drawing of conclusions about electrodynamics. Rather, at this point, one has a bunch of absolute reflectances across different frequency ranges. It is still necessary to connect the spectral regions to achieve a single absolute reflectance curve, extract the complex phase of the reflection coefficient, and compute the optical constants.

To assist in data analysis, the datan program suite is used. This is provided by the website of Dr. David Tanner at the University of Florida, and can be found here: http://www.phys.ufl.edu/ tanner/datan.html. Where these programs have been used, it will be explicitly stated that this is so and the method they use to calculate the results described. Within the program folder, the manual man.pdf explains the use and specific functions of the available programs; herein only those actually used in this work are discussed.

3.4.1 Preparing the data for analysis

The detectors each give data over a relatively small region of the spectrum of interest. In order to get a complete reflectance spectrum across the entire spectral range, the different curves must be combined. This is all too often easier said than done, as the region of overlap can be quite small and is usually at the very edge of the detector sensitivities, making it noisy.

Worse still, different bolometer loading effects can affect the sensitivity of the detectors, resulting in data that does not coincide: one reflectance curve will be higher than the other. The response of the bolometer changes with the total amount of signal, or the load, and a large change in the input signal that is sufficient to change the response is called "loading". This typically happens when the reflectance of the sample is much smaller than the reflectance of the gold overcoating and when the intensity of light from the source is very large, so it disproportionately affects the higher frequencies.

The usual procedure is to take the lowest measured frequencies as giving the correct (or nearly correct) values, and then normalizing the other curves at higher frequencies to these. This is usually fairly straightforward as the overlap regions are generally fairly close to linear, but if the slopes are different it becomes more difficult. A program from the datan-win suite called mav.exe can be used to merge the two files together. It normalizes the integrals of the data sets to one another in the overlap region and multiplies the higher-frequency data set to match the lower-frequency data set. It then uses a weighted average function to combine the two together.

3.4.2 The Kramers-Kronig transform

At this point, one has a complete spectrum extending from the far infrared to the ultraviolet, roughly 2.5 meV to 5 eV. There is crucial information missing however: the phase of the reflectance, the imaginary part of the complex reflectance function, remains to be determined.

Fortunately, the real and imaginary parts of the reflectance are not independent of one another. The Kramers-Kronig transform relates the two of them and allows the complex phase to be determined from the real reflectance amplitude. For any linear response function subject to causality, say the conductivity $\vec{J} = \sigma\vec{E}$ that relates the current to the applied electric field, the real and imaginary parts of $\sigma(\omega) = \sigma_1(\omega) + i\sigma_2(\omega)$ are not independent of one another, but rather are linked together by the following relation:

$$\sigma_2(\omega) = -\frac{2\omega}{\pi}\int_0^\infty \frac{\sigma_1(\omega')}{\omega'^2 - \omega^2} d\omega' \tag{3.7}$$

which is the Kramers-Kronig relation. The integral requires knowledge of the real part of the function up to infinite frequency, an impossibility in practice. For discrete data, it becomes a summation done using a computer program.

For the reflectance, the KK transform is evaluated using the program KK.exe from the datan-win suite. The program requires a high-frequency extrapolation and a low-frequency extrapolation and then computes the transform of the reflectance. The high frequency extrapolation can be dealt with in two ways by the program: either taking an assumed value, or using x-ray data at high frequencies. Each method has advantages and disadvantages.

The x-ray data is more accurate, but there is a significant missing region between where the UV data cuts off and where the x-ray data begins. The program must create a "bridge" between the two, and the accuracy of the final result will depend on how good this bridge is. This is done using either a power law in ω, a power law in $1/\omega$, a cubic spline, or a straight line. The fits are to the end of the UV optical data and the lowest frequencies of the x-ray data.

The alternative is to use a high frequency extrapolation without any optical data. The program handles this by taking two values of the reflectance: it is a function of ω raised to a negative power between 0 and 2 up to a cutoff frequency, and thereafter it is taken as proportional to ω^{-4}. The program allows different values of the cutoff and the power of ω to be tried; in practice changing these values makes little difference in the low frequency region, manifesting as a slightly shifted constant background although it can affect the height of features like peaks and phonons.

For most of the data presented here, the latter method is used, with $R \propto \omega^{-1}$ and a cutoff at $\omega = 10^6$. The reason I chose to do it this way is partly because the x-ray optics program didn't become available until part way through and I wanted to keep the analysis consistent, but primarily because when I tried it I couldn't get the bridge section to give sensible values since the reflectance of URu_2Si_2 has been measured to quite high frequency. In any case, the simple extrapolation yielded quite reasonable results and there was no need to go through the tedious process of trying to get the more rigorous method to work only to reproduce what the simpler version could already do.

3.4.3 Low-frequency extrapolation and the DC resistivity

The KK.exe program also requires a low-frequency extrapolation, and this is where some minor problems arise. The problem is that we are drawing conclusions from our data based on the lowest frequencies. The obvious potential, then, is to base the extrapolation on the behaviour we expect to see, and when we see that behaviour taking it as confirmation that the extrapolation was correct in a circular chain of reasoning. Guarding against wishful thinking or the desire to explicitly confirm a prejudice must be done mercilessly.

The options within the kk.exe program for low frequency extrapolations are all based on a particular assumption about the underlying behaviour of the material. As the "DC" reflectance (the reflectance at zero frequency) must be unity for a metal, the only question is how to get from the lowest data point to one at zero frequency. The program uses an extrapolation of the form $R = 1 - A\omega^p$ where the value of p is dependent on the model and A is a fit parameter chosen to make the extrapolation match the data. The simplest is the Hagen-Rubens formula, based on the Drude model, which gives $R \propto (1 - \sqrt{\omega/\sigma})$.

The low-frequency extrapolation is essentially an assumption about the nature (and, by extension, the mechanism) of the scattering at low frequencies. Under the assumptions about the scattering of the Drude model, the Hagen-Rubens formula gives a good approximation to the low frequency reflectance. However, the dominant scattering mechanism may not be simple impurity scattering as assumed by the Drude model. If other scattering mechanisms are involved, the low-frequency reflectance will deviate from the simple form of $1 - \sqrt{\omega}$ of Hagen-Rubens. However, in the very low frequency limit the Hagen-Rubens value is generally close enough for practical purposes.

The kk.exe program allows several other low frequency extrapolations, including marginal Fermi liquid, with $R = 1 - A\omega$, appropriate for cuprate superconductors in their normal state; a two-fluid model for superconductors, with $R = 1 - A\omega^2$ for two electron fluids, one in a superconducting condensate and one in the normal, resistive state; and a model for superconductors with $R = 1 - A\omega^4$. There is also the option to use the DC resistivity to extrapolate to zero frequency using this value.

In practice, what I have done is as follows. I always use the Hagen-Rubens extrapolation to do the KK transform, as the differences between the different techniques are very small since the reflectance is above 90% by the time the extrapolation starts. Then, the low-frequency part is replaced with a Drude peak drawn by "hand" (plotted using the computer), fitted to the measured conductivity at the edge, and with the measured DC resistivity/conductivity input (again by "hand") as the zero-frequency limit. This is then used to calculate the reflectance in the low frequency limit and compared to the Hagen-Rubens extrapolation. If the two agree in the measured region within 1%, this is considered acceptable.

There is a limit to the accuracy of optical measurements, due to the aforementioned considerations related to the detector stability, reference stability, temperature stability, and so on; in practice, there is typically a variation of up to 0.5% in the absolute reflectance between measurements of the same frequency and temperature range on the same sample. While not a significant consideration at higher frequencies, in the very low frequency limit where the reflectance is close to unity small variations can cause large effects in the optical conductivity. In order to combat this, the reflectance is normalized at the lowest frequency (typically below 3 meV) according to the Hagen-Rubens formula using the DC resistivity in the formula. This adjustment is typically a multiplication by a constant on the order of 1 ± 0.003 or less; any more than a half-percent shift and the data is considered flawed and discarded in favour of new measurements.

3.4.4 Fitting the optical conductivity and extracting the electronic gap

The optical conductivity of URu_2Si_2 in the hidden order state shows a distinctive depression followed by a peak that recovers the spectral weight lost in the depression. This is immediately reminiscent of a density wave gap, as seen in Cr (S. Barker *et al.*, 1968) and Bechgaard salts like $(TMTSF)_2PF_6$ (Degiorgi *et al.*, 1996). As a result, a simple model for the Dynes density of states (see previous chapter) is used to give a quantitative measure of the change in the Fermi surface and a reasonable estimation of the value of the gap.

The model used is straightforward. The gap is described by the formula

$$n_D(E) = |Re\frac{E/\Delta + i\gamma}{\sqrt{(E/\Delta + i\gamma)^2 - 1}}| \tag{3.8}$$

which includes parameters Δ for the gap, γ for the quasiparticle lifetime. A cut-off frequency ω_c is introduced when computing the conductivity to account for the bandstructure:

$$\sigma_D(\omega) = Re\frac{1}{\omega}\int_{\Delta}^{\omega_c} n_D(\omega')n_D(\omega-\omega')d\omega' \tag{3.9}$$

The optical conductivity is given by summing over the states above and below the gap, giving the number of available transitions from filled states to empty states.

This model, a Dynes density of states for an s-wave gap with case I coherence factors (as described in the previous chapter) is purely phenomenological in the sense that no assumptions are made about the underlying order parameter or nature of the transition that justify the use of a Dynes model. The microscopic details are not included in any way: the Dynes model is a consequence of mean-field BCS theory and can be derived from a microscopic model but here we just use the result without worrying about the underlying mechanisms. Nonetheless, it is valid for density waves, and the strong incommensurate nesting (Elgazzar *et al.*, 2009; Wiebe *et al.*, 2007) and the structure of the density of states (Park *et al.*, 2012; Chatterjee *et al.*, 2013) suggest that it is a valid description of the phenomenology.

In the fit, there is also a Drude peak that is not explicitly included in the formula above, but was used for fitting the conductivity data. The height of the Drude peak is fixed by the DC conductivity, so this introduces only one other free parameter, namely γ_D the Drude width. In practice, however, the Drude width is constrained by the scattering rate measured and so cannot be fitted arbitrarily.

In order to do the fit, the procedure used was as follows: First, the Drude peak is subtracted from the optical conductivity. The value of γ_D is adjusted in order to keep σ_1 positive. The conductivity that is left is then fitted by varying the values for γ, ω_c, and Δ, with the peak of the spectral weight recovery roughly corresponding to the cutoff, the rise of the conductivity from zero being the gap, and the width determined by the quasiparticle lifetime parameter.

The fits are done by eye: I adjusted each value in order to get the best fits possible. In general, the software I had available had difficulty handling four free parameters across three equations, while using simple fitting algorithms yielded nonsensical results. The quality of the fit was evaluated by computing the residuals up to the cutoff frequency; above this frequency, the details of the bandstructure are not included in this simple model and this region is therefore not considered.

Chapter 4

Optical properties of condensed matter systems

4.1 Introduction

The two scales on which light and solid matter interact are difficult to immediately reconcile. On the one hand, we have the macroscopic properties of materials like dielectric constant and permeability, and Snell's law and index of refraction. On the other hand, we have individual photons with fixed energies interacting with electrons within the energy bandstructure of crystalline solids. The question, then, is how to understand both types of behaviour together and how the macroscopic properties that can be measured by experiment are used to understand the underlying behaviour of interest of the electrons in the material.

4.2 Optical properties of solids

The usual starting point for discussions of electromagnetic waves is the Maxwell equations, and this description will be no different. For electric fields **E**, magnetic fields **B** and charge distributions ρ, Maxwell's equations, in CGS units with μ=1 (since in real materials magnetic effects due to incident light are usually insignificant), are

$$\begin{aligned}
\nabla \cdot \mathbf{E} &= \frac{\rho}{\epsilon} \\
\nabla \cdot \mathbf{B} &= 0 \\
\nabla \times \mathbf{E} &= -\frac{\partial \mathbf{B}}{\partial t} \\
\nabla \times \mathbf{B} &= \frac{4\pi\sigma}{c}\mathbf{E} + \frac{\epsilon}{c}\frac{\partial \mathbf{E}}{\partial t}
\end{aligned} \tag{4.1}$$

In free space this is simple. There is no free or bound charge, no magnetic monopoles, and no currents, so the equations are nicely simplified. In real materials, however, there is some divergence from simplicity. Although free net charge is typically still zero, two quantities account for the properties of the material in Maxwell's equations: the dielectric constant $\tilde{\epsilon}$ and the conductivity $\tilde{\sigma}$. These two generally complex quantities describe the formation of currents due to the electric field and displacement currents due to the time variation of the field, and are related to one another.

Maxwell's equation for the electric field can be re-written as a wave equation

$$\nabla^2 \mathbf{E} = \frac{\epsilon}{c^2}\frac{\partial^2 \mathbf{E}}{\partial t^2} + \frac{4\pi\sigma}{c}\frac{\partial \mathbf{E}}{\partial t} \tag{4.2}$$

which has solutions in the form of plane waves

$$\mathbf{E}(\mathbf{r},t) = \mathbf{E_0}e^{i(\tilde{\mathbf{k}}\cdot\mathbf{r}-\omega t)} \tag{4.3}$$

In vacuum, the phase velocity would be c=ω/k. In a material with current and charge distributions, however, it is

$$k = \frac{\omega}{c}\sqrt{\epsilon + i\frac{4\pi\sigma}{\omega}} \tag{4.4}$$

$$= n\frac{\omega}{c} \tag{4.5}$$

The velocity of propagation is therefore lower in a material than it is in vacuum, by a complex factor of $\tilde{n}$ called the refractive index and defined as $\tilde{n} = \sqrt{\tilde{\epsilon}}$. For convenience this can be separated into real and imaginary parts $\tilde{n}$ = n + iκ. For our travelling wave, this gives

$$\mathbf{E}(\mathbf{r},t) = \mathbf{E_0}e^{i\omega(\frac{n\cdot\mathbf{r}}{c}-t)}e^{\frac{-\kappa\omega\mathbf{r}}{c}} \tag{4.6}$$

which shows why the imaginary part of the refractive index κ is called the extinction coefficient while the real part gives the phase velocity as c/n.

The reflectance relates the intensity of the incoming light to the intensity of reflected light, as

$$r = \frac{\mathbf{E_r}}{\mathbf{E_i}} \tag{4.7}$$

which, at normal incidence and assuming the interface is between the vacuum and the material, with appropriate boundary conditions, gives:

$$r = \frac{1-\tilde{n}}{1+\tilde{n}} \tag{4.8}$$

The relationship between the reflectance coefficient $R = \frac{I_r}{I_i} = (\frac{E_r}{E_i})^2 = r^*r$ and the physical properties of the system is contained in this expression. The reflectance coefficient R is the magnitude of the reflectance, and it is what is actually measured. The reflectance can be written, then, as a real magnitude and a complex phase factor θ

$$r = \sqrt{R}e^{i\theta} \tag{4.9}$$

The reflectance coefficient and phase factor give the real and imaginary parts of the index of refraction as

$$n = \frac{1-R}{1+r-2\sqrt{R}cos\theta} \tag{4.10}$$

$$\kappa = \frac{-2\sqrt{R}sin\theta}{1+r-2\sqrt{R}cos\theta} \tag{4.11}$$

Since the optical conductivity is related to the dielectric function as $\tilde{\epsilon} = \tilde{n}^2 = i\frac{4\pi}{\omega}\tilde{\sigma} + \epsilon_\infty$ the relevant physical properties of the system under consideration, namely the dependence of the optical conductivity (or, equivalently, the dielectric constant) on frequency, are determined from a knowledge of the reflectance coefficient.

4.3 Extended Drude model

In order to interpret optical data, a model is needed. Typically the model used in optics as the basic starting point for describing metallic materials is the extended Drude model. This model uses free electrons interacting with stationary scattering centres as its starting point, and then seeks to calculate the properties such a system should have. It is characterized primarily by the carrier concentration n, the scattering rate $1/\tau$ (given as the inverse of the average time between scattering events τ), and the charge-to-mass ratio of the carriers.

The Drude model starts from free electrons and adds scattering by assuming that the scattering event ”resets” the electron’s momentum. The equation for motion for electrons in the Drude model is

$$\frac{\partial \vec{p}}{\partial t} = -e\vec{E} - \frac{\vec{p}}{\tau} \tag{4.12}$$

which leads to an expression for the current density, $\vec{j} = -en\vec{p}/m$ in terms of frequency

$$\begin{aligned} j(\omega) &= \sigma(\omega)\vec{E}(\omega) \\ &= \frac{ne^2\tau}{m}\frac{1}{1-i\omega\tau}\vec{E}(\omega) \\ &= \frac{\omega_p^2\tau}{4\pi}\frac{1}{1-i\omega\tau}\vec{E}(\omega) \end{aligned} \tag{4.13}$$

This gives the complex optical conductivity

$$\sigma(\omega) = \frac{\omega_p^2}{4\pi}\frac{1}{\frac{1}{\tau} - i\omega} \tag{4.14}$$

subsuming the material properties into the plasma frequency $\omega_p = 4\pi ne^2/m$. The DC conductivity is the zero-frequency limit, $\sigma_0 = ne^2\tau/m$.

In analyzing the optical conductivity obtained from experiments, the Drude model gives an explanation for the existence of the Drude peak, the peak in the optical conductivity at zero frequency. The width of the Drude peak is characteristic of the scattering rate, while the height is just the DC conductivity. The total area under the Drude peak gives the plasma frequency.

The Drude model is exceedingly simple and can be improved in a number of ways. The extended Drude model allows for the scattering rate to be frequency-dependent (as well as introducing a frequency-dependent renormalization to preserve causality that can be interpreted as an effective mass). This incorporates some of the properties of band theory without the need to introduce complicated models.

Optical conductivity measures transitions between states with (nearly) zero momentum change from just below the Fermi energy (occupied states) to just above (empty states), so the conductivity will depend on the density of states at the Fermi level. The effective mass will depend on the energy because the curvature of the band determines the effective mass, and the energy of the incoming light determines what energies within the band transitions can be made at. The scattering rate depends on the energy as well, because the number of states available at each energy determines the availability of empty states to scatter into as well as the availability of carriers for scattering.

To account for these effects, the extended Drude model includes the frequency-dependent scattering rate $1/\tau(\omega)$ in a similar way to the scattering rate in the DC resistivity:

$$\begin{aligned}\rho(\omega) &= \frac{1}{\sigma(\omega)}\\ \rho_1(\omega) &= \frac{\sigma_1(\omega)}{\sigma_1(\omega)^2+\sigma_2(\omega)^2}\\ &= \frac{\omega_p^2}{4\pi}\left(\frac{1}{\tau(\omega)}\right)\end{aligned} \tag{4.15}$$

which is proportional to the optical (frequency-dependent) scattering rate by a factor of $\omega_p^2/4\pi$.

4.4 The electrodynamics of density waves

Density waves are a type of ordered state that occurs when a modulation in the density of a physical quantity serves as the order parameter, such as in a charge density wave (CDW) or a spin density wave (SDW), wherein the distribution of charge or net magnetic moment organizes itself into an ordered pattern. This opens a gap in the density of states at the Fermi level. The CDW is described by a periodic distortion of the lattice with a wavelength related to the Fermi wave vector

$$\rho = \rho_0 + \rho_1 cos(2\mathbf{k_F}\cdot\mathbf{r}+\phi) \tag{4.16}$$

The broken translational symmetry leads to the formation of a gap in the density of states at the Fermi level, a situation well described by mean-field BCS theory. The density of states is given by

$$N(E) = \begin{cases} 0 & E < \Delta \\ \frac{E}{\sqrt{E^2-\Delta^2}} & E > \Delta \end{cases} \tag{4.17}$$

where Δ is the gap.

The electrodynamics of density waves have been established for some time (Lee *et al.*, 1973; Grüner, 1988; Grüner, 1994; Degiorgi *et al.*, 1996). The key features come from BCS theory, which provides the description for the formation of a gap in the density of states at the Fermi level. In the case of superconductivity the gap is formed by the creation of pairs of bound electrons with opposite crystal momentum values. The charge density wave is a similar collective behaviour of electron-hole pairs connected by the wave vector $2\mathbf{k_F}$, so much of the behaviour of superconductors is reproduced in a CDW system. One key difference is that the phase excitation spectrum is gapless in a density wave, pinning the CDW to the lattice and preventing the lossless transport that would otherwise be able to occur.

Typically the optical conductivity behaves in a similar way to the density of states, and a peak in the density of states causes a peak in the conductivity. In superconductors this is not the case due to coherence factors. As the ordering involves states on opposite sides of the Fermi surface, transitions described by $a^\dagger_{\mathbf{k}} a_{\mathbf{k}'}$ and $a^\dagger_{-\mathbf{k}'} a_{-\mathbf{k}}$ are connecting the same two states. The behaviour of the optical conductivity is determined by whether these transitions interfere with each other constructively (case II) as they do for superconductors, or destructively (case I) as they do for density waves. The spectral weight lost in the gap is transferred either to a peak in a narrow frequency region immediately above the gap energy (case I) or into the superconducting condensate as a δ-function at $\omega = 0$.

4.5 The optical properties of heavy fermion systems

Strongly correlated systems are those in which the independent electron approximation breaks down: the assumption that the single-particle states are valid in a multi-electron system is false, and the behaviour of the system is heavily determined by the interactions of the electrons with each other. In the case of heavy fermion materials, this manifests itself as often strikingly normal looking electronic behaviour, but with a linear specific heat coefficient that is many times the value seen in normal metals. This is interpreted as a mass enhancement, and the electronic behaviour is described in terms of heavy quasiparticles that obey single-particle band theory.

The physical origin of the enhanced mass is the hybridization of conduction electrons with a flat (i.e., momentum-independent energy) band of localized f electrons. This is described (Millis and Lee, 1987) by the Hamiltonian

$$\hat{H} = \sum_{k,\sigma} \epsilon_{k\sigma} c^{\dagger}_{k\sigma} c_{k\sigma} + \sum_{i,m} E_{0,m} f^{\dagger}_{i,m} f_{i,m} + \sum_{k,i,m,\sigma} (V e^{ikR_i} c^{\dagger}_{k\sigma} f_{i,m} + H.c.) \tag{4.18}$$

where the first term represents the conduction electrons, the second term is a flat f-band, and the third term is the hybridization between the two bands through an interaction V, in the limit of infinite repulsion between f electrons (i.e. one electron per site). This is analyzed using a slave-boson formalism and a 1/N expansion in order to get the conductivity.

The optical behaviour of heavy fermion systems are widely studied and well established (Millis and Lee, 1987; Dordevic *et al.*, 2001; Degiorgi *et al.*, 2001). Overall,

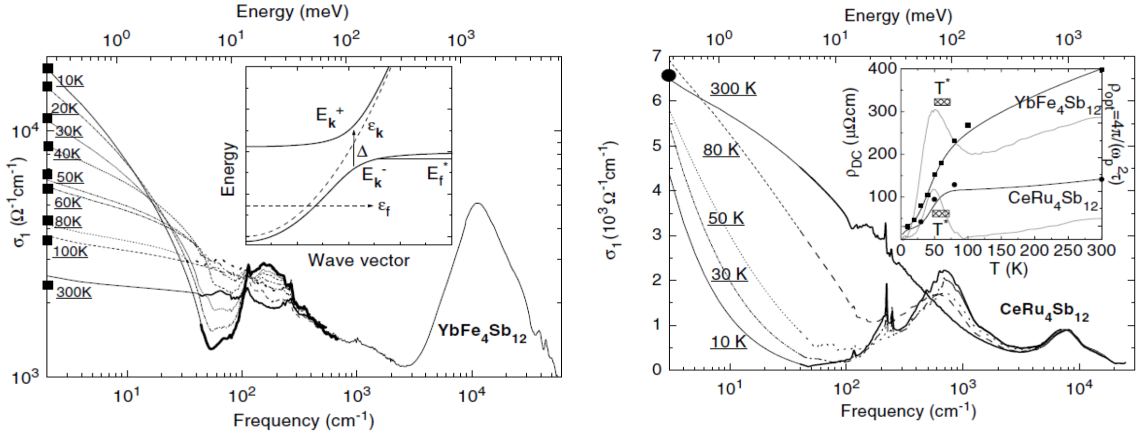

Figure 4.1: Example conductivity of heavy fermion materials. The Drude peak is enhanced as the temperature is lowered, while a depletion of spectral weight above the Drude peak is transferred to a broad spectrum of higher frequencies. After (Dordevic *et al.*, 2001)

they fit well within the framework for understanding the physics of heavy fermion systems. Figure 4.1 shows the optical conductivity of representative heavy fermion materials.

At low frequencies, the dynamical conductivity of heavy fermion systems is understood by considering the conduction electrons as experiencing a renormalized scattering rate and mass due to the hybridization with the strongly-interacting f electrons (Millis and Lee, 1987). Assuming Mathiessen's rule holds and scattering mechanisms are additive (i.e. $1/\tau = \sum 1/\tau_n$), equivalent to assuming that the scattering is momentum-independent, each scattering mechanism can be investigated separately.

For impurity scattering, the conductivity is given by

$$\sigma(\omega) = \frac{ne^2}{m^*}\frac{\tau^*}{1+(\omega\tau^*)^2} \tag{4.19}$$

where $\tau^* = (m^*/m)\tau$ is the renormalized scattering rate. At low frequencies, a

Drude-like peak appears in the conductivity whose spectral weight is given by

$$(\omega_p^*) = \frac{4\pi n e^2}{m^*} \tag{4.20}$$

This gives what is essentially a renormalized Drude model for the optical conductivity in the coherent scattering state.

An important renormalization is the energy scale ϵ_f which is a measure of the renormalized Fermi energy, and is set by the temperature scale on which coherence effects become important so that $T^* \sim \epsilon_f/k_B$. In a heavy fermion material with a coherence temperature on the order of 100 K, the renormalized Fermi energy for the coherent carriers is therefore on the order of 10 meV.

At finite temperatures, scattering of electrons off of bosons is important. The imaginary part of the conduction electron self-energy when the scattering is dominated by bosons is

$$Im\Sigma(\omega, T) = \frac{n_f}{N\epsilon_f}\frac{m^*}{m_b}(\omega^2 + (\pi T)^2) \tag{4.21}$$

which essentially reproduces the results of Landau-Fermi liquid theory, and leads to the description of the system as a heavy Fermi liquid. The scattering rate has the ω^2 and T^2 dependence expected for Fermi liquid theory, where the temperature dependence of $\pi^2 T^2$ is used for the single-particle self-energy measured in ARPES and the factor $4\pi^2 T^2$ is the particle-particle scattering rate seen in optics.

At higher frequencies, the effects of coherence are negligible and the conductivity is flat and nearly frequency independent in this model, while the low frequency part consists of a Drude peak that becomes narrower as the temperature is lowered below

T^*. In reality, what is observed (Dordevic *et al.*, 2001) is that a pseudogap opens as a suppression in the conductivity around the energy of the hybridization gap Δ_H. The sharpening Drude peak cannot account for all of the spectral weight that is lost in this region; much of it is transferred to higher frequencies, often with spectral weight recovery not occurring until $\omega \sim 10\Delta_H$ (Degiorgi, 1999).

Chapter 5

Overview of electrodynamics

This paper was written for a focus issue on hidden order in Philosophical Magazine. In it we summarize the different optical results and draw comparisons between the various optical techniques. We included much data that had already been published elsewhere, by ourselves and others, and the results focus on the analysis and interpretation of the data to give a unified understanding of the electrodynamics of URu_2Si_2.

The hybridization that causes the heavy fermion state to emerge has drawn considerable attention in the literature, as several theories of hidden order suggest that a "precursor" state characterized by order parameter fluctuations should be detectable in the region above the transition. This was, for a time, associated with the measurement (Park *et al.*, 2012) by point contact spectroscopy of a gap opening in the density of states at a temperature well above the hidden order transition. Here we look at the optical evidence for such a state, and find it lacking. The spectral weight of the hybridization gap that opens above the hidden order transition is analyzed in detail and shown to be fundamentally different from that of the hidden order gap. We looked at all of the evidence from optical probes on the hybridization, analyzed their data, and compared them, and concluded that there is no evidence from the hybridization gap of a precursor state.

There is evidence for the onset of a scattering mechanism that strongly resembles Fermi liquid behaviour but with anomalous scaling between the frequency and temperature dependent terms. The scattering rates from both optics and transport are analyzed to demonstrate that this effect precedes the onset of hidden order but happens well within the Kondo lattice state responsible for the heavy fermion behaviour.

The hidden order state is likewise analyzed by looking at all of the optical data that has been published on it. The conclusion is that the data from optics is wholly consistent with a gapping of the Fermi surface that can be described by a Dynes model for the density of states. Furthermore, all of the optical data is consistent with a spin density wave gap or a charge density wave gap, although other techniques rule these out.

For this study, I was responsible for writing the paper. I re-analyzed the data that we had previously taken on this material, including the transport data and the optical data. I analyzed the spectral weight of the hidden order and hybridization states using both our data and that published by other groups. I repeated our analysis and gap fitting procedures on the data published by others, and compared the scattering rates obtained by other groups in the hybridization regime. I constructed a spin density wave model and used it to fit the data and compared the effects of different coherence factors on the gap fitting procedure.

Philosophical Magazine, 2014
http://dx.doi.org/10.1080/14786435.2014.899439

Optical study of hybridization and hidden order in URu_2Si_2

J.S. Hall[a] and T. Timusk[a b *]

[a] *Department of Physics and Astronomy, McMaster University, Hamilton, ON, Canada;* [b] *Canadian Institute for Advanced Research*

(*Received 19 December 2013; accepted 19 February 2014*)

We summarize existing optical data of URu_2Si_2 to clarify the nature of the hidden order transition in this heavy fermion metal. Hybridization develops between 50 K and 17.5 K, and a coherent Drude peak emerges which mirrors the changes in the dc resistivity. The Drude weight indicates that there is little change in the effective mass of these carriers in this temperature range. In addition, there is a flat background conductivity that develops a partial hybridization gap at 10 meV as the temperature is lowered, shifting spectral weight to higher frequencies above 300 meV. Below 30 K the carriers become increasingly coherent and Fermi-liquid-like as the hidden order transition is approached. The hidden order state in URu_2Si_2 is characterized by multiple anisotropic gaps. The gap parameter $\Delta_a = 3.2$ meV in the *ab*-plane. In the *c*-direction, there are two distinct gaps with magnitudes of $\Delta_{c1} = 2.7$ meV and $\Delta_{c2} = 1.8$ meV. These observations are in good agreement with other spectroscopic measurements. Overall, the spectrum can be fit by a Dynes-type density of states model to extract values of the hidden order gap. The transfer of spectral weight strongly resembles what one sees in density wave transitions.

Keywords: heavy-fermion metals; optical properties; URu_2Si_2; hybridization; hidden order

1. Introduction

Optical spectroscopy is an ideal tool for studying the low-energy electrodynamics of strongly correlated metals such as URu_2Si_2. It is a bulk probe, penetrating hundreds of atomic layers into the material; it is therefore not sensitive to surface states. Furthermore, it allows the study of cut and polished surfaces rather than being restricted only to the cleavage plane in the manner of STM/STS and ARPES. Optical measurements can access a very wide range of energies, from the far-infrared (∼2 meV) to the ultraviolet (∼5 eV). They yield direct high resolution (<0.10 meV) spectroscopic information about the energy gaps of ordered states and can be used to extract the spectrum of excitations responsible for the self energy of the free carriers. Optical sum rules can be used to distinguish states by determining where the spectral weight is lost in the gapped conductivity and to where it is transferred: in the zero frequency condensate state for superconductors, just above 2Δ for density waves, or to high frequencies for strong correlation gaps. In URu_2Si_2 the charge carrier dynamics appears to be strongly affected by the hidden order state, and optical spectroscopy is an important tool

---

*Corresponding author. Email: timusk@mcmaster.ca

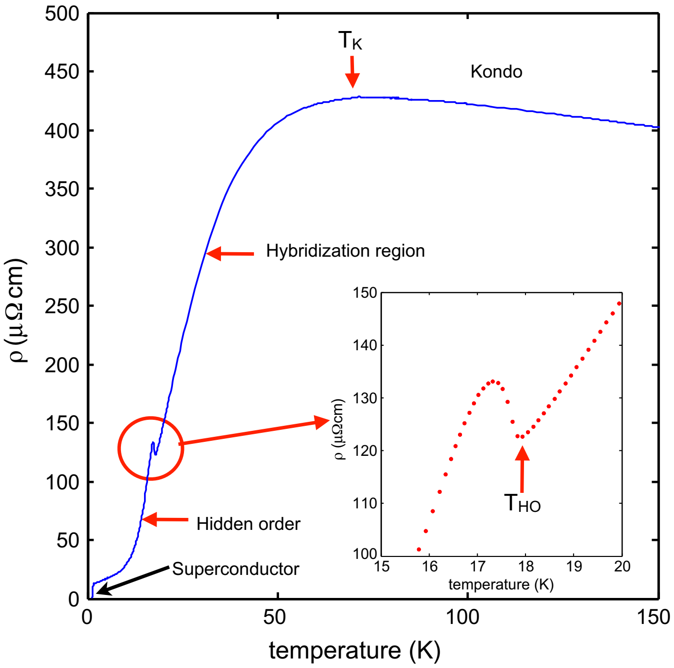

Figure 1. (colour online) The resistivity of URu_2Si_2 from [12]. Above $T_K = 70$ K the resistivity is Kondo-like in that it increases as the temperature is lowered. Below T_K the resistivity drops dramatically as the uranium f electrons begin to hybridize with the s and p electrons. The hidden order transition takes place at $T_{HO} = 17.5$ K and the resistivity rises slightly initially but then drops dramatically as the hidden order gap opens. Finally, at $T_C \sim 1.5$ K, URu_2Si_2 becomes a superconductor. The inset shows the resistivity near the hidden order transition.

for understanding how the charge carrier dynamics evolves from the incoherent state into the ordered state.

Shortly after the first characterization of URu_2Si_2 by transport measurements [1–3], reflectance measurements were performed [4] that revealed the presence of a strong absorption band centred around 5 meV in the ordered phase below $T_{HO} = 17.5$ K. Kramers-Kronig analysis of the reflectance showed that the absorption band was the result of the gradual opening of a gap in the conductivity below the hidden order temperature. The spectral weight lost in the gap was transferred to frequencies just above the gap, typical of a density wave transition. Subsequent optical work has centred around investigations of the effects of doping on the hidden order [5,6], of the effect of hybridization on the electrodynamics [7–10] and the anisotropy of the hidden order parameter [11]. The superconducting state occurs below the temperatures available in typical optical experiments; likewise, the large moment antiferromagnet state (LM-AFM) induced by hydrostatic pressure has not yet been investigated optically.

Figure 1 shows the dc resistivity of URu_2Si_2 [2] as a function of temperature. Four separate regions can be identified. At high temperatures (above 100 K) is the Kondo region where the resistivity rises as the temperature is lowered, a behaviour typical of other heavy fermion systems in which the uranium f electrons are thought to act as localized magnetic impurities that cause large incoherent scattering. At $T_K \sim 70$ K the resistivity begins to drop as the scattering rate begins to decrease rapidly. At the hidden order transition $T_{HO} = 17.5$ K there is a small but distinct jump in the resistivity. In the hidden order state the resistivity

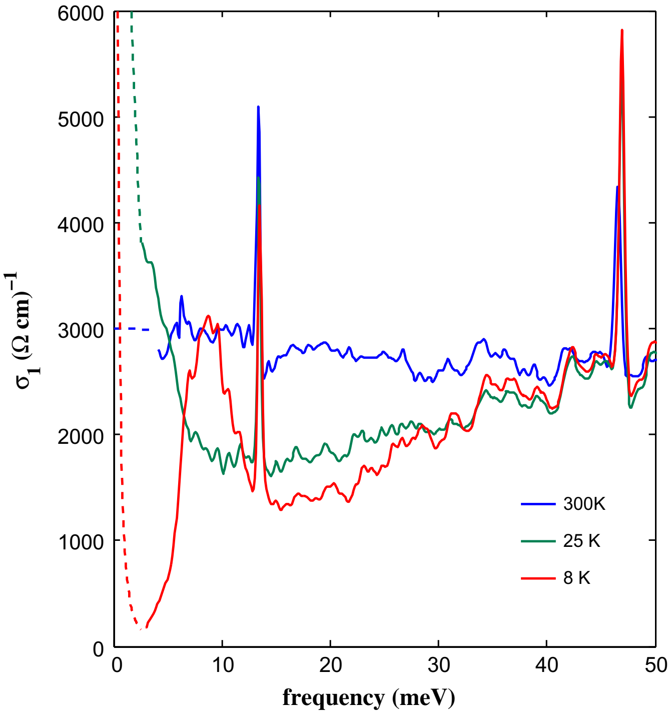

Figure 2. (colour online) The optical conductivity as a function of photon energy in the region dominated by the hybridization gap. Below 4 meV the conductivity has been fitted to a Drude peak whose amplitude agrees with the dc resistivity. Below 10 meV the Drude weight dominates. The spectral weight in the hybridization gap region, 5–40 meV, is lost to higher frequencies. The sharp peaks at 13.5 and 46.9 meV are optically active phonons.

falls further with decreasing temperature, finally falling to zero as the superconducting state is reached, at 1.5 K in pure samples.

In the following, we focus on two regions shown in Figure 1: first, between T_K and T_{HO} where the coherent conductivity first appears, labelled the hybridization region; and second, the region where the hidden order gap appears. We will not discuss the region above T_K where the optical conductivity, shown in Figure 2, resembles many other heavy electron systems [13–18] in their incoherent high temperature state. Here the conductivity is frequency and temperature independent and has a magnitude that approaches the Mott-Ioffe-Regel limit wherein the mean free path of the carriers approaches the interatomic spacing. Also, we will not address the superconducting state, which is not readily accessible to infrared reflectance measurements.

2. Hybridization region

Optical studies of the temperature regime between approximately T_K and T_{HO} reveal a great deal about the evolution of the electrodynamics as the heavy fermion state forms. This is shown in Figure 2, where the optical conductivity is plotted as a function of frequency at three temperatures. As the temperature is lowered the single flat background that dominates at 300 K develops a Drude peak at low frequency and a broad gap-like depression centred at 10 meV. The *c*-axis conductivity is rather higher than that of the *a*-axis, in keeping with

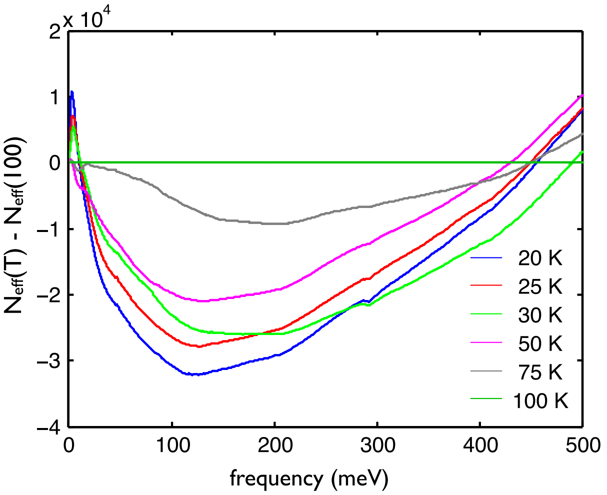

Figure 3. (colour online) Partial spectral weight. The spectral weight below 10 meV is dominated by the Drude peak, which vanishes above 30 K. The curves merge in the 10 meV region showing that the Drude weight does not change much in this temperature region. The high frequency range is dominated by the spectral weight in the incoherent region and the curves join at 450 meV showing that the pseudogap spectral weight lost in the 10–100 meV region is recovered in the 100–450 meV region. Finally there is new spectral weight being added above 450 meV. We attribute this to interband absorption.

transport measurements [11], but is similar in overall features to what is shown in Figure 2. In the heavy Fermion literature this gap-like depression has been identified as the hybridization gap that is expected to develop as the localized *f* electrons hybridize with the mobile *s* and *p* electrons [19]. However, both STM [20,21] and ARPES [22–25] measurements suggest that just above the HO transition there are light carriers and that hybridization may not be complete. As Figure 2 shows, the conductivity at 10 meV has dropped to half its high temperature limiting value and a gap is not completely formed at 25 K. Similar results have been obtained by other investigators [7,10].

With decreasing temperature the Drude peak narrows and increases in height as the scattering becomes increasingly coherent and the dc resistivity decreases. If the *only* change were the development of heavy mass we would expect to see the Drude peak narrow with the lost spectral weight shifted into a Holstein sideband [26], but the height of the Drude peak would remain the same. Clearly, this is not the case in URu_2Si_2. There is another process at work; the carrier mobility is increasing, which by itself would raise the height of the Drude peak but not affect its spectral weight, i.e. the area under the peak. The combination of the two effects gives a Drude peak that is narrowing and increasing in height but also losing some spectral weight to hybridization.

This behaviour, namely the suppression of the background conductivity at higher frequencies and the sharpening of the Drude peak, has been observed in other heavy fermion compounds, such as $YbFe_4Sb_{12}$ and $CeRu_4Sb_{12}$ [15], $CeCoIn_5$ [17], MnSi [16], $CaFe_4Sb_{12}$ and $BaFe_4Sb_{12}$ [18], and UCu_5 and UPd_2Al_3 [6].

Figure 3 shows the partial spectral weight $N_{eff}(\Omega, T) - N_{eff}(\Omega, 100\ \mathrm{K})$, where $N_{eff}(\Omega, T) = \int_0^{\Omega} \sigma(\omega, T) d\omega$, where we have subtracted the partial spectral weight at 100 K over a wider range of frequencies. We see a large loss of spectral weight between 10 meV and 100 meV, and a recovery in the region from 100 to 450 meV corresponding to the formation of the hybridization gap. Very similar data has been presented by Guo et al. [10]. In the context of conventional electron-boson interaction models [26] this energy scale would imply coupling to excitations with energies of the order of 300 meV, much higher than the Kondo scale $T_K \approx 6$ meV. One should note, however, that measurements of spectral weight recovery in the high frequency region are difficult in view of the small changes in the optical conductivity and the possibility of overlapping interband absorption in this region. For example, instead of the expected flattening of the curves above 400 meV, we see a crossing to positive values. In agreement with this view the optical reflectance shows a clear interband feature at 400 meV [11].

It is difficult to estimate the spectral weight of the Drude peak accurately, but in Figure 3 the narrow maximum near zero frequency is the Drude contribution, about a fifth of the large negative arising from the hybridization gap. It was suggested in Nagel et al. that the total spectral weight in the Drude peak is conserved, [9] as suggested by the crossover of the partial spectral weight curves at 10 meV. One cannot rule out *some* changes in Drude weight between T_K and T_{HO}, but any change within the limits of the data would be far too small to explain the large mass seen in the specific heat just above the hidden order transition where $m^*/m = 25$ [3]. Fitting a Drude peak to the high frequency tail of the conductivity down to 2.0 meV (the limit of our data) and the measured dc conductivity, we find little evidence for mass changes above a factor of two. Similar measurements by Levallois et al. [7] show only a slightly larger change in the Drude weight between 90 and 20 K. Another way of estimating the mass change in this region is to use the expression $m^*/m = (V_K/k_B T_K)^2$ where V_K is the zero temperature value of the hybridization gap and $T_K = 70$ K, the temperature where the hybridization starts [15,19]. Since V_K is ill defined in our data, we will use the $m^*/m = 2.5$ from Ref. [7] to find $V_K = 10$ meV. This value for the hybridization gap agrees roughly with the flat region of minimum conductivity in Figure 2 between 5 and 15 meV.

Figure 3 shows only the portion of the spectral weight that is changing between 100 K and the temperature T. There remains a background incoherent conductivity that does not change in this range of temperature. It is difficult to estimate the spectral weight of this component but if it extends up to 0.6 eV it could well explain the γ value of the specific heat. As we will see below, it is this incoherent component that hybridizes at T_{HO}. The original spectroscopy paper of Bonn et al. cited an effective mass of 40 $\sim$ m_e obtained from the limited spectral region available by fitting a Lorentz oscillator to the high frequency data and using this to estimate the plasma frequency, which as a result includes both the Drude component and the incoherent background in the total spectral weight.

Figure 4 shows the optical resistivity $\rho(\omega) = Re\ 1/\sigma(\omega)$ from Nagel et al. [9]. Below 22 K it varies quadratically with frequency (with slight deviations at the lowest frequencies, presumably the result of impurities in the sample raising the dc resistivity) which indicates the onset of purely Fermi-liquid-like behaviour. The resistivity of a Fermi liquid, where electron-electron umklapp scattering is the dominant mechanism, is the sum of two terms, one quadratic in frequency and the other quadratic in temperature [27]:

$$\rho(\omega, T) = A'(\hbar\omega^2 + b\pi^2(k_B T^2)) \tag{1}$$

where the coefficient $b = 4$. This is not what is observed in URu_2Si_2. The observed ratio of the temperature and frequency coefficient b is 1.0 ± 0.1 [9]. Similar deviations from simple electron-electron scattering formula have been reported by Sulewski et al. [14] in UPt_3.

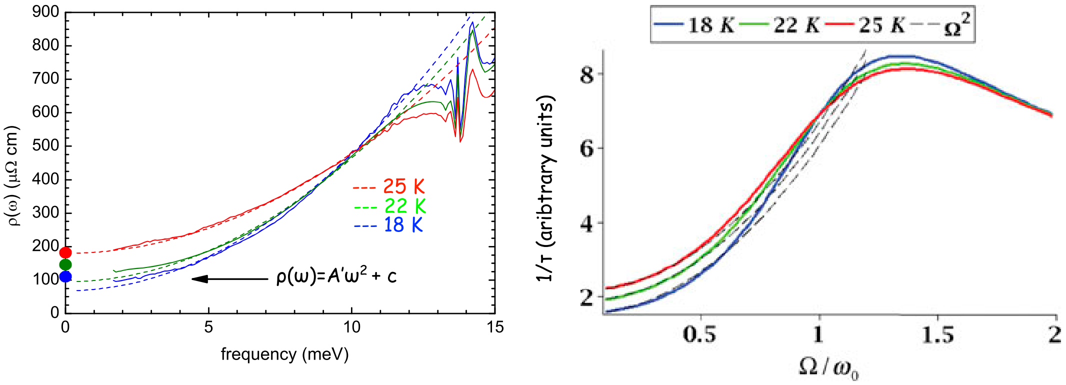

Figure 4. (colour online) The left panel shows the low-energy frequency dependent resistivity $\rho(\omega)$ of URu_2Si_2. The experimental curves (solid lines) are compared to a Fermi liquid fit (dashed lines) with the coefficient *A*' and an offset c(T) determined by a least squares fit to the experimental data. The right panel shows the frequency dependent scattering rate calculated for resonant impurity scattering, with dashed lines showing the fit to Fermi liquid scattering. After U. Nagel et al., PNAS 109 (2012) p.19161, and D.L. Maslov and A.V. Chubukov, Phys. Rev. B 86 (2012) 155137.

A search of the literature shows that virtually all correlated electron materials have a $b < 4$ and that the coefficient b, where it has been measured, varies from material to material from less than one up to 2.5. One way this can be understood is in terms of a suggestion of Maslov and Chubukov [28] of scattering from resonant impurities leading to quadratic frequency and temperature dependence rather than inelastic electron-electron scattering. The coefficient b then lies along a continuum from 1 to 4, with the value determined by the relative strength of the elastic and inelastic scattering. An obvious source of the elastic scattering centres are the un-hybridized uranium f electrons.

The optical resistivity $\rho(\omega, T)$ can be converted to the scattering rate if the plasma frequency is known. We plot in Figure 5 the renormalized scattering rate $1/\tau^*$ based on the Drude plasma frequency of 418 meV at three temperatures from Nagel et al. [9]. At 50 K the scattering rate is flat and does not vary with frequency, a signature of incoherent hopping transport. The dashed line corresponds to the condition $\omega = 1/\tau^*$ for coherent transport. One can then draw the conclusion that coherent transport of the Drude component of the carriers starts below 30 K. This estimate of quasiparticle lifetime can be compared with time resolved ARPES scattering from Dakovski et al. who find a quasiparticle scattering rate of 2.2 meV ($\tau = 301$ fs) in the hidden order state located near the Fermi surface "hotspots". We can identify these quasiparticles with our Drude carriers that have even longer lifetimes at low temperatures. Just above the hidden order transition Dakovski et al. find short-lived quasiparticles with scattering rates of 15 meV (44 fs) at 19 K. Presumably these correspond to the carriers contributing to the incoherent background that hybridizes at 17.5 K.

In addition to the onset of coherence seen in the Drude scattering rate, there is further evidence for changes in the electronic properties at $T \approx 30$ K, well above the hidden order temperature. These features have been attributed to a "pseudogap" in analogy with the cuprate superconductors, where similar signatures are seen. NMR $(T_1T)^{-1}$ [29] shows a depression growing in depth below 30 K. No new optical spectral features are seen at this temperature: the hybridization gap measured in optics develops continuously from 70 K to 17.5 K, as seen by Nagel et al. [9], and any precursors to the hidden order gap would be expected to appear only at very low frequency, below 2 meV. According to Levallois

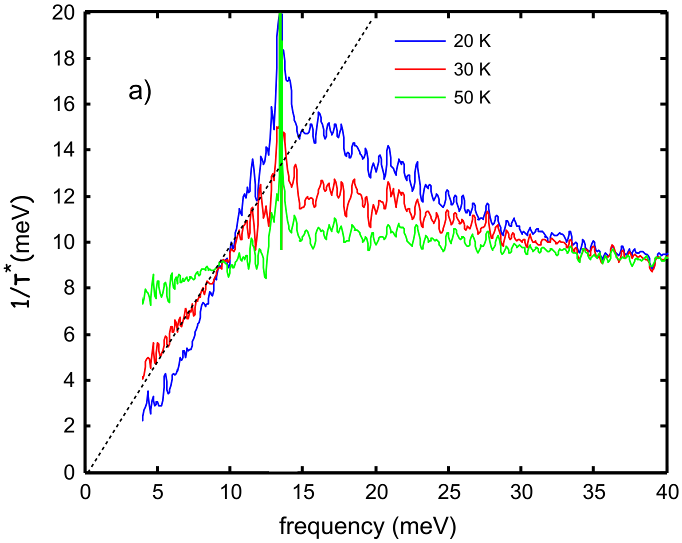

Figure 5. (colour online) The frequency dependent renormalized scattering rate $1/\tau^*$ at three temperatures. As the temperature is raised the Fermi liquid scattering at 20 K is gradually replaced by an incoherent background. Coherent quasiparticles exist below the dashed line $\omega = 1/\tau^*$. This condition is satisfied for T = 30 K. After U. Nagel et al., PNAS 109 (2012) p.19161.

et al. [7] there is a break in the rate of change of the Drude plasma frequency at 30 K as well as the scattering rate – both evolve more rapidly below this temperature. But the dc resistivity does not show any discontinuous kinks between 35 K and 17.5 K, only a gradual flattening of the curve as T_{HO} is approached from above, followed by an upturn below the transition. As shown in Figure 6 the rate of change of dc resistivity acquires a negative component below 30 K but there is no sharp kink. A gap has two opposite effects on the dc resistivity: a reduction in the number of carriers N at the Fermi surface causes an increase in resistivity, but a gap also reduces the number of states available for scattering, reducing $1/\tau$. Just below the hidden order transition it seems that the decrease in N dominates, causing an upturn in resistivity. Well below the hidden order transition the resistivity drops exponentially due to the gapping of final states available for scattering. This is similar to what happens in the high temperature superconductors below the superconducting transition temperature [30]. By contrast, the opposite is true at the cuprate pseudogap where at T^* the resistivity drops which is evidence that the scattering reduction dominates.

As Figure 4 shows there are no distinct bosonic features in the optical resistivity spectra of URu_2Si_2 in the frequency range 2–10 meV, the type of excitations seen in the 40 meV range in many cuprate superconductors, and are associated with peaks in the magnetic fluctuation spectrum [31]. Instead, the excitation spectrum is smooth and has the ω^2 dependence of a Fermi liquid.

Time-resolved THz reflectance measurements [8] also offer insight into the electrodynamics in the coherent regime. Above T_K a single and relatively constant fast decay in the reflectance is observed. As the temperature is lowered below 60 K, this fast decay slows down. This can be attributed to the opening of a partial hybridization gap. At 25 K the single-decay model is no longer accurate, and a two-component (fast component and slow component) decay must be fitted to the data. This is strongly suggestive of the opening of a partial gap at 25 K. The PCS measurements of Park et al. [32] see a partial gap open

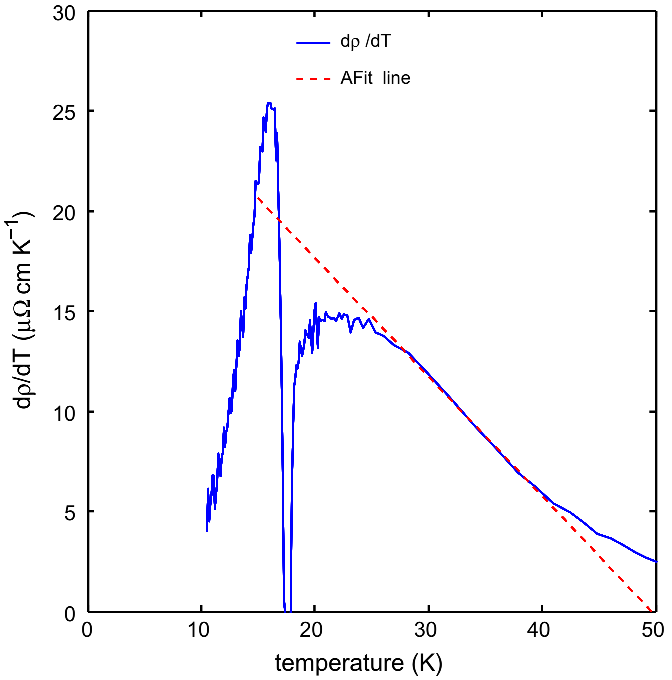

Figure 6. (colour online) The rate of change of dc resistivity with temperature $d\rho(T)/dT$ [12] (solid line). The dashed line shows the trend above 30 K. There is a component that grows below 30 K. As shown in Nagel et al. [9], in this region the transport approaches Fermi liquid behaviour. Within 1 K of the transition this component grows more rapidly. The derivative goes to zero at 17.85 K which we suggest is the hidden order transition, T_{HO}.

below 27 K, also about 10 meV, but they do not see any sharp features at the hidden order transition, and it has been suggested [33] that this may be due to the pressure of the metal tip on the sample. ARPES measurements also see a gap open at the X-point in k-space below 25 K [24]. This gap has a value of approximately 10 meV and is well explained by a simple hybridization model, and furthermore, is associated with a different part of the Fermi surface than the hidden order gap. All of this suggests that this is unrelated to the hidden order state.

In summary, in the state between 50 K and 17.5 K the optical conductivity is dominated by two channels. The first is a coherent Drude channel which is responsible for the changes in the dc resistivity. There is some evidence for an increase in the effective mass of these carriers in this temperature range but not enough to explain the large specific heat coefficient. The second channel has a flat, frequency independent conductivity that develops a partial gap at 10 meV as the temperature is lowered. The spectral weight lost in this gap is recovered at a much higher frequency of 300 meV. This is in broad agreement with other spectroscopic measurements.

3. The hidden order state

Unlike transport measurements, the optical data show no discontinuities at the onset of the hidden order transition. Instead, an absorption feature appears gradually in the reflectance, which shifts to a higher frequency as the temperature is lowered and ends up, in the low temperature limit, at $\omega \sim 5$ meV when measured with light polarized along the a-axis and at $\omega \sim 4$ meV when measured with light polarized along the c-axis [11]. The absorption becomes stronger as the temperature is decreased below T_{HO}. No other optical response is associated with the onset of the hidden order state. The optical conductivity shows that the HO state is accompanied by a gap in the low frequency conductivity; nonetheless, the Drude peak continues to sharpen, indicating that the greatly increased carrier mobility more than compensates for the loss of carriers. The spectral weight that is lost in the gap region is recovered in a peak above the gap energy. In the c-axis conductivity there is clear evidence for the opening of a second gap with a separate, distinct energy. The larger gap in the c-axis is also at a different energy as compared with the gap in the a-axis conductivity. These two observations indicate that the hidden order parameter is anisotropic.

It was initially assumed that the hidden order state was antiferromagnetic, or possibly a spin density wave state [2,3,34], and the early optical measurements of the 1980s and 1990s were interpreted in this framework. Gradually, however, it became apparent that the tiny ordered moment of 0.03 μ_B per U atom was far too small to account for the specific heat data: more entropy was being quenched at the transition, on the order of R ln(2), than could be ascribed to magnetic ordering. More recently it has been argued [35] that the small moment antiferromagnet (SM-AFM) state is extrinsic, caused by strain regions in the lattice, and is not a property of the hidden order state. In addition, when hydrostatic pressure is applied to the crystal, there is a first-order phase transition to the LM-AFM state, further suggesting that the hidden order is unrelated to antiferromagnetism.

Despite this, the optical signature of the hidden order state observable in the conductivity shown in Figure 7 from Hall et al. is strongly reminiscent of a spin density wave state [11] for light polarized parallel to both the a-axis and the c-axis. It was initially noted that the characteristic structure of a suppression of conductivity below the gap energy with spectral weight recovery in a symmetric peak at higher frequency bore a striking resemblance to the spin density wave state in Cr [4,36]. At the time, theoretical descriptions of the SDW conductivity for materials in which the scattering rate is larger than the gap energy were not available, but an estimate could be made for the optical energy gap 2Δ of between 5.5 meV and 8 meV [4]. This was smaller than the specific heat value of 11 meV [3], a first indication that optical measurements and specific heat would come to disagree. In weak-coupling BCS theory there is a universal relationship between the energy of the gap and the transition temperature, given by $2\Delta = 3.53 k_B T_c$. A transition temperature of 17.5 K implies a gap energy of $2\Delta = 5.3$ meV.

Recent measurements of the optical conductivity of URu_2Si_2 [11] reveal the anisotropy of the hidden order parameter in both the different magnitudes of the optical gaps when measured with light polarized along either the a- or the c-axis, but also in the appearance of a second gap, presumably on a different part of the Fermi surface. The strong suppression of the conductivity indicates that a substantial portion of the Fermi surface is being gapped. We know from quantum oscillations [37] that there are four or five Fermi surface sheets in the hidden order state, so presumably the gaps affect each sheet differently. Optical spectroscopy is not a momentum resolved probe, as it is limited to constant **k**-vector transitions and averages over all of k-space for $\mathbf{k} \parallel E$, so the individual components of the Fermi surface cannot separated.

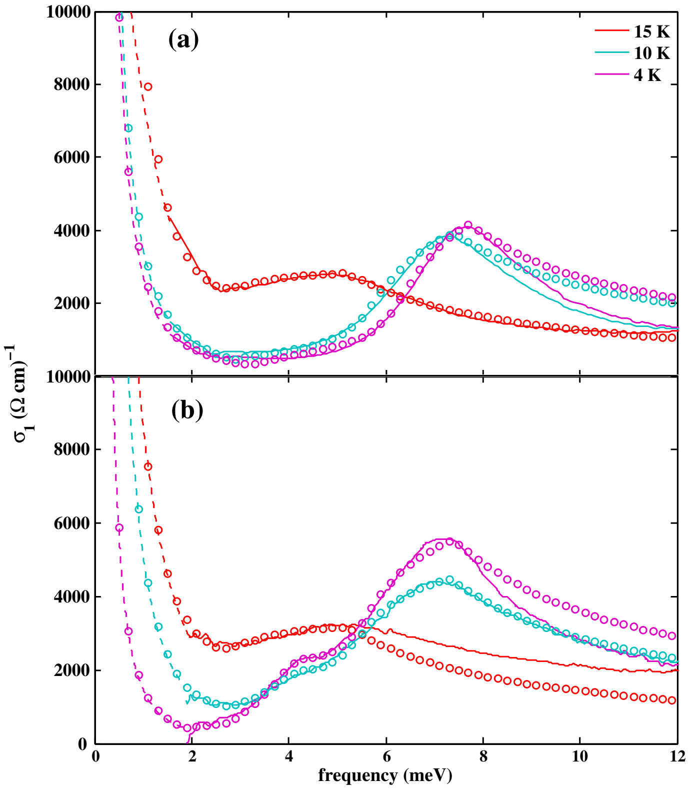

Figure 7. (colour online) Fits of a Dynes model for the density of states to the optical conductivity for the *a*-axis (top panel) and *c*-axis (bottom panel) for selected temperatures in the hidden order state. The dashed lines at low frequency indicate the fit to a Drude model. Circles are experimental points, the lines are the fits. After J.S. Hall et al., Phys. Rev. B 86 (2012) p.035132.

It is possible to fit the measured optical conductivity [11] with a simple Dynes [38] model for an s-wave gap in the density of states:

$$n_D(E) = \left| Re \frac{E/\Delta + i\gamma}{\sqrt{(E/\Delta + i\gamma)^2 - 1}} \right| \tag{2}$$

where a factor of γ has been introduced to account for a finite quasiparticle lifetime, but it can also account for some anisotropy in the gap. When impurity scattering, the frequency-dependent effective mass, and finite quasiparticle lifetime effects are included, the singularity n_D is broadened and the density-wave peak in $\sigma_1(\omega)$ takes on the characteristic shape seen in Cr [36,39] and the Bechgaard salt (TMTSF)$_2$PF$_6$ [40]. The optical conductivity is given by integrating the joint density of states:

$$\sigma_D(\omega) = Re \frac{1}{\omega} \int_{\Delta}^{\omega_c} n_D(\omega') n_D(\omega - \omega') d\omega' \tag{3}$$

In a broken symmetry ground state such as superconductivity or a spin density wave, there are two possible transition processes between any two quasiparticle states. The transition probabilities are determined by coherence factors, which depend on whether the two transition processes interfere with one another destructively (case I) or constructively (case II) [41,42]. The BCS formalism describes both density wave states (case I coherence factor) and superconductivity (case II coherence factor) depending on whether the effective interaction between the quasiparticles changes sign on opposite sides of the Fermi surface (that is, when going from **k** to −**k**). The model above uses a simplified Dynes density of states with broadening to reproduce the qualitative features of the conductivity and extract a reasonable estimate of the gap in the hidden order state. It has been noted [10] that $\mathrm{URu_2Si_2}$ is an almost archetypical example of a case I coherence factor. Indeed, a theoretical calculation of the optical response of heavy Fermion spin density wave materials [43] noted that, of all of the candidates, $\mathrm{URu_2Si_2}$ was the only material that perfectly matched the calculated optical conductivity.

In many ways, this makes a great deal of sense. The gapping of incommensurate magnetic excitations at the hidden order transition has been shown by neutron scattering [44,45], and these account for much of the entropy lost. Band structure calculations [46,47] have yielded a picture of the Fermi surface with strong nesting in the pressure-induced antiferromagnetic state, and quantum oscillation measurements [37] demonstrate that there is no significant Fermi surface restructuring between HO and LM-AFM, which implies that the Fermi surface calculated for the latter state applies equally well to the former. Incommensurate nesting will lead to the formation of a spin-density wave gap at ϵ_F and will be accompanied by a sharp absorption feature in the optical data [6,48], while a commensurate antiferromagnetic order of the localized moments would not be visible in optical measurements because it would not lead to a gap in the excitation spectrum at ϵ_F.

An analysis of the spectral weight N_{eff} transfer in the hidden order region [10] tells the story of what happens as the material transitions from the incoherent to the coherent and then hidden order state. The hybridization transfers spectral weight to higher frequencies, above 300 meV. In contrast, the hidden order transfers spectral weight into the peak immediately above the gap region. However, the spectral weight above the peak in the HO state is not equal to the spectral weight in the coherent state at 20 K. This effect is difficult to quantify precisely, however, as much depends on the choice of plasma frequency for the Drude weight and how the Drude peak is determined below the measurement region (typically ∼2.5 meV).

The temperature dependence of the gap parameter Δ as determined by fits to the Dynes function is shown in Figure 8. The upper panel (a) shows the *ab*-plane gap and the lower panel (b) the *c*-axis (larger) gap. The solid lines are guides to the eye, extrapolated to zero at the temperature of the HO transition at 17.5 K. The inset shows the expected mean field theory gap energy $2\Delta = 3.5k_BT_{HO}$. It is clear that the data do not support the mean field dependence. It must be noted, however, that the presence of multiple gaps of different magnitudes can lead to deviations from the mean field temperature dependence of the order parameter [49]. Such a scenario may account for the temperature dependence of the hidden order gap in $\mathrm{URu_2Si_2}$.

The limiting value at low temperature from Hall et al. [11] for the *ab*-plane gap of $\Delta_{ab} = 3.2$ meV is in reasonable agreement with the work of other investigators if one takes into account possible variations that can be attributed to different criteria for the gap location. Two gaps are seen for $E||c$ at 2.7 meV and a lower one at 1.8 meV. Bonn gives a range from Δ = 2.8 meV to 4.0 meV [4], while Guo et al. give Δ = 4 meV [10]. Other techniques yield gaps that have a larger range of variation, in part due to the fact that their resolution is lower than what is common in optics. Both STM [21] and ARPES [22,24] also give gap values of about 4 meV as well as neutron scattering (around 4 meV) [45,50]. Other tunneling data include those of Escadero et al. [51] who find $\Delta = 5.85$ meV. Another way

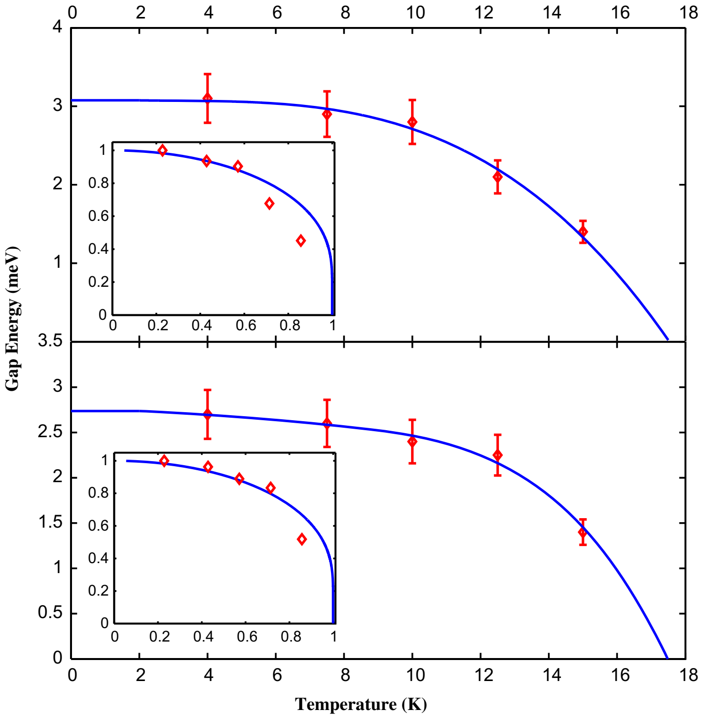

Figure 8. (colour online) The temperature dependence of the gap Δ in the hidden order state as a function of temperature. The upper panel shows **E** parallel to the *ab*-plane; the lower panel, **E** parallel to the *c*-axis. The inset is the mean field temperature dependence $2\Delta = 3.5k_B T_{HO}$, the solid line is a guide to the eye. After J.S. Hall et al., Phys. Rev. B 86 (2012) p.035132.

to find the gap is to fit a Boltzmann factor to various thermodynamic measurements. We will assume that the gap fitted there is 2Δ. Thus the earliest work of Palstra et al. [1], who fit the specific heat coefficient to an activation energy, reports a gap of 115 K, i.e. in our notation, $\Delta = 5$ meV. Mentink et al. [52] fit the dc resistivity in the hidden order state to an activation model and get an *ab*-plane gap of 3.1 meV and *c*-axis gap of 2.2 meV.

In summary, the optical data point to a hidden order state with multiple anisotropic gaps. The non-mean field temperature dependance is in accord with this. The magnitude of the gap parameter Δ agrees with other spectroscopic measurements if one takes into account the lower resolution of ARPES and STM techniques. Overall, the spectrum can be fit closely by a Dynes model with finite quasiparticle lifetimes, and is modelled accurately [43] by a BCS model using type I coherence factors for a spin density wave gap. The transfer of spectral weight is very similar to what one sees in density wave transitions, although one has to rule out a simple SDW picture for the lack of a sufficient ordered moment.

4. Summary and conclusion

We will now try to bring together all the optical data keeping in mind the other spectroscopic results as well. It is natural to discuss the results in terms of the temperature regions defined in Figure 1 but we have to modify the original picture by including a separate "precursor" region between 30 K and T_{HO}.

Between 300 K and 30 K URu_2Si_2 behaves very much like other heavy fermion materials. Above T_K the conductivity is incoherent and increases slightly as the temperature is lowered, reaching a broad maximum around 70 K, and then drops smoothly. We have identified this decreasing conductivity as a combination of f electron hybridization and a general reduction of scattering due to thermal factors. The overall result is a growing Drude peak and a hybridization gap at 10 meV. However, there remains a substantial incoherent background even at 17.5 K and the hybridization gap is not complete: the conductivity at the minimum at 10 meV has only dropped to half its room temperature value. The scattering mechanism of the Drude component is Fermi-liquid-like in that the frequency dependence is ω^2, but the scattering is anomalous in that is does not follow the scaling expected for electron-electron umklapp scattering. A possible mechanism is resonant scattering from the remaining un-hybridized f electrons. There are no dominant features in the optical spectra from bosonic interactions as seen in the cuprate [31] and the pnictide [53] superconductors in the normal state above their superconducting transition temperatures.

Below 30 K, several things happen. There is a break in the rate of change of the Drude plasma frequency, and the rate of change of the dc resistivity begins to deviate from linearity. As the temperature is lowered further, time resolved THz spectroscopy, point contact spectroscopy, and ARPES all show evidence for the opening of partial gaps in the electron excitation spectrum. None of the measured effects that begin between 30 K and T_{HO} are discontinuous at the hidden order transition, and ARPES sees a gap open on a different part of the Fermi surface at T_{HO}. This strongly implies that the changes in the electronic structure in this temperature range are unrelated to the hidden order state.

Below T_{HO} several things happen. A gap opens up and within a fraction of a degree Kelvin the resistivity increases due to a loss of states. But as the temperature is lowered the reduced scattering becomes more important and the resistivity drops exponentially. A gap in the optical conductivity opens up and the gapped spectral weight is transferred to a narrow band just above the gap. It should be noted that it is the *incoherent* non-Drude part of the conductivity that is gapped, but above 12 meV the conductivity remains at its normal state value. This is consistent with hybridization stopping at the hidden order transition while above the frequency of the hidden order gap the carriers remained incoherent. While these dramatic changes take place in the incoherent channel of conductivity, the Drude peak narrows but does not show any large discontinuous changes in width at the hidden order transition.

Acknowledgements

We thank the following colleagues for helpful discussions: Bill Buyers, Jules Carbotte, Andre Chubukov, Piers Coleman, Seamus Davis, Gabriel Kotliar, Brian Maple, Dmitrii Maslov and Peter Oppeneer. In particular we owe thanks to Nick Butch for allowing us to use his high resolution resistivity data shown in Figures 1 and 6. Much of the work shown here was done in collaboration with Urmas Nagel and Toomas Rõõm in Tallinn, Estonia and Ricardo Lobo in Paris. This work was supported by the Natural Sciences and Engineering Research Council of Canada and the Canadian Institute for Advanced Research.

References

[1] T.T.M. Palstra, A.A. Menovsky, J. van den Berg, A.J. Dirkmaat, P.H. Kes, G.J. Nieuwenhuys and J.A. Mydosh, Phys. Rev. Lett. 55 (1985) p.2727.

[2] T.T.M. Palstra, A.A. Menovsky and J.A. Mydosh, Phys. Rev. B 33 (1986) p.6527.

[3] M.B. Maple, J.W. Chen, Y. Dalichaouch, T. Kohara, C. Rossel, M.S. Torikachvili, M.W. McElfresh and J.D. Thompson, Phys. Rev. Lett. 56 (1986) p.185.
[4] D.A. Bonn, J.D. Garrett and T. Timusk, Phys. Rev. Lett. 61 (1988) p.1305.
[5] S. Thieme, P. Steiner, L. Degiorgi, P. Wachter, Y. Dalichaouch and M.B. Maple, Europhys. Lett. 32 (1995) p.367.
[6] L. Degiorgi, S. Thieme, H.R. Ott, M. Dressel, G. Grüner, Y. Dalichaouch, M.B. Maple, Z. Fisk, C. Geibel and F. Steglich, Z. Phys. B 102 (1997) p.367.
[7] J. Levallois, F. Levy-Bertrand, M.K. Tran, D. Stricker, J.A. Mydosh, Y.K. Huang and D. van der Marel, Phys. Rev. B 84 (2011) p.4420.
[8] M.K. Liu, R.D. Averitt, T. Durakiewicz, P.H. Tobash, E.D. Bauer, S.A. Trugman, A.J. Taylor and D.A. Yarotski, Phys. Rev. B 84 (2011) p.161101.
[9] U. Nagel, T. Uleksin, T. Rõõm, R.P.S.M. Lobo, P. Lejay, C.C. Homes, J. Hall, A.W. Kinross, S. Purdy, T.J. Williams, G.M. Luke and T. Timusk, PNAS 109 (2012) p.19161.
[10] W.T. Guo, Z.G. Chen, T.J. Williams, J.D. Garrett, G.M. Luke and N.L. Wang, Phys. Rev. B 85 (2012) p.195105.
[11] J.S. Hall, U. Nagel, T. Uleksin, T. Rõõm, T. Williams, G. Luke and T. Timusk, Phys. Rev. B 86 (2012) p.035132.
[12] N. Butch and M. Maple, J. Phys.: Condens. Matter 22 (2010) p.164202.
[13] F. Marabelli, G. Travaglini, P. Wachter and J. Franse, Solid State Comm. 59 (1986) p.381.
[14] P.E. Sulewski, A.J. Sievers, M.B. Maple, M.S. Torikachvili, J.L. Smith and Z. Fisk, Phys. Rev. B 38 (1988) p.5338.
[15] S. Dordevic, D.N. Basov, N.R. Dilley, E.D. Bauer and M.B. Maple, Phys. Rev. Lett. 86 (2001) p.684.
[16] F.P. Mena, D. van der Marel, A. Damascelli, M. Fäth, A.A. Menovsky and J.A. Mydosh, Phys. Rev. B 67 (2003) p.241101.
[17] E.J. Singley, D.N. Basov, E.D. Bauer and M.B. Maple, Phys. Rev. B 65 (2002) p.161101.
[18] J. Sichelschmidt, V. Voevodin, H.J. Im, S. Kimura, H. Rosner, A. Leithe-Jasper, W. Schnelle, U. Burkhardt, J.A. Mydosh, Y. Grin and F. Steglich, Phys. Rev. Lett. 96 (2006) p.037406.
[19] A.J. Millis and P.A. Lee, Phys. Rev. B 35 (1987) p.3394.
[20] A.R. Schmidt, M.H. Hamidian, P. Wahl, F. Meier, A.V. Balatsky, J.D. Garrett, T.J. Williams, G.M. Luke and J.C. Davis, Nature 465 (2010) p.570.
[21] P. Aynajian, E.H. da Silva Neto, C.V. Parker, Y.K. Huang, A. Pasupathy, J.A. Mydosh and A. Yazdani, PNAS 107 (2010) p.10383.
[22] A.F. Santander-Syro, M. Klein, F.L. Boariu, A. Nuber, P. Lejay and F. Reinert, Nature Phys. 5 (2009) p.637.
[23] R. Yoshida, M. Fukui, Y. Haga, E. Yamamoto, Y. Onuki, M. Okawa, W. Malaeb, S. Shin, Y. Muraoka and T. Yokoya, Phys. Rev. B 82 (2010) p.205108.
[24] F.L. Boariu, C. Bareille, H. Schwab, A. Nuber, P. Lejay, T. Durakiewicz, F. Reinert and A.F. Santander-Syro, Phys. Rev. Lett. 110 (2013) p.156404.
[25] S. Chatterjee, J. Trinckauf, T. Hänke, D.E. Shai, J.W. Harter, T.J. Williams, G.M. Luke, K.M. Shen and J. Geck, Phys. Rev. Lett. 110 (2013) p.186401.
[26] G. Grimvall, *The Electron-Phonon Interaction in Metals*, North-Holland, New York, 1981.
[27] R. Gurzhi, Sov. Phys. JETP 35 (1959) p.673.
[28] D.L. Maslov and A.V. Chubukov, Phys. Rev. B 86 (2012) p.155137.
[29] K.R. Shirer, A.P. Dioguardi, J.T. Haraldsen, J. Crocker, N. apRoberts Warren, A.C. Shockley, C.H. Lin, D.M. Nisson, J.C. Cooley, M. Janoschek, K. Huang, N. Kanchanavatee, M.B. Maple, M.J. Graf, A.V. Balatsky and N.J. Curro, Phys. Rev. B 88 (2013) p.094436.
[30] S. Kamal, R. Liang, A. Hosseini, D.A. Bonn and W. Hardy, Phys. Rev. B 58 (1998) p.8933.
[31] J. Carbotte, T. Timusk and J. Hwang, Rep. Prog. Phys. 74 (2011) p.066501.
[32] W.K. Park, P.H. Tobash, F. Ronning, E.D. Bauer, J.L. Sarrao, J.D. Thompson and L.H. Greene, Phys. Rev. Lett. 108 (2012) p.246403.

[33] J.G. Rodrigo, F. Guinea, S. Vieira and F.G. Aliev, Phys. Rev. B 55 (1997) p.14318.
[34] W. Schablitz, J. Baumann, B. Pollit, U. Rauchschwalbe, H. Mayer, U. Ahlheim and C. Bredl, Z. Phys. B 62 (1986) p.171.
[35] H. Amitsukaa, K. Matsuda, I. Kawasakia, K. Tenyaa, M. Yokoyamab, C. Sekinec, N. Tateiwad, T. Kobayashie, S. Kawarazakif and H. Yoshizawag, J. Magn. Magn. Mater. 310 (2007) p.214.
[36] J.S. Barker, B.I. Halperin and T.M. Rice, Phys. Rev. Lett. 20 (1968) p.384.
[37] E. Hassinger, G. Knebel, T.D. Matsuda, D. Aoki, V. Taufour and J. Flouquet, Phys. Rev. Lett. 105 (2011) p.216409.
[38] R.C. Dynes, V. Narayanamurti and J.P. Garno, Phys. Rev. Lett. 41 (1978) p.1509.
[39] G. Grüner, Rev. Mod. Phys. 66 (1994) p.1.
[40] L. Degiorgi, M. Dressel, A. Schwartz, B. Alavi and G. Grüner, Phys. Rev. Lett. 76 (1996) p.3838.
[41] M. Tinkham, *Introduction to Superconductivity*, 2nd ed., McGraw Hill, New York, 2012.
[42] M. Dressel, *Electrodynamics of Solids: Optical Properties of Electrons in Matter*, Cambridge University Press, Cambridge, 2002.
[43] O.V. Dolgov and M.L. Kulic, Phys. Rev. B 66 (2002) p.134510.
[44] C. Broholm, J.K. Kjems, W.J.L. Buyers, P. Matthews, T.T.M. Palstra, A.A. Menovsky and J.A. Mydosh, Phys. Rev. Lett. 58 (1987) p.1467.
[45] C.R. Wiebe, J.A. Janik, G.J. MacDougall, G.M. Luke, J.D. Garrett, H.D. Zhou, Y.J. Jo, L. Balicas, Y. Qiu, J.R.D. Copley, Z. Yamani and W.J.L. Buyers, Nature Phys. 3 (2007) p.96.
[46] S. Elgazzar, J. Rusz, M. Amft, P.M. Oppeneer and J.A. Mydosh, Nature Mater. 8 (2009) p.337.
[47] P.M. Oppeneer, S. Elgazzar, J. Rusz, Q. Feng, T. Durakiewicz and J.A. Mydosh, Phys. Rev. B 84 (2011) p.241102.
[48] P. Lee, T. Rice and P.W.T.M. Anderson, Phys. Rev. Lett. 31 (1973) p.462.
[49] E.J. Nicol and J.P. Carbotte, Phys. Rev. B 71 (2005) p.054501.
[50] T.J. Williams, Z. Yamani, N. Butch, G. Luke, M. Maple and W. Buyers, Phys. Rev. B 86 (2012) p.235104.
[51] R. Escadero, F. Morales and P. Lejay, Phys. Rev. B 49 (1994) p.15271.
[52] S.A.M. Mentink, T.E. Mason, S. Süllow, G.J. Nieuwenhuys, A.A. Menovsky and J.A. Mydosh, Phys. Rev. B 53 (1996) p.R6014.
[53] J. Yang, D. Hüvonen, U. Nagel, T. Rõõm, N. Ni, P.C. Canfield, S.L. Bud'ko, J.P. Carbotte and T. Timusk, Phys. Rev. Lett. 102 (2009) p.187003.

Chapter 6

The c axis optical conductivity

The optical conductivity of the hidden order state had been studied in the past (Bonn *et al.*, 1988; Degiorgi *et al.*, 1995), but the studies had been focused on the *ab* cleavage plane. In this study, we examined the reflectance spectrum of the *c* axis. The crystal structure is tetragonal, with a *c* axis resistivity that is lower than the *ab* plane by a factor of three or so. Because ARPES and STM studies are limited to cleaved surfaces, infrared spectroscopy is ideally suited to study electronic excitations in this orientation.

We discovered a number of important features of the hidden order state in this study. In particular, the electronic gap is anisotropic, with different values depending on whether the light is polarized along the *c* axis or the *ab* plane. We also reported the first observation of a second gap, presumably on a different part of the Fermi surface, which has since been corroborated by ARPES measurements. Neither of these developments was expected, and this provided additional insight into the electronic structure changes at the hidden order transition.

In addition, we used a Dynes model density of states to fit the gap and were able to study the dependence of the gap on temperature. This resulted in the determination that the electronic gap does not appear to have a mean-field BCS-like temperature dependence. This contradicts conclusions drawn from STM experiments that had to invoke surface effects and modify the transition temperature to fit a BCS gap. This means that either the order parameter does not follow BCS theory or the energy gap does not track the order parameter.

The behaviour and size of the gap allowed us to draw some comparisons to other experiments, in particular to neutron scattering in which we identified the larger FS gap with the gapping of the incommensurate magnetic excitations. This supports the idea that the nesting of the Fermi surface is responsible for gapping the charge excitations as well, despite the absence of spin density wave order.

In this study, I performed the measurements of the absolute reflectance of the c-axis at McMaster. I participated in the measurements of the temperature dependence of the reflectance in Tallinn in collaboration with the team there. I did a number of studies of the surface of the cut crystal and was able to determine the the surface after cutting needed to be treated with HF in order to give good results. I analyzed the data and wrote the paper.

PHYSICAL REVIEW B **86**, 035132 (2012)

Observation of multiple-gap structure in hidden order state of URu$_2$Si$_2$ from optical conductivity

Jesse S. Hall,[1] Urmas Nagel,[2] Taaniel Uleksin,[2] Toomas Rõõm,[2] Travis Williams,[1] Graeme Luke,[1,3] and Thomas Timusk[1,3]

[1]*Department of Physics and Astronomy, McMaster University, Hamilton, ON L8S 4M1, Canada*

[2]*National Institute of Chemical Physics and Biophysics, Akadeemia tee 23, 12618 Tallinn, Estonia*

[3]*The Canadian Institute for Advanced Research, Toronto, Ontario M5G 1Z8, Canada*

(Received 26 March 2012; published 20 July 2012)

We have measured the far-infrared reflectance of the heavy-fermion compound URu$_2$Si$_2$ through the phase transition at $T_{\mathrm{HO}} = 17.5$ K dubbed "hidden order" with light polarized along both the a and c axes of the tetragonal structure. The optical conductivity allows the formation of the hidden order gap to be investigated in detail. We find that both the conductivity and the gap structure are anisotropic, and that the c-axis conductivity shows evidence for a double gap structure, with $\Delta_{1,c} = 2.7$ meV and $\Delta_{2,c} = 1.8$ meV, respectively, at 4 K, while the gap seen in the a-axis conductivity has a value of $\Delta_a = 3.2$ meV at 4 K. The opening of the gaps does not follow the behavior expected from mean-field theory in the vicinity of the transition.

DOI: 10.1103/PhysRevB.86.035132 PACS number(s): 71.27.+a, 74.25.Gz

I. INTRODUCTION

The heavy-fermion compound URu$_2$Si$_2$ has been extensively studied due to the great diversity of electronic behaviors it displays in different temperature regimes. At room temperature, URu$_2$Si$_2$ behaves as a poor metal due to the Kondo effect, with a Kondo temperature of approximately[1] 370 K and a slowly increasing resistivity as the temperature is lowered, reaching a maximum of $\sim$320 $\mu\Omega$ cm at about 70 K. As the temperature is lowered further, the resistivity begins to decrease.[2–5] This decrease has been attributed to the formation of a Kondo lattice where the localized uranium f electrons hybridize with the conduction electrons forming heavy charge carriers with $m^* \sim 25m_e$ in this material, i.e., heavy Fermions.[2,3] This view has been challenged recently by Schmidt *et al.*[6] using STM and confirmed by Nagel *et al.*[7] using infrared spectroscopy, who find that the mass of the charge carriers remains on the order of the free electron mass down to the hidden order transition at $T_{\mathrm{HO}} = 17.5$ K. At this temperature, URu$_2$Si$_2$ undergoes a second-order phase transition, identifiable as a discontinuity in the resistivity[2–5] and specific heat,[8] for which no order parameter has yet been conclusively identified. Finally, from this ordered state, unconventional superconductivity emerges below 1.7 K.[3]

The specific heat data fit well to an exponential decay below the ordering temperature as would be expected in a BCS-like transition, with a corresponding loss of entropy of approximately $0.2Rln(2)$. The dc electrical resistivity data fit well to a Fermi liquid model above the transition, revealing that electron-electron interactions are the dominant scattering mechanism in the coherent regime. There is a pronounced anisotropy between the a and the c directions, with the c direction having a lower resistivity. Below the transition, the dc resistivity fits well to an exponential decay with an additional T^2 term to account for the continued contribution to the scattering from Fermi liquid physics. Recent resistivity measurements[9,10] on ultraclean samples with residual resistivity ratios of 270 or better indicate that the Fermi liquid model fails in the hidden order (HO) state, and that the resistivity is best described by a generalized T^n power law with $n \sim 1.6$ from fitting the data at atmospheric pressure.

Initially, the transition was assumed to be antiferromagnetic ordering[8,11] or the onset of a density wave state.[2] Magnetic ordering was subsequently ruled out by neutron scattering,[12] which detected an ordered moment of 0.03 μ_B per U atom, too small to account for the entropy loss inferred from the specific heat. The alternative of a charge density wave state has received little support since there is no evidence of lattice distortion. Because the order parameter remains unknown the transition has been named hidden order. A number of theoretical models have been proposed to account for the order parameter, such as multipolar ordering, density and hybridization waves,[13–17] but so far none has been conclusively identified as responsible for the transition.

Previous reflectance measurements[18,19] have shown the structure and evolution of the frequency-dependent conductivity, measured in the ab cleavage plane as a function of temperature. Above 75 K, the optical conductivity is completely frequency independent, characteristic of incoherent hopping conductivity. Below 75 K, the spectrum is well described as a metal, with a Drude peak that becomes sharper and narrower down through the hidden order transition. More recently, measurements on an a-c face[20] above the hidden order transition have demonstrated the anisotropy in the optical conductivity expected from transport measurements. Further measurements on the ab plane[7] have recently shown that the spectral weight associated with the Drude peak is constant between 75 K and T_{HO}, suggesting that the effective mass of $5m_e$ remains constant between these temperatures, and that major changes to the electronic structure do not occur in this temperature range.

We have conducted optical spectroscopy measurements on oriented samples of URu$_2$Si$_2$ along both the a and c axes, using a new technique for obtaining high-quality low-noise data. We present the first comparison of optical spectra from both crystal directions on URu$_2$Si$_2$ in the hidden order state.

II. EXPERIMENTAL METHOD

Single crystals of URu$_2$Si$_2$ were grown at McMaster University by the Czochralski method. The crystals were grown in a triarc furnace in argon atmosphere and were then either cleaved perpendicular to the c axis or oriented with a Laue x-ray diffractometer and cut with a tungsten wire saw parallel to the c axis. The ac face was then polished smooth and etched using a wash of hydrofluoric acid to remove any damaged surface after it was found that the polishing process removed the phonon features from the reflectance.

The dc resistivity has been measured along the a axis on crystals from the same growth as those used in the reflectance measurements, and along both axes elsewhere.[4,5,8] The form of the resistivity is robust between different samples, and the values of the resistivity are close enough to one another that it seems more likely that the differences are due to uncertainty in the positioning of the electrodes and the sample geometry during the measurements than variations due to sample quality. When the resistivity at the transition is normalized to agree between the dc measurements taken at McMaster, on a crystal grown at the institute Néel, and in Ref. 5, the values along the a axis agree with one another to better than 10% up to 30 K, and variation on this level does not introduce significant changes to the calculated conductivity. Furthermore, reflectance measurements on different samples with different residual resistivity ratios do not see a shift in the energy of the absorption, so the form of the reflectance is quite robust against sample quality. We therefore use the dc conductivity from Zhu *et al.*[5] for the c axis.

The samples were measured with standard reflectance techniques, using both an immersion cryostat with a ^{3}He bolometer and a Sciencetech SPS spectrometer in Tallinn, Estonia, and an open-flow helium cryostat and Bruker IFS 66 v/s spectrometer at McMaster. A standard gold overcoating technique[21] was used to get absolute spectra accurate to 0.3% and reproducible between the two measurement systems.

In order to interpret the electronic behavior as the gap forms across the Fermi surface at the transition, it is necessary to extract the optical conductivity from the absolute reflectance using the Kramers-Kronig relations. As a first approximation, since URu_2Si_2 behaves electronically as a metal at low temperatures both above and below the hidden order transition, the Hagen-Rubens formula for the reflectance in the limit of low frequencies, $R(\omega) = 1 - \sqrt{(\frac{2\omega}{\pi\sigma_{dc}})}$, has been used to extrapolate the reflectance to zero frequency. The measured dc conductivity was used to compare expected reflectance to that measured. In this case, the measured absolute reflectance was adjusted slightly to agree with the transport data, as slight drifts in the measurement system, particularly the detectors used, can cause errors on the order of 0.5%.

To eliminate geometrical artifacts at low frequency, the sample was held stationary during the measurement process and the temperature was varied. Ratios were then constructed between the reflectance at different temperatures of interest and the reference temperature of 20 K in order to study the temperature dependence the reflectance in the vicinity of the HO transition. Because thermal expansion is negligible on the scale of the optical path and the sample is not moved between measurements, the ratios between the reflected spectra contain very little noise. The temperature ratios are shown in Fig. 1. The full temperature dependence of the reflectance is contained in these ratios, and the low-noise level and high resolution allows weak features to be analysed in detail.

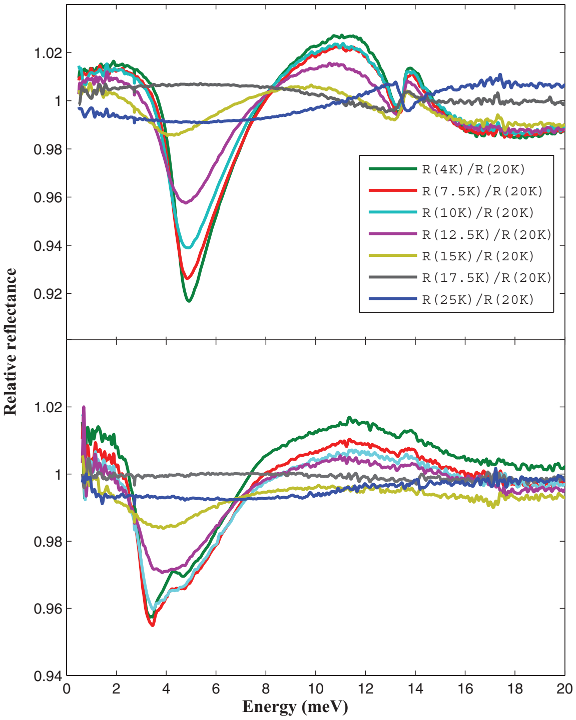

FIG. 1. (Color online) Relative reflectance of the sample for light polarized along the a (top) and c (bottom) axes. The reflected spectrum $R(T)$ is measured at 20 K and then at one of the temperatures indicated, and the ratio $R(T)/R(20\,K)$ is constructed by dividing the reflectance at the temperature of interest by the reflectance at the reference temperature. The sample is held stationary during the measurements so there is little noise.

Geometrical artifacts are introduced to the absolute reflectance during the gold overcoating process due to the motion of the sample, detector drift, and the imperfect reproduction of the original sample position. The noise in the absolute spectra is greater than the noise in the temperature ratios by an order of magnitude. In order to address this, a simple polynomial can be fit to the absolute reflectance at the reference temperature. This smoothed estimate of the absolute reflectance at the reference temperature and the ratios are then combined to give absolute reflectance at the temperatures of interest. This removes weak temperature-independent features if they are within the noise level, but allows the transition and any other temperature-dependent features to be studied with only the much smaller noise from the temperature ratios.

III. RESULTS

The full reflectance in the ab plane is shown in Fig. 2. There are optical phonons at 13.6 and 47.1 meV along the a axis and 42.8 meV in the c direction. Interband transitions can be seen as a shoulderlike feature at 380 and 1200 meV. The feature at 380 meV has a sharper onset at lower temperatures that broadens out at room temperature. The signature of the hidden order can be seen as a strong absorption at 5 meV at the lowest temperature, and it is the only feature within our spectral

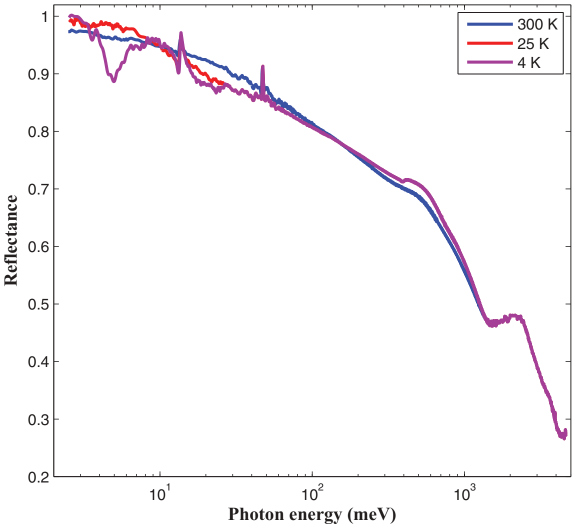

FIG. 2. (Color online) Absolute reflectance measured in the *ab* plane from the far infrared to the ultraviolet. The shoulderlike features at 380 and 1200 meV correspond to interband transitions. The partial hybridization gap appears in the 25 K spectrum as a drop in the reflectance between 15 and 30 meV. The hidden order gap opening causes a strong absorption centered around 5 meV, visible in the 25 K spectrum.

range that can be associated with the hidden order transition. The drop in reflectance between room temperature and 25 K in the region between 12 and 40 meV can be attributed to the formation of a hybridization pseudogap[7,20] below 70 K.

Figure 3 shows the polynomial fit to the absolute reflectance described above, along with the smoothed absolute reflectance along both distinct crystal directions. The onset of the hidden order state is clearly visible in the low-temperature spectrum as a drop in the reflectance of both crystal axes centered around 5 meV (*a* axis) and 4 meV (*c* axis). The minimum is distinct and shifts to slightly higher energies with decreasing temperature. The appearance of this minimum evolves gradually with a sudden onset at the hidden order temperature and its depth increases monotonically with decreasing temperature in the *a* direction; in the *c* direction, there is additional structure that makes this impossible to determine. Along the *c* axis below 12 K, an additional feature appears in the absorption near the minimum, unlike when the light is polarized along the *a* axis whose absorption minimum remains sharp to our lowest temperature of 4 K. No other sharp features appear below T_{HO} above 2 meV.

Figure 4 shows the optical conductivity at selected temperatures. The solid curves above 2 meV show the real part of the optical conductivity from the Kramers-Kronig analysis as described above. $\mathrm{URu_2Si_2}$ behaves electronically as a metal in the low-temperature regime both above and below T_{HO}. To obtain an estimate of the conductivity below 2 meV shown as dashed curves, where we have no optical data, we used the following procedure to fit a Drude peak to the conductivity. The amplitude of the peak $\sigma(0)$ was taken from the measured dc conductivity and the width $1/\tau$ from the tail of the Drude peak that extended to the optically measured region above 2 meV.

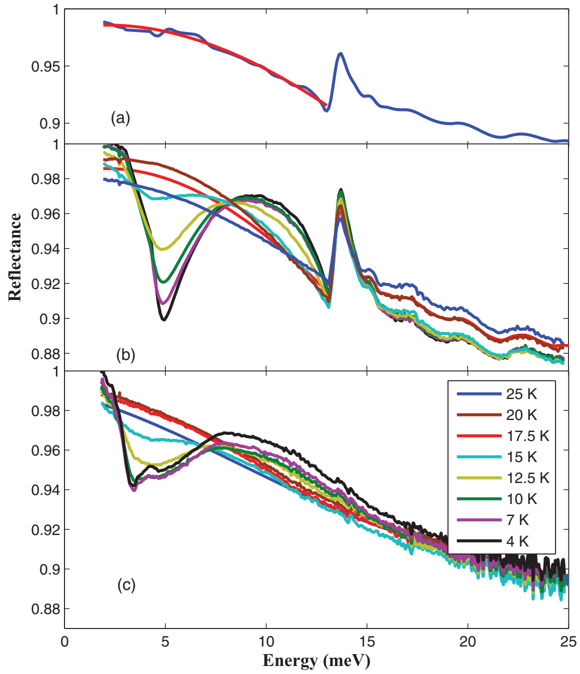

FIG. 3. (Color online) (a) Absolute reflectance in the *a* axis at 25 K, with the polynomial fit (red line) to smooth out geometrical artifacts introduced during motion of the sample. The same procedure was used for the *c* axis (not shown). (b) Refined reflectance along the *a* axis, obtained by multiplying the measured reflectance ratios $R(T)/R(25\ \mathrm{K})$ by the fit to the absolute reflectance at 25 K. (c) Refined reflectance along the *c* axis. At the lowest temperatures, additional structure appears within the absorption around the minimum near 5 meV.

As expected from transport data, there is a strong anisotropy between the optical conductivity in the *a* and the *c* directions. Both have qualitatively the same features above the transition: a sharp Drude peak and strong incoherent background, with the Drude peak becoming sharper as coherence becomes stronger with decreasing temperature. The conductivity is higher along the *c* axis, consistent with dc resistivity measurements.

The gap can be identified as a suppression of the optical conductivity (Fig. 4) in the frequency range immediately above the narrow Drude peak, with a shift of spectral weight to the frequencies in a narrow region above the gap energy, visible as a sharp peak. The Drude peak narrows sharply and increases in height as the gap develops, but the spectral weight lost in the gap region is not fully recovered either in the Drude peak or above the gap. The very strong suppression of the conductivity in the gap region suggests that the gap forms across a large section of the Fermi surface. Qualitatively, the gap structure appears similar in the two crystal directions, although the peak above the gap is broader in the *c* direction and the gap energy is larger in the *a* direction. The structure within the absorption in the reflectance along the *c* axis is visible within the gap region

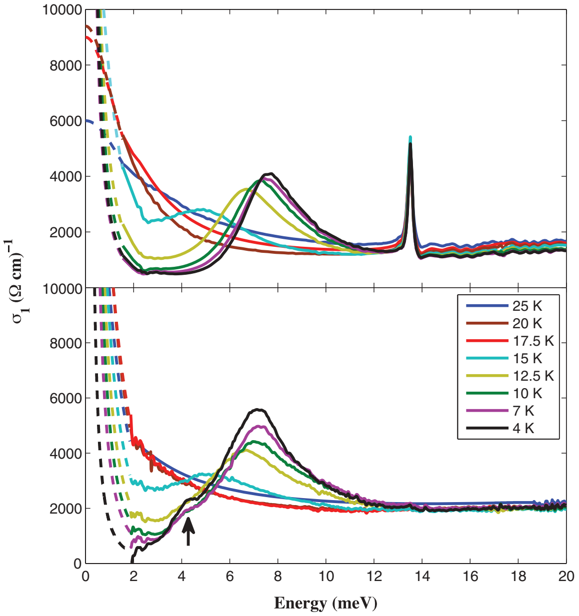

FIG. 4. (Color online) Real part of the optical conductivity of the *a* (top) and *c* (bottom) axes for selected temperatures above and below the hidden order transition at 17.5 K. The arrow in the lower panel shows the position of the second gap at lower temperatures. The dashed lines at low frequency indicate the Drude peak that has been extrapolated to agree with dc conductivity measurements.

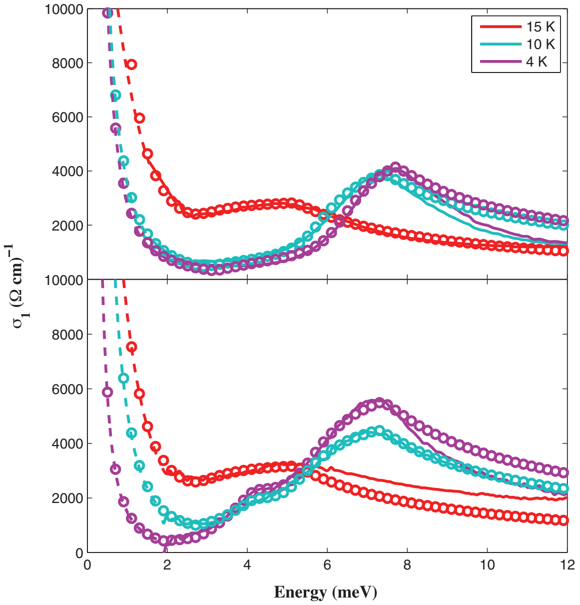

FIG. 5. (Color online) Fits of a Dynes *s*-wave model for the density of states to the optical conductivity for the *a* (top) and *c* (bottom) axes for selected temperatures in the hidden order state. The dashed lines at low energy indicate the Drude model extrapolation, the solid lines are the measured conductivity, and the circles indicate the conductivity calculated on the basis of the *s*-wave model. Above the cutoff energy exact agreement is not expected since the details of the band structure are not taken into account in the fitting process.

in the optical conductivity as an additional bump appearing below 12 K, becoming stronger and sharper as the temperature decreases.

We use an isotropic *s*-wave gap model from Dynes *et al.*[22] with a square-root-like singularity in the density of states to attempt to parametrize the gap seen in the conductivity:

$$n_D(\omega) = \left| \mathrm{Re} \frac{\omega + i\gamma_{\mathrm{qp}}}{\sqrt{(\omega + i\gamma_{\mathrm{qp}})^2 - (\Delta + i\gamma_\Delta)^2}} \right|, \qquad (1)$$

where Δ is the gap energy, γ_{qp} is a damping term due to the quasiparticle lifetime, and γ_Δ is the imaginary part of the complex gap parameter. In order to account for the region in which the density of states goes to zero, a cutoff frequency ω_c is introduced as the upper bound of the integration over the available states:

$$\sigma_D(\omega) = \mathrm{Re} \frac{1}{\omega} \int_\Delta^{\omega_c} n_D(\omega') n_D(\omega - \omega') d\omega'. \qquad (2)$$

The comparison of the isotropic gap model fit to the measured conductivity is shown in Fig. 5 for selected temperatures for both crystal directions. The behavior of the relevant band structure above the cutoff is unknown and the form of the cutoff is somewhat arbitrary and has not been included in the model, so exact agreement above this frequency is not necessarily to be expected.

The energy and the gap both have an imaginary part, γ_{qp} and γ_Δ, respectively. In both polarizations and for both gaps in the *c* direction, the values of both γ's are constant with temperature. The width of the gap was determined to be the same for all three gaps to within 10%. The quasiparticle lifetime is the same for the *a*-axis and larger *c*-axis gaps, but differs for the smaller *c*-axis gap. The values for γ_{qp} due to the quasiparticle lifetime are $\gamma_{a,\mathrm{qp}} = \gamma_{c1,\mathrm{qp}} = 0.1$ meV, and $\gamma_{c2,\mathrm{qp}} = 0.5$ meV.

The appearance of multiple gaps as well as the differences between the gap sizes, observed with different axes of polarization, indicates that the gaps are not isotropic. The isotropic gap model still works extremely well, however, suggesting that the density of states does indeed possess a square-root singularity despite the anisotropy of the underlying gap. The structure of the Fermi surface is complicated with as many as five separate sheets,[23] which makes a reasonable determination of gap structure difficult. Optical measurements are by their nature averages over all of *k* space in the direction given by the light polarization, so variations in the detailed gap structure will not necessarily produce greatly differing optical conductivity.

The *a*-axis gap evolves steadily down into the hidden order state, with a value at 4 K of $\Delta_a = 3.2$ meV in good agreement with ARPES[24] (which sees a heavy band dispersing approximately 4 meV below the Fermi level) and tunneling[25] ($\Delta = 4.1$ meV) as well as previous optical data.[18] The gap in the *c* axis is not easy to compare to other measurements because the material does not cleave along the *ac* face, so surface-sensitive techniques like STM and ARPES cannot be used directly. Our measurements suggest that the additional structure in the c-axis conductivity is due to a second gap opening within the hidden order state. The larger gap has a value of $\Delta_{1,c} = 2.7$ meV, while the smaller gap value is $\Delta_{2,c} = 1.8$ meV, both at 4 K. The isotropic gap model can be fit at all temperatures without changing the quasiparticle widths or lifetimes or the gap width; only the value of the gap needs to be changed to fit the data, except at 15 K where the cutoff frequency has to be decreased slightly.

The gap in the a axis is well described by the single-gap s-wave model fit, while the c-axis requires a two-gap model to be consistent with the data. The second gap seen in the c-axis is too weak to be seen in the 15 K conductivity, but is clearly present at the 12.5 K and is nearly fully developed before it is visible, with a value of $\Delta_{2,c} = 1.5$ meV at $T = 12.5$ K and $\Delta_{2,c} = 1.8$ meV at $T = 4$ K.

IV. DISCUSSION

Figure 6 shows the evolution of the three gaps with temperature, as determined by fitting our model. Neither of the observed gaps whose onset we can detect follow the behavior expected from a mean-field BCS model in the region near the transition, but the fit becomes closer at lower temperatures. It can be noted here that good agreement with BCS theory can be achieved if the transition is assumed to happen at 16 K rather than at 17.5 K, a feature also observed by Aynajian *et al.*,[25] however, transport measurements rule this out and the bulk transition certainly happens at 17.5 K.

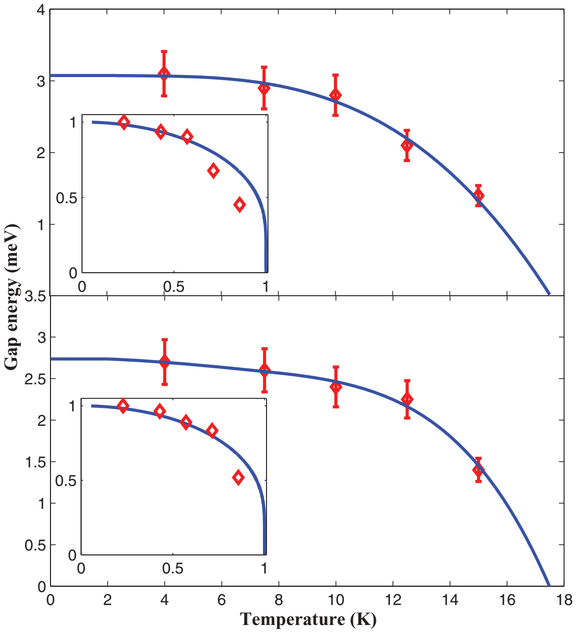

FIG. 6. (Color online) The gap value as a function of temperature for the a-axis (top) and the larger c-axis gap (bottom). Solid lines are guides to the eye to show the trend of the gap values. Insets show the behavior expected from a mean-field BCS model from which the data deviates at temperatures close to the transition; at lower temperatures the behavior is closer to mean-field theory. The smaller c-axis gap is nearly constant to within our sensitivity and is not shown. Error bars are determined from the largest change of gap value that can be made to agree with the data if the other parameters in the model are varied.

Neutron scattering work[26] shows that a series of incommensurate spin excitations corresponding to the wave vectors $(1 \pm 0.4,0,0)$ become gapped at the transition, and this must account for a significant amount of the entropy lost at the transition. The neutron scattering data reveals that charge and spin degrees of freedom are very strongly coupled, and the Fermi surface reconstruction at T_{HO} has a corresponding effect on the spin excitation spectrum. The energy of the a-axis gap seen in optics (3.2 meV at 4 K) is in good agreement with the gap seen in neutron scattering[26] (∼3.5 meV at 1.5 K). This close correspondence suggests that the spin and charge degrees of freedom are strongly correlated and the same gap exists in the charge excitation spectrum as in the spin excitation spectrum.

The neutron scattering results also show commensurate excitations corresponding to the antiferromagnetic zone center that become gapped at the HO transition. This gap has a value of 2 meV at 1.5 K, very close to the observed value of the smaller gap in the c-axis optical data (1.8 meV at 4 K). The oscillator strength in our model associated with the opening of this gap is much smaller than for the a-axis gap; this is also in agreement with INS, which sees the commensurate mode as considerably weaker than the incommensurate modes. This is further good evidence that the gap seen in the optical data is related to the gap in the spin excitation spectrum seen in the neutron scattering.

Band structure calculations[27–29] and quantum oscillation measurements[30,31] have recently revealed much more information about the Fermi surface reconstruction that occurs at the HO transition. Rotational symmetry is broken in the ab plane and the unit cell changes from body-centred tetragonal to simple tetragonal, with a doubling of the unit cell along the c-axis[30] inferred. Strong nesting between different parts of the Fermi surface are responsible for the excitations seen in neutron scattering, which agrees well with the present results. We note that we do not detect any additional zone-boundary optical phonons appearing within the spectrum from the unit cell doubling along the c axis; the feature within the gap structure in the c axis, which we identify as a second gap, can be conclusively ruled out as a phonon.

Recent ARPES[24] measurements and STM results[6,25] show the behavior of the band structure at the transition near the Fermi level. ARPES shows a heavy quasiparticle band that crosses the Fermi level from above at the hidden order transition and hybridizes with a light hole band. Measurements of the differential conductance using STM see a similar effect; a light band breaks into two heavy bands at the transition, forming a gap at the Fermi level. The STM data suggests an effective mass of 5 m_e in the coherence region (in agreement with optical results[7]) increasing to ∼25 m_e in the HO state, while ARPES sees an effective mass of 22 m_e in the HO state.

The STM[6,25] results show a heavy-band splitting at the transition into two heavy bands with a gap of ∼4 meV at the Fermi level. However, when the band splits, there are additional empty states that appear above the Fermi energy with a gap of approximately 2 meV [see Schmidt *et al.*[6]

Fig. 5(c), and Aynajian *et al*. Fig. 4(c)]. This band of empty states is available for transitions from the filled band at the Fermi level, and the gap between these two bands shows close agreement with the smaller gap seen in the optical conductivity measured along the c axis. We therefore suggest that this band accounts for not only the corresponding optically observed gap, but the commensurate spin excitation gap as well.

The origin of the larger gap seen in the c axis is less clear: its value at 4 K (2.7 meV) does not correspond well with any gap seen in neutron scattering. APRES measurements[24] see a heavy quasiparticle band dispersing 4 meV below E_F. STM measurements, likewise, do not see any gaps corresponding to 3 meV between filled states and empty states (though arguably there is a gap between two empty bands of about this magnitude). Both ARPES and STM, however, are limited to measuring a cleaved surface, while we observe this effect only in the c-direction. We suggest that this gap has not been previously observed using the other available probes. The fact that it does not correspond to a gap in the spin excitation spectrum suggests that for the charge carriers involved, spin and charge degrees of freedom are decoupled.

V. CONCLUSIONS

We have measured the optical conductivity of the heavy-fermion compound URu_2Si_2 through the hidden order transition at 17.5 K down to 4 K. We observe several s-wave gaps opening in the Fermi surface; one can be seen in the a-axis conductivity and two others in the c axis. We associate the gap in the a axis with a value of 3.2 meV at 4 K with the gaps seen by ARPES, STM, and neutron scattering with values of $\sim$4 meV, and the smaller gap in the c axis with a value of 1.8 meV at 4 K with the gapped commensurate spin excitations seen in neutron scattering and the band splitting seen in STM. The larger c-axis gap, with a value of 2.7 meV at 4 K, cannot be associated with any previously reported measured gaps in the magnetic excitation spectrum, and appears to be a purely charge gap. The combination of isotropic s-wave gaps with a gradually narrowing Drude peak provides a complete and consistent explanation for the low-frequency optical conductivity in the hidden order state.

ACKNOWLEDGMENTS

We thank K. Behnia, J. C. Carbotte, A. V. Chubukov, P. Coleman, J. C. Davis, B. Gaulin, B. Maple, D. L. Maslov, A. J. Millis, and D. B. Tanner for helpful discussions. In particular, we thank K. Behnia for supplying us with unpublished data. This work has been supported by the Natural Science and Engineering Research Council of Canada and the Canadian Institute for Advanced Research. Work in Tallinn was supported by the Estonian Ministry of Education and Research under Grant SF0690029s09, and Estonian Science Foundation under Grants ETF8170 and ETF8703.

---

[1] J. Schoenes, C. Schönenberger, J. J. M. Franse, and A. A. Menovsky, Phys. Rev. B **35**, 5375 (1987).

[2] M. B. Maple, J. W. Chen, Y. Dalichaouch, T. Kohara, C. Rossel, M. S. Torikachvili, M. W. McElfresh, and J. D. Thompson, Phys. Rev. Lett. **56**, 185 (1986).

[3] T. T. M. Palstra, A. A. Menovsky, and J. A. Mydosh, Phys. Rev. B **33**, 6527 (1986).

[4] M. W. McElfresh, J. D. Thompson, J. O. Willis, M. B. Maple, T. Kohara, and M. S. Torikachvili, Phys. Rev. B **35**, 43 (1987).

[5] Z. Zhu, E. Hassinger, Z. Xu, D. Aoki, J. Flouquet, and K. Behnia, Phys. Rev. B **80**, 172501 (2009).

[6] A. R. Schmidt, M. H. Hamidian, P. Wahl, F. Meier, A. V. Balatsky, J. D. Garrett, T. J. Williams, G. M. Luke, and J. C. Davis, Nature (London) **465**, 570 (2010).

[7] U. Nagel, T. Uleksin, Toomas Rõõm, R. P. S. M. Lobo, P. Lejay, C. C. Homes, J. Hall, A. W. Kinross, S. Purdy, T. J. Williams, G. M. Luke, and T. Timusk, arXiv:1107.5574.

[8] T. T. M. Palstra, A. A. Menovsky, J. van den Berg, A. J. Dirkmaat, P. H. Kes, G. J. Nieuwenhuys, and J. A. Mydosh, Phys. Rev. Lett. **55**, 2727 (1985).

[9] T. D. Matsuda, E. Hassinger, D. Aoki, V. Taufour, G. Knebel, N. Tateiwa, E. Yamamoto, Y. Haga, Y. Ōnuki, Z. Fisk, and J. Flouquet, J. Phys. Soc. Jpn. **80**, 114710 (2011).

[10] N. Tateiwa, T. D. Matsuda, Y. Ōnuki, Y. Haga, and Z. Fisk, Phys. Rev. B **85**, 054516 (2012).

[11] W. Schlabitz, J. Baumann, B. Pollit, U. Rauchschwalbe, H. M. Mayer, U. Ahlheim, and C. D. Bredl, Z. Phys. B **62**, 171 (1986).

[12] C. Broholm, J. K. Kjems, W. J. L. Buyers, P. Matthews, T. T. M. Palstra, A. A. Menovsky, and J. A. Mydosh, Phys. Rev. Lett. **58**, 1467 (1987).

[13] A. Kiss and P. Fazekas, Phys. Rev. B **71**, 054415 (2005).

[14] P. Chandra, P. Coleman, J. A. Mydosh, and V. Tripathi, Nature (London) **417**, 6891 (2002).

[15] K. Haule and G. Kotliar, Nat. Phys. **5**, 796 (2009).

[16] F. Cricchio, F. Bultmark, O. Grånäs, and Lars Nordström, Phys. Rev. Lett. **103**, 107202 (2009).

[17] H. Harima, K. Miyake, and J. Flouquet, J. Phys. Soc. Jpn. **79**, 033705 (2010).

[18] D. A. Bonn, J. D. Garrett, and T. Timusk, Phys. Rev. Lett. **61**, 1305 (1988).

[19] L. Degiorgi, S. Thieme, H. R. Ott, M. Dressel, G. Grüner, Y. Dalichaouch, M. B. Maple, Z. Fisk, C. Geibel, and F. Steglich, Z. Phys. B **102**, 367 (1996).

[20] J. Levallois, F. Lévy-Bertrand, M. K. Tran, D. Stricker, J. A. Mydosh, Y.-K. Huang, and D. van der Marel, Phys. Rev. B **84**, 184420 (2011).

[21] C. C. Homes, M. A. Reedyk, D. A. Crandles, and T. Timusk, Appl. Opt. **32**, 2976 (1993).

[22] R. C. Dynes, V. Narayanamurti, and J. P. Garno, Phys. Rev. Lett. **41**, 1509 (1978).

[23] J. A. Mydosh and P. M. Oppeneer, Rev. Mod. Phys. **83**, 1301 (2011).

[24] A. F. Santander-Syro, M. Klein, F. L. Boariu, A. Nuber, P. Lejay, and F. Reinert, Nat. Phys. **5**, 637 (2009).

[25] P. Aynajian, E. H. da Silva Neto, C. V. Parker, Y.-K. Huang, A. Pasupathy, J. A. Mydosh, and A. Yazdani, Proc. Natl. Acad. Sci. USA, **107**, 10383 (2010).
[26] C. R. Wiebe, J. A. Janik, G. J. MacDougall, G. M. Luke, J. D. Garrett, H. D. Zhou, Y.-J. Jo, L. Balicas, Y. Qiu, J. R. D. Copley, Z. Yamani, and W. J. L. Buyers, Nat. Phys. **3**, 96 (2007).
[27] P. M. Oppeneer, S. Elgazzar, J. Rusz, Q. Feng, T. Durakiewicz, and J. A. Mydosh, Phys. Rev. B **84**, 241102(R) (2011).
[28] S. Elgazzar, J. Rusz, M. Amft, P. M. Oppeneer, and J. A. Mydosh, Nat. Mater. **8**, 337 (2009).
[29] P. M. Oppeneer, J. Rusz, S. Elgazzar, M.-T. Suzuki, T. Durakiewicz, and J. A. Mydosh, Phys. Rev. B **82**, 205103 (2010).
[30] R. Okazaki, T. Shibauchi, H. J. Shi, Y. Haga, T. D. Matsuda, E. Yamamoto, Y. Ōnuki, H. Ikeda, and Y. Matsuda, Science **331**, 439 (2011).
[31] E. Hassinger, G. Knebel, T. D. Matsuda, D. Aoki, V. Taufour, and J. Flouquet, Phys. Rev. Lett. **105**, 216409 (2010).

Chapter 7

The hybridization state and Fermi liquid scaling

This paper primarily deals with the behaviour of the charge carriers above the hidden order transition and the hybridization that leads to the heavy fermion state. The papers on STM and ARPES were quite recent when this was published so much of the focus was on the same ideas that had been put forward by them.

The main finding of the paper is that the scattering immediately above the transition temperature is Fermi-liquid-like. Typically, Fermi liquid behaviour is identified by a $\rho \propto T^2$ quadratic dependence of the resistivity on temperature. In $\mathrm{URu_2Si_2}$ the temperature range over which the scattering is Fermi liquid in nature is too narrow to identify the Fermi liquid behaviour this way. In this material, we identified a Fermi liquid purely optically, by the observation that $1/\tau \propto \omega^2$.

The scaling between the temperature and frequency terms is given by the self-energy, and is wholly determined by the number of particles participating in the scattering process. The coefficient that defines this scaling, called b in our paper, must be equal to 4 in a Fermi liquid with electron-electron scattering in which Umklapp processes are allowed. We find that this coefficient differs from it's theoretical value, indicating that Fermi liquid behaviour here is not caused by electron-electron scattering. Furthermore, none of the materials for which we could find data had a scaling factor equal to 4, indicating that this behaviour is generic to correlated electron systems.

We also studied the hybridization gap and the Drude weight. We found that the Drude weight is conserved below 12 meV, while the spectral weight above this frequency is associated with the formation of the hybridization gap and is shifted up to higher frequencies. The mass associated with the heavy carriers in the Drude peak is only about $5m_e$, much smaller than the specific heat mass enhancement of $40m_e$ but consistent with STM measurements. We were able to track the onset of the coherence and the development of the hybridization pseudogap in the density of states and its evolution with temperature.

For this study, I contributed to the optical experiments to determine the absolute reflectance, which were done concurrently in Paris and at McMaster. I measured the temperature dependence of the reflectance up to high temperatures across the full frequency range, from 3 meV up to 5 eV. I and another student, Alison Kinross, performed the DC resistivity measurements on the samples used in Tallinn and at McMaster. I analyzed the optical data including doing fits to the reflectance, calculating the conductivity and the scattering rate, and calculating the temperature dependence of the reflectivity. I assisted in writing and editing the paper itself which was written by Professor Timusk, including doing the final proof edits prior to publication.

Optical spectroscopy shows that the normal state of URu_2Si_2 is an anomalous Fermi liquid

Urmas Nagel[a], Taaniel Uleksin[a], Toomas Rõõm[a], Ricardo P. S. M. Lobo[b], Pascal Lejay[c], Christopher C. Homes[d], Jesse S. Hall[e], Alison W. Kinross[e], Sarah K. Purdy[e], Tim Munsie[e], Travis J. Williams[e], Graeme M. Luke[e,f], and Thomas Timusk[e,f,1]

[a]National Institute of Chemical Physics and Biophysics, 12618 Tallinn, Estonia; [b]Laboratoire de Physique et d'Étude des Matériaux, École Supérieure de Physique et de Chimie Industrielles de la Ville de Paris, ParisTech, Université Pierre et Marie Curie, Centre National de la Recherche Scientifique, 75005 Paris, France; [c]Institut Neél, Centre National de la Recherche Scientifique/Université Joseph Fourier, 38042 Grenoble Cedex 9, France; [d]Condensed Matter Physics and Materials Science Department, Brookhaven National Laboratory, Upton, NY 11780; [e]Department of Physics and Astronomy, McMaster University, Hamilton, ON, Canada L8S 4M1; and [f]Canadian Institute for Advanced Research, Toronto, ON, Canada M5G 1Z8

Edited* by J. C. Seamus Davis, Cornell University, Ithaca, NY, and approved October 2, 2012 (received for review May 16, 2012)

Fermi showed that, as a result of their quantum nature, electrons form a gas of particles whose temperature and density follow the so-called Fermi distribution. As shown by Landau, in a metal the electrons continue to act like free quantum mechanical particles with enhanced masses, despite their strong Coulomb interaction with each other and the positive background ions. This state of matter, the Landau–Fermi liquid, is recognized experimentally by an electrical resistivity that is proportional to the square of the absolute temperature plus a term proportional to the square of the frequency of the applied field. Calculations show that, if electron-electron scattering dominates the resistivity in a Landau–Fermi liquid, the ratio of the two terms, *b*, has the universal value of $b = 4$. We find that in the normal state of the heavy Fermion metal URu_2Si_2, instead of the Fermi liquid value of 4, the coefficient $b = 1 \pm 0.1$. This unexpected result implies that the electrons in this material are experiencing a unique scattering process. This scattering is intrinsic and we suggest that the uranium *f* electrons do not hybridize to form a coherent Fermi liquid but instead act like a dense array of elastic impurities, interacting incoherently with the charge carriers. This behavior is not restricted to URu_2Si_2. Fermi liquid-like states with $b \neq 4$ have been observed in a number of disparate systems, but the significance of this result has not been recognized.

hidden order | resistance | infrared conductivity | resonant scattering

Among the heavy Fermion metals, URu_2Si_2 is one of the most interesting: it displays, in succession, no fewer than four different behaviors. As is shown in Fig. 1, where the electrical resistivity is plotted as a function of temperature, at 300 K the material is a very bad metal in which the conduction electrons are incoherently scattered by localized uranium *f* electrons. Below $T_K \sim 75$ K, the resistivity drops and the material resembles a typical heavy Fermion metal (1–3). At $T_0 = 17.5$ K the "hidden-order" phase transition gaps a substantial portion of the Fermi surface but the nature of the order parameter is not known. A number of exotic models for the ordered state have been proposed (4–7), but there is no definitive experimental evidence to support them. Finally, at 1.5 K URu_2Si_2 becomes an unconventional superconductor. The electronic structure, as shown by both angle-resolved photoemission experiments (8) and band-structure calculations (9) is complicated, with several bands crossing the Fermi surface. To investigate the nature of the hidden-order state we focus on the normal state just above the transition. This approach has been used in the high-temperature superconductors where the normal state shows evidence of discrete frequency magnetic excitations that appear to play the role that phonons play in normal superconductors (10). The early optical experiments of Bonn et al. (11) showed that URu_2Si_2 at 20 K, above the hidden order transition, has an infrared spectrum consisting of a narrow Drude peak and a strong incoherent background. The large electronic specific heat just above the transition pointed to the presence of heavy carriers with a mass $m^* = 25m_e$ (2). However, recent scanning tunneling micrsocopy (STM) experiments contradict this model (12, 13). Schmidt et al. (12) find a light band crossing the Fermi surface above 17.5 K turning into a hybridized heavy band only below the hidden-order transition. This finding contradicts the conventional view that mass builds up gradually below T_K, although there have been recent reports of some hybridization occurring in the 25–30 K region by Park et al. (14) and Levallois et al. (15), but the reported effects are weak and perhaps not resolved by all spectroscopies. We can test the development of mass by carefully tracking the Drude weight as a function of temperature with optical spectroscopy. The Drude weight is a quantitative measure of the effective mass of the carriers. Before turning to an optical investigation of the normal state of URu_2Si_2, we will review briefly what is known from optical spectroscopy of other metallic systems at low temperature.

In pure metals, at high temperature the dominant source of resistance is the electron–phonon interaction, giving rise to the familiar linear temperature-dependence of the electrical resistance. At low temperature the phonon contribution weakens and the resistance varies as T^2, where T is the absolute temperature. Gurzhi showed that under rather general conditions, the resistivity of a pure metal at low temperature is given by $\rho(\omega, T) = A'[\hbar\omega^2 + 4\pi^2(k_B T^2)]$, where ω is the frequency of the field used to measure the resistivity, and A' a constant that varies from material to material (16). This formula is valid for three-dimensional systems, as long as Galilean invariance is broken by the lattice, and the Fermi surface is not convex and simply connected (16–22), and then in the high-frequency regime when $\omega >> 1/\tau^{sp}(\omega, T)$ with $1/\tau^{sp}(\omega, T)$ being the single-particle scattering rate. In the dc limit, the resistivity behaves as $\rho(T) = AT^2$, if umklapp scattering is allowed. Notice that although the coefficients A and A' contain different combinations of umklapp and normal scattering amplitudes, they are related as $A = 4\pi^2 A'$ if umklapp scattering dominates over the normal one. We prefer to introduce a parameter b, which we define as $b = A/(A'\pi^2)$. Then, if the Gurzhi resistivity formula is valid, $b = 4$. A source of confusion in the literature is the formula for the single-particle scattering rate $1/\tau^{sp}$ within Fermi liquid theory $1/\tau^{sp}(\omega, T) = A'[(\hbar\omega^2 + \pi^2(k_B T)^2]$ that is sometimes used to describe the resistivity. This formula does not apply here and, to be general, we will use the parameter b as a quantity that is measured by comparing the frequency and temperature terms in Gurzhi's

---

Author contributions: U.N., T.U., T.R., R.P.S.M.L., C.C.H., J.S.H., A.W.K., S.K.P., T.M., G.M.L., and T.T. performed research; P.L., T.J.W., and G.M.L. contributed new reagents/analytic tools; A.W.K. and T.M. analyzed data; and T.T. wrote the paper.

The authors declare no conflict of interest.

*This Direct Submission article had a prearranged editor.

[1]To whom correspondence should be addressed. E-mail: timusk@mcmaster.ca.

www.pnas.org/cgi/doi/10.1073/pnas.1208249109

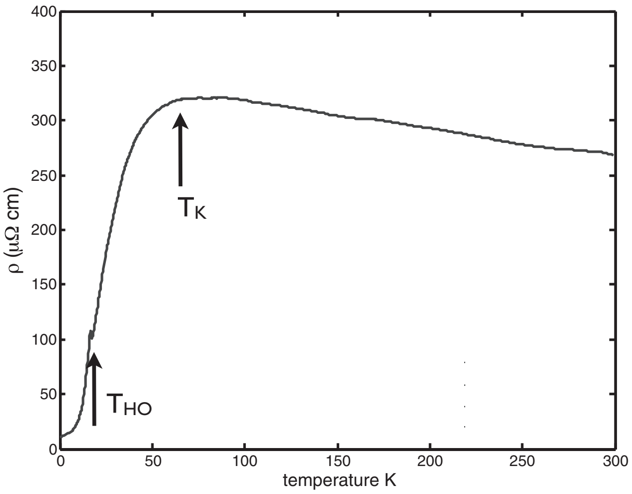

Fig. 1. The dc resistivity of URu_2Si_2 as a function of temperature. Unlike ordinary metals, the resistivity rises as the temperature is lowered below 300 K to reach a maximum at around 75 K, referred to as the Kondo temperature, T_K. Below this temperature the resistivity drops dramatically and the system acquires a Drude peak at low frequency, a defining property of a material with metallic conductivity. This change of resistivity slope at T_K is the signature of a heavy Fermion system, where the conduction electrons hybridize with *f* electrons to form massive carriers. In URu_2Si_2, this process in interrupted at 17.5 K by a phase transition, called the hidden-order transition, where a portion of the Fermi surface is gapped. Our aim in this work is to investigate the electrodynamics of this system just above the hidden-order state.

formula, in the same energy range $\hbar\omega \sim k_BT$. Although the focus of this report is an accurate determination of b in the normal state above the hidden-order transition of URu_2Si_2, it is useful to look at previous work, where the quantity b can be extracted from the measured optical resistivity $\rho(\omega, T)$ and, in some cases, the dc resistivity $\rho(T)$. These are challenging experiments because Fermi liquid scattering, in most metals, is a low-temperature phenomenon and, therefore, to stay in the energy range where the temperature dependence of the resistivity is examined, the optical measurements have to be carried out in the very far infrared, an experimentally difficult region. Nevertheless, a search of the literature turns up several examples.

The first report of a discrepancy of the ratio of the amplitudes of the frequency and temperature terms in a Fermi liquid was a report by Sulewski et al. (23) on the infrared properties of the heavy Fermion material UPt_3. Instead of the expected value of $b = 4$, they reported and experimental upper limit of $b = 1$. Since then a number of studies have presented both T^2 and ω^2 dependencies of the optical scattering on the same material (24–26). A summary of these is given in Table 1. In some cases, the authors have not calculated the ratio A/A', in which case we have made an estimate from the published curves. We have also tabulated the approximate maximum temperatures and frequencies where the quadratic dependence is observed. It is important that these overlap to some extent. The overall conclusion one can draw from this table is that in no case has the expected canonical Fermi liquid behavior with $b = 4$ been observed experimentally. Additional examples of non-Fermi liquid behavior are given in a review by Dressel (27).

Table 1. Summary of experimental measurements of the ratio *b* of temperature and frequency terms for some Fermi liquids

Material	T_{max} (meV)	ω_{max} (meV)	b	Source
UPt_3	1	1	<1	(23)
$CePd_3$			1.3	(23)
$Ce_{0.95}Ca_{0.05}TiO_{3.04}$	25	100	1.72	(24)
Cr	28	370	2.5	(25)
$Nd_{0.95}TiO_4$	24	50	1.1	(26)
URu_2Si_2	2	10	1.0	Present work

T_{max} and ω_{max} indicate the upper limit of the measured quadratic behavior of $\rho(T)$ and $\rho(\omega)$, respectively.

Results

Fig. 2 shows the optical conductivity between 20 and 75 K, the region where coherence develops, as shown by the appearance of a Drude peak below 15 meV, which narrows as the temperature is lowered. Above 75 K the optical conductivity is frequency- and temperature-independent. Interestingly, we find that in the temperature range 75 K to 20 K the area under the Drude peak is temperature-independent, with a plasma frequency of ~400 meV. This finding is a signature that m^* is constant in this region of temperatures. A distinct minimum develops between the Drude peak and the high-frequency saturation value. We suggest this minimum is a pseudohybridization gap normally associated with the formation of the Kondo lattice but not fully formed in this material above 17.5 K. There is a simple relationship between the Kondo temperature T_K, the effective mass m^* and the gap V_K: $m^*/m_e = (V_K/k_BT_K)^2$ (17, 28). Estimating $T_K = 75$ K from the temperature where the Drude peak first appears, and taking $V_K = 15 \pm 5$ meV, we find $m^*/m_e = 5 \pm 2$, which is lower than what is estimated from specific heat measurements (2) but not in disagreement with recent STM (12) or optical (15) data. We note here that the hybridization gap acts like the pseudogap in the cuprates; its frequency does not change with temperature but fills in gradually as the temperature is raised. In addition, the spectral weight lost in the gap region is not recovered by the Drude peak or in the spectral region immediately above the gap. The inset in Fig. 2 shows the accumulated spectral weight at the five temperatures. All of the curves cross at 15 meV, showing that the Drude weight is conserved in the temperature range from 20 to 75 K. On the other hand, spectral weight is lost above this frequency range as the temperature is lowered. These behaviors are inconsistent with a simple picture of an effective mass resulting from an inelastic interaction with a bosonic spectrum.

To examine quasiparticle damping above the hidden-order transition, we apply an extended Drude model to the conductivity:

$$\sigma(T,\omega) = \frac{\omega_p^2}{4\pi}\frac{1}{1/\tau^{op}(\omega) - i\omega(1+\lambda(\omega))}, \qquad [1]$$

where $\omega_p^2 = 4\pi ne^2/m_e$ is the plasma frequency squared, $1/\tau^{op}(\omega) = \frac{\omega_p^2}{4\pi}\mathcal{R}e(1/\sigma(\omega))$, the optical scattering rate, and $1 + \lambda(\omega) = m^*/m_e$ is the mass enhancement. Optical phonons at 13.5 and 46.9 meV have been subtracted from the measured conductivity. The renormalized optical scattering rate, $1/\tau^* = 1/\tau^{op}/(m^*/m_e)$, is shown in Fig. 3*A*, where we have used a plasma frequency of $\omega_p^* = \omega_p/\sqrt{m^*/m_e} = 418$ meV, evaluated from the Drude weight. As the temperature exceeds T_K, here taken as 75 K, the frequency-dependence below 14 meV is replaced by uniform temperature- and frequency-independent scattering. We also note that the low-frequency scattering above 20 K is incoherent in the sense that $1/\tau^* > \omega$ but, significantly, the condition reverses at 20 K, near the temperature of the hidden order transition.

We next turn to the optical resistivity, defined as $\rho(\omega) = \mathcal{R}e[1/\sigma(\omega)]$, where $\sigma(\omega)$ is the complex conductivity. We used the "refined reflectivity" (*Materials and Methods*) to calculate this quantity, as plotted in Fig. 3*B* at three temperatures, because we are focusing on temperatures just above the phase transition. The zero frequency limit of $\rho(\omega)$ is the dc resistivity, which as mentioned above, has been adjusted to agree with the measured

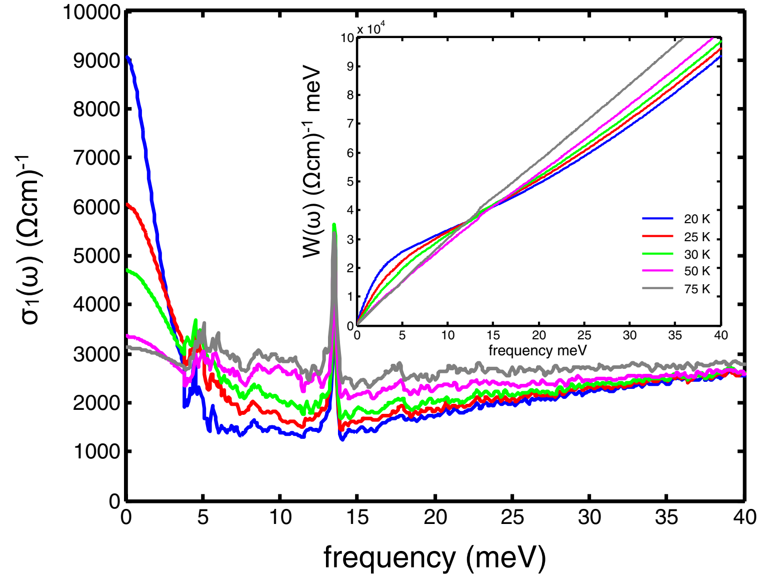

Fig. 2. The optical conductivity as a function of photon energy in the heavy Fermion state. Below 4 meV, the conductivity has been fitted to a Drude peak, the amplitude of which agrees with the dc resistivity. (*Inset*) The integrated spectral weight up to a frequency ω. Below 10 meV, the Drude weight dominates. The total Drude weight is temperature independent because all of the curves join at 15 meV above the Drude cutoff. The spectral weight in the hybridization gap region, 5–40 meV, is lost to higher frequencies, and the accumulated spectral weight drops at 40 meV as the temperature is lowered.

resistivity shown as filled circles at zero frequency. Fig. 3*B* also shows a parabola fitted to the data where the constants $A'(T)$ and $c(T)$ are adjustable parameters.

We next evaluate the Fermi liquid parameters A' and A from our data, as well as the constant b. We determine A' directly from a quadratic fit to the optical data shown in Fig. 3*B* between 5 and 11 meV. Note that the the scattering rate deviates from the simple quadratic form below 5 meV and above 12 meV, where it saturates. The coefficient $A' = 0.034$ $\mu\Omega\cdot\text{cm}\cdot\text{K}^{-2}$ at 17.5 K and decreases to 0.030 $\mu\Omega\cdot\text{cm}\cdot\text{K}^{-2}$ at 22 K, whereas the cutoff seems to remain at 12 meV. Even with our enhanced signal-to-noise ratio, we see little evidence to coupling to sharp resonance modes in our spectra of the type seen in the cuprates (29). Such modes, whether they are magnetic or because of phonons, would show a characteristic rise of scattering rate at the mode frequency. Instead, the self energy of the quasiparticles is dominated by a featureless continuum without an energy scale.

The inset to Fig. 3*B* shows the intercept $c(T)$ plotted as a function of T^2. The slope gives us the coefficient $A = b(\pi)^2 A' = 0.30$ $\mu\Omega\cdot\text{cm}\cdot\text{K}^{-2}$ and $b = 1.0 \pm 0.1$, an average over the temperature region 18.5 K to 22 K. The intercept is negative but in view of large range of extrapolation, we do not consider this significant. A positive intercept would suggest a linear T contribution, whereas a negative one implies a Kondo-like process that rises as the temperature is lowered. Although the scatter in the points precludes any definite conclusions, it is clear from the raw data that an upward trend is present in $\rho(\omega)$ below 3 meV and below 25 K.

We next compare these optically determined parameters with the parameters determined from the dc resistivity. Fig. 4 shows the temperature derivative of the dc resistivity of URu_2Si_2. The line is a straight-line fit to the derivative in the 18–22 K temperature range to $d\rho/dT = c + 2AT$ with $A = 0.3 \pm 0.12$ $\mu\Omega\cdot\text{cm}\cdot\text{K}^2$. The fit shows that the resistivity is dominated by a T^2 term and the coefficient A agrees with its value determined from optics well within experimental error. The near-zero value of the intercept c shows that there is only a weak linear in T contribution to the scattering, but it should be noted that in view of the narrow 4 K temperature range used in the fit, by itself Fig. 3 does not prove that we have a Fermi liquid above 18 K. In fact, higher-resolution dc resistivity data (30) shows that there is no finite region where $\rho(T)$ is linear in T. If Fermi statistics and electron-electron scattering dominate the resistivity and $1/\tau < \omega$, we expect that, in addition to the ω^2 dependence of the ac and T^2 dependence of the dc resistivity, the coefficient b has to equal 4. In URu_2Si_2 all of the conditions are met except the last one. Our strongest evidence for this are the frequency fits in Fig. 3*B* and the main role of the dc resistivity fit is to confirm the value of the coefficient A. The agreement of the A coefficients obtained by optics and transport is better than expected because the experiments were done on different samples from the same batch and absolute dc resistivities generally do not agree to better than 20% among groups. A Fermi liquid–like resistivity above 17.5 K in URu_2Si_2 with $A = 0.35$ has also been reported by Palstra et al. (3). Another comparison between the temperature- and frequency-dependence of scattering is the ratio of the Kondo temperature $T_K = 75$ K and the cutoff frequency $\omega_c = 14$ meV of frequency-dependent scattering. If it is written as $b_c = \omega_c^2/\pi^2 T_K^2$ we find that $b_c = 0.48$, again substantially smaller than the Fermi liquid value of $b = 4$.

We conclude that instead of the expected value of $b = 4$ for Fermi liquid scattering (16), our data clearly show that $b = 1 \pm 0.1$ in the temperature region immediately above the hidden order transition. This discrepancy is well outside our possible error. The value $b = 1$ is expected for resonant elastic scattering from impurities, when the single-particle scattering rate has an ω^2 but no T^2 term (20). The Kubo formula then yields the optical $1/\tau$ with $b = 1$. Here, however, the scattering appears to be intrinsic. One possibility is that in this material, instead of the formation of an Anderson lattice of coherent states, the uranium f levels act like independent incoherent scatterers and form the coherent lattice only below the hidden-order transition. This picture has also been advanced by Haule and Kotliar (6) and Schmidt et al. (12). Our data provide independent evidence for this model. The important question remains: Are there cases of true Fermi liquids with $b = 4$? As Table 1 shows, all of the cases where the frequency-dependence has been measured fail to show clear cases where $b = 4$. The deviation from the Fermi liquid value of b has been discussed by Rosch and Howell (18) for some special cases,

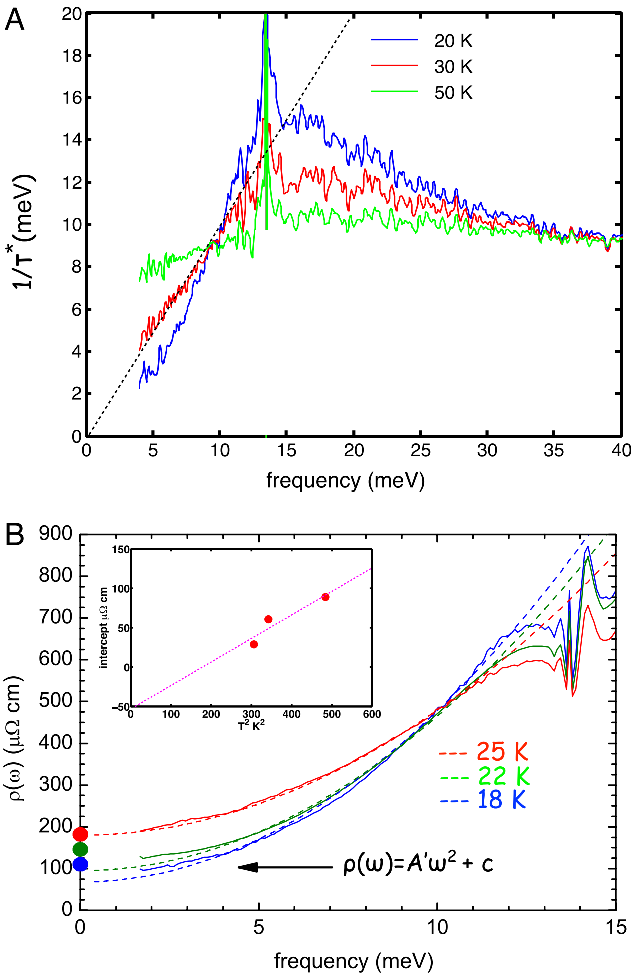

Fig. 3. (*A*) The frequency dependent scattering rate $1/\tau^*$ at three temperatures in the normal state above the hidden-order transition at 17.5 K from the unrefined reflectivity. As the temperature is raised, the Fermi liquid scattering below 14 meV is replaced by a uniform frequency-independent incoherent scattering. Coherent quasiparticles exist below the dashed line $\omega > 1/\tau^*$. (*B*) The optical resistivity $\rho(\omega)$ vs. photon energy at low frequencies from the refined reflectivity. The experimental curves (solid lines) are compared with a Fermi liquid fit (dashed lines), with the coefficient A' and an offset $c(T)$ determined by a least-squares fit to the experimental data. (*Inset*) The temperature dependence of $c(T)$ plotted as a function of T^2, for the three lowest temperatures, 17.5 K, 18 K, and 22 K. The slope of this curve yields an estimate of $A = 0.30\mu\Omega\cdot\text{cm}\cdot\text{K}^{-2}$ from optics.

such as quasi-two-dimensional compounds, and a case with $b = 5.6$ is reported by Dressel (27).

In summary, we have found that in the normal state above the hidden-order transition in URu$_2$Si$_2$, a relatively light band with a mass $m^*/m_e \sim 5$ is weakly coupled to the f electrons with $V_K \sim 5$ meV, and that this band is responsible for the transport current as measured by the optical conductivity. We suggest that this coupling is not strong enough to form an Anderson lattice. Instead, the f electrons act like elastic, incoherent scatterers, as shown by the anomalous $b = 1$ in the generalized Fermi liquid-scattering formula instead of the expected $b = 4$ for coherent inelastic scattering from bosonic excitations. As suggested by the STM experiments of Schmidt et al. (12), the Fermi liquid with the heavy quasiparticles exists only below the hidden-order transition. Because of the rapidly varying electronic density of states, we are unable to use our technique to analyze the nature of the scattering below the hidden-order transition to verify this scenario, and recent transport experiments suggest a possible non-Fermi liquid behavior at low temperatures (30). We also note that this anomalous Fermi liquid behavior is shared by a number of other strongly correlated materials, where magnetism appears to play a role. The possibility exists that in these systems the electron lifetime is not determined by Fermi liquid electron-electron scattering but by elastic resonant scattering, and leads to the notion that a quadratic temperature dependence of the resistivity may not be a good signature of a Fermi liquid.

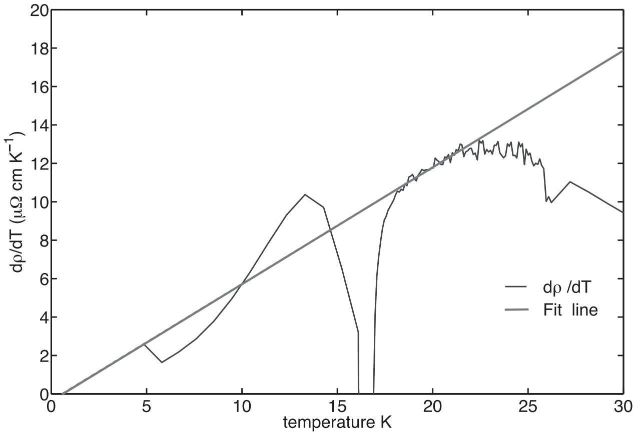

Fig. 4. The solid line shows the temperature derivative of the experimental dc resistivity of URu$_2$Si$_2$. The straight line is a fit of $d\rho(T)/dT = c + 2AT$ in the temperature range 18–22 K. Above 22 K the temperature derivative falls, a signature of the onset of incoherence.

Materials and Methods

The single crystals of URu$_2$Si$_2$ were grown at Grenoble and at McMaster in triarc furnaces in an argon atmosphere. The crystals were annealed under UHV at 900 °C for 10 d. The surfaces cleaved along the ab plane were measured by standard reflectance techniques, at three separate laboratories, using an in situ gold-overcoating technique (31). The absolute reflectance results of the three groups agreed to within 0.5%.

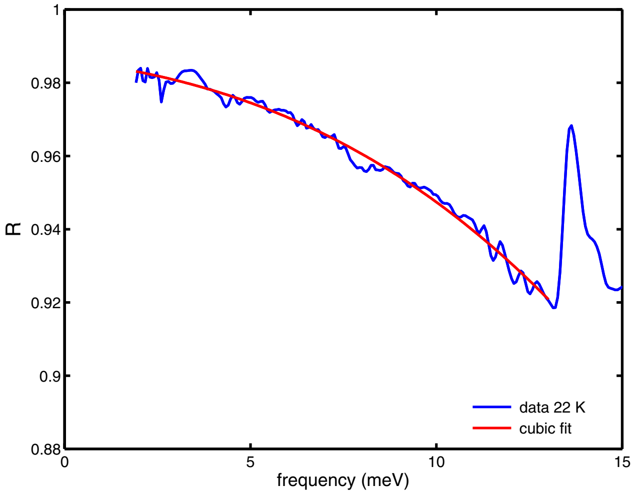

Fig. 5. The noisy experimental reflectance data, measured at 22 K, is smoothed by fitting a cubic polynomial to the data. This curve is combined with other experimental data at higher frequencies and Kramers–Kronig transformed to yield an approximation to the actual spectrum.

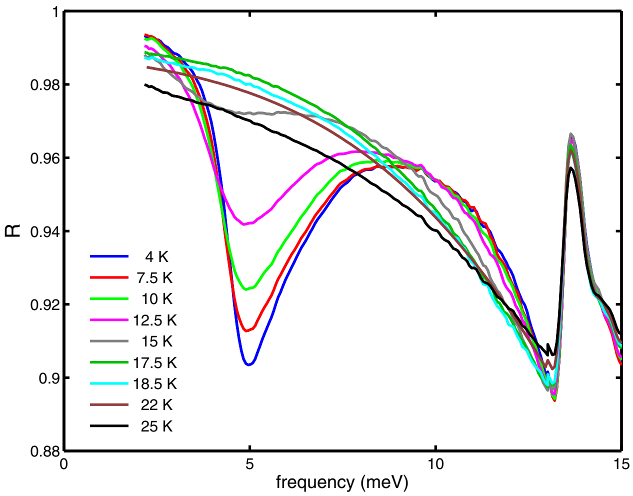

Fig. 6. “Refined” reflectance of URu_2Si_2 obtained by first measuring a series of spectra at different temperatures T and then dividing the spectra with one measured at a reference temperature T_{ref}. All this is done without moving the sample stage. The resulting temperature ratios are smooth without interference artifacts. Then, these smooth ratios are multiplied by the estimate to the absolute spectrum at T_{ref} shown in Fig. 4. The resulting spectra shown in the figure are a low noise approximation to the true absolute spectra of URu_2Si_2. Of all of the spectra shown, only the one at T_{ref} = 22 K is a polynomial fit; all of the others show actual measured data.

At long wavelengths, a simple procedure which we call “refined thermal reflectance” was used to cancel out interference artifacts (32) below 13 meV. The procedure involves the following steps. We have found that the interference artifacts seen in the absolute experimental spectrum (Fig. 5) are related to the movement of the sample stage. To overcome this problem, we measure the reflected spectra over a narrow temperature range without moving the sample stage, typically from 4 K to 25 K. Using one of the spectra as a reference, we record the ratios of the spectra at the various temperatures to the spectrum at the reference temperature. To obtain a low-noise absolute reflectance, we use the gold-overcoating technique to get an estimate of the absolute reflectance at the reference temperature. Because the sample is moved in this process this absolute spectrum is contaminated by interference artifacts. To eliminate these artifacts, we fit the absolute reflectance at the reference temperature with a cubic polynomial, a curve labeled “cubic fit” in Fig. 5. This smoothed spectrum is then used as a reference spectrum to calculate absolute spectra at all other temperatures. It is clear that the smoothing procedure hides any sharp structure in the reference spectrum. However, any new sharp structure that appears as the temperature is changed will be present at full resolution. The final refined spectra are shown in Fig. 6. This procedure is well-suited to the discovery of new spectral features that appear at phase transitions, for example the prominent minimum at 5 meV, because of the hidden-order gap. The measured refined reflectance was converted to an optical conductivity by Kramers–Kronig analysis. At low frequency, below 4 meV, a Drude response was assumed where we used the measured dc resistivity to determine the amplitude of the Drude peak and the absorption at our lowest measured infrared frequency to determine the width. At high frequency, beyond 7 eV, we used the results of Degiorgi et al. (33).

ACKNOWLEDGMENTS. We thank K. Behnia and T. Matsuda for supplying us with unpublished data. This work was supported by the Natural Science and Engineering Research Council of Canada and the Canadian Institute for Advanced Research. Work in Tallinn was supported by the Estonian Ministry of Education and Research under Grant SF0690029s09 and the Estonian Science Foundation under Grants ETF8170 and ETF8703; work in Paris was supported by the Agence Nationale de la Recherche under Grant BLAN07-1-183876 GAPSUPRA.

1. Palstra TTM, et al. (1985) Superconducting and magnetic transitions in the heavy-fermion system URu_2Si_2. *Phys Rev Lett* 55(24):2727–2730.
2. Maple MB, et al. (1986) Partially gapped Fermi surface in the heavy-electron superconductor URu2Si2. *Phys Rev Lett* 56(2):185–188.
3. Palstra TTM, Menovsky AA, Mydosh JA (1986) Anisotropic electrical resistivity of the magnetic heavy-Fermion superconductor URu_2Si_2. *Phys Rev B Condens Matter* 33(9):6527–6530.
4. Chandra P, Coleman P, Mydosh JA, Tripathi V (2002) Hidden orbital order in the heavy Fermion metal $URu_{(2)}Si_{(2)}$. *Nature* 417(6891):831–834.
5. Varma CM, Zhu L (2006) Helicity order: Hidden order parameter in URu_2Si_2. *Phys Rev Lett* 96(3):036405.
6. Haule K, Kotliar G (2009) Arrested Kondo effect and hidden order in URu_2Si_2. *Nat Phys* 5:796–799.
7. Balatsky AV et al. (2009) Incommensurate spin resonance in URu2Si2. *Phys Res B* 79(21):214413.
8. Santander-Syro AF, et al. (2009) Fermi-surface instability at the hidden-order transition of URu_2Si_2. *Nat Phys* 5:637.
9. Oppeneer PM, et al. (2010) Electronic structure theory of the hidden-order material URu_2Si_2. *Phys Rev B* 82:205103.
10. Carbotte JP, Timusk T, Hwang J (2011) Bosons in high-temperature superconductors: An experimental survey. *Rep Prog Phys* 74:066501.
11. Bonn DA, Garrett JD, Timusk T (1988) Far-infrared properties of URu_2Si_2. *Phys Rev Lett* 61(11):1305–1308.
12. Schmidt AR, et al. (2010) Imaging the Fano lattice to ‘hidden order’ transition in $URu_{(2)}Si_{(2)}$. *Nature* 465(7298):570–576.
13. Aynajian P, et al. (2010) Visualizing the formation of the Kondo lattice and the hidden order in $URu_{(2)}Si_{(2)}$. *Proc Natl Acad Sci USA* 107(23):10383–10388.
14. Park WK, et al. (2012) Observation of the hybridization gap and fano resonance in the Kondo lattice URu_2Si_2. *Phys Rev Lett* 108(24):246403.
15. Levallois J, et al. (2011) Hybridization gap and anisotropic far-infrared optical conductivity of URu_2Si_2. *Phys Rev B* 84:184420.
16. Gurzhi RN (1959) Mutual electron correlations in metal optics. *Sov Phys JETP* 35:673–675.
17. Millis AJ, Lee PA (1987) Large-orbital-degeneracy expansion for the lattice Anderson model. *Phys Rev B Condens Matter* 35(7):3394–3414.
18. Rosch A, Howell PC (2005) Zero-temperature optical conductivity of ultraclean Fermi liquids and superconductors. *Phys Rev B* 72:104510.
19. Jacko AC, Fjærestad JO, Powell BJ (2009) Unified explanation of the Kadowaki-Woods ratio in strongly correlated metals. *Nat Phys* 5:422–425.
20. Maslov DL, Chubukov AV (2012) First-Matsubara-frequency rule in a Fermi liquid. II. Optical conductivity and comparison to experiment. *Phys Rev B* 86:155137.
21. Maslov DL, Yudson VI, Chubukov AV (2011) Resistivity of a non-Galilean-invariant Fermi liquid near Pomeranchuk quantum criticality. *Phys Rev Lett* 106(10):106403.
22. Pal HK, Yudson VI, Maslov DL (2011) Resistivity of non-Galilean-invariant Fermi- and non-Fermi liquids. *Phys Rev Lett* 106(10):106403.
23. Sulewski PE, et al. (1988) Far-infrared absorptivity of UPt_3. *Phys Rev* 38(8):5338–5352.
24. Katsufuji T, Tokura Y (1999) Frequency and temperature dependence of conductivity for perovskite titanates. *Phys Rev B* 60:7673–7676.
25. Basov DN, Singley EJ, Dordevic SV (2002) Sum rules and electrodynamics of high-T_c cuprates in the pseudogap state. *Phys Rev B* 65:054516.
26. Yang J, Hwang J, Timusk T, Sefat AS, Greedan JE (2006) Temperature-dependent optical spectroscopy studies of $Nd_{1-x}TiO_3$. *Phys Rev B* 73:195125.
27. Dressel M (2011) Quantum criticality in organic conductors? Fermi liquid versus non-Fermi-liquid behaviour. *J Phys Condens Matter* 23(29):293201.
28. Dordevic SV, Basov DN, Dilley NR, Bauer ED, Maple MB (2001) Hybridization gap in heavy fermion compounds. *Phys Rev Lett* 86(4):684–687.
29. Hwang J, Timusk T, Schachinger E, Carbotte JP (2007) Evolution of the bosonic spectral density of the high-temperature superconductor $Bi_2Sr_2CaCu_2O_{8+\delta}$. *Phys Rev B* 75:144508.
30. Matsuda TD, et al. (2012) Details of sample dependence and transport properties of URu_2Si_2. *J Phys Soc Jpn* 80:114710.
31. Homes CC, Reedyk MA, Cradles DA, Timusk T (1993) Technique for measuring the reflectance of irregular, submillimeter-sized samples. *Appl Opt* 32(16):2976–2983.
32. Purdy S (2010) Optical spectroscopy of URu_2Si_2: A search for new features. MS thesis (McMaster University, Hamilton, ON, Canada).
33. Degiorgi L, et al. (1997) The electrodynamic response of heavy-electron materials with magnetic phase transitions. *Z Phys B* 102:367.

Chapter 8

The antiferromagnetic state

In this paper we present results on crystals of $URu_{2-x}(Fe, Os)_xSi_2$. The parent compound URu_2Si_2undergoes a first-order phase transition under pressure to an antiferromagnetic state. The relationship between the two states is the topic of intense discussion and debate, in particular because DMFT calculations for the AFM phase closely match the Fermi surface seen by ARPES and quantum oscillation measurements show the similarity of the two Fermi surfaces. This suggests that the Fermi surfaces of the two phases are very similar, despite the different orders underlying them.

The paper shows that the structure of the electronic gap does not change between the hidden order state and the antiferromagnetic state. The implication of this is that the same mechanism is responsible for gapping the Fermi surface in both states. The structure of the gap strongly resembles that of a spin density wave, and coupled with neutron scattering measurements and DMFT calculations the implication is that Fermi surface nesting is responsible for the charge gap. The absence of a spin density wave in the parent compound becomes all the more puzzling.

At the same time, the temperature dependence of the gap changes between the two states, with $2\Delta = Ak_BT_o$ giving different values for the coefficient A between the two states. There is clearly something to differentiate them, besides the absence of a magnetic ordered moment in the HO state, but the mechanism gapping the Fermi surface appears not to be the distinction. The energy gap does track the transition temperature quite closely.

We also show that there is unequivocally a Fermi liquid precursor to the transition, and that this is the case for both hidden order and antiferromagnetic transitions. As the transition temperature increases with increasing substitution, the temperature at which the optical scattering rate becomes linear moves upwards in temperature. The Fermi liquid scattering is anomalous, in that the coefficient relating the frequency and temperature dependences does not have the value expected for electron-electron scattering. Another mechanism is responsible for the scattering, and is presumably related to the ordered state due to the observation that the onset of this scattering occurs at a higher temperature as the transition temperature rises.

This work raises two questions that any explanation of the hidden order must address. The first is Why does Fermi surface nesting gap the Fermi surface but not form a spin density wave? The second is Why is the scattering always Fermi-liquid-like at temperatures above the transition and what is the mechanism responsible for this scattering?

In this study, I organized the experiments, communicating with other groups to arrange samples. I planned the experiments in detail. I carried out all of the measurements except the measurements of the dc resistivity, which were performed by another student in the group. I analyzed the data, including fitting the gap, calculating the conductivity and scattering rates, and fitting the Drude formula. I also wrote the paper. Additional analysis and editing was done by Professor Timusk. The other co-authors grew the crystals and supplied characterization data such as magnetization, transition temperatures, and so on that were used to inform the data analysis.

Electrodynamics of the antiferromagnetic phase in URu_2Si_2

Jesse S. Hall,[1] M. Rahimi Movassagh,[1] M. N. Wilson,[1] G. M. Luke,[1, 2] N. Kanchanavatee,[3, 4] K. Huang,[3, 5, *] M. Janoschek,[3, 4, †] M. B. Maple,[3, 4, 5] and T. Timusk[1, 2]

[1]*Department of Physics and Astronomy, McMaster University, Hamilton, ON, Canada L8S 4M1*
[2]*Canadian Institute for Advanced Research, Toronto, ON, Canada M5G 1Z8*
[3]*Department of Physics, University of California, San Diego, La Jolla, California 92093, USA*
[4]*Center for Advanced Nanoscience, University of California, San Diego, La Jolla, California 92093, USA*
[5]*Materials Science and Engineering Program, University of California, San Diego, La Jolla, California 92093, USA*

(Dated: July 24, 2015)

We present data on the optical conductivity of $URu_{2-x}(Fe,Os)_xSi_2$. While the parent material URu_2Si_2 enters the enigmatic hidden order phase below 17.5 K, an antiferromagnetic phase is induced by the substitution of Fe or Os onto the Ru sites. We find that both the HO and the AFM phases exhibit an identical gap structure that is characterized by a loss of conductivity below the gap energy with spectral weight transferred to a narrow frequency region just above the gap, the typical optical signature of a density wave. The AFM phase is marked by strong increases in both transition temperature and the energy of the gap associated with the transition. In the normal phase just above the transition the optical scattering rate varies as ω^2. We find that in both the HO and the AFM phases, our data are consistent with elastic resonant scattering of a Fermi liquid. This indicates that the appearance of a coherent state is a necessary condition for either ordered phase to emerge. Our measurements favor models in which the HO and the AFM phases are driven by the common physics of a nesting-induced density-wave-gap.

The heavy fermion metal URu_2Si_2 has a rich phase diagram in both temperature and pressure [1–3]. Uniquely among heavy fermion materials, as the temperature is lowered, the development of the heavy fermion phase is interrupted by a second order phase transition at 17.5 K [4, 5] to an enigmatic “hidden order” (HO) whose physical origin has been the subject of considerable study. Despite intense experimental investigation [6–10] and proposed theoretical models [11–15], the nature of the phase transition has remained elusive.

When hydrostatic pressure is applied to URu_2Si_2 the temperature of the transition rises steadily with pressure up to 20 K at 1.5 GPa, [16] at which point a first order phase transition from the HO phase with a small extrinsic magnetic moment [3, 17] to a large moment long-range antiferromagnetic (AFM) phase [1, 18, 19] occurs. As the pressure is further increased the transition temperature continues to rise up to nearly 30 K [20]. Much attention has been placed upon the antiferromagnetic phase because quantum oscillation measurements [10, 21] suggest that the Fermi surface does not change between the HO and AFM phases. This allows calculations of the bandstructure [22, 23] and the Fermi surface, which can be computed for the AFM phase, to be applied to the HO phase.

Recently [24–26], it has been found that the partial substitution of Fe onto the Ru sites in URu_2Si_2 can also induce antiferromagnetism in the system. Increasing the concentration of Fe increases the transition temperature and, as with applied hydrostatic pressure, there is a crossover into antiferromagnetism above a certain substitution level. The similarity of the phase diagrams with pressure and Fe substitution suggests that the AFM phases are equivalent. Substitution with Os also induces an AFM phase that raises the transition temperature [26, 27]. In this paper, we present optical conductivity data on URu_2Si_2 in the substitution-induced antiferromagnetic phase and we report the first observations of the behavior of the energy gap for charge excitations in the AFM phase and its evolution with increasing substitution x. We also show spectra of the normal paramagnetic phase at temperatures above the AFM transition and contrast them with the spectra above the HO transition.

The Fe substituted crystals were grown in a tetra-arc furnace in San Diego and the Os substituted samples in a tri-arc furnace at McMaster, both using the Czochralski method in an argon atmosphere. Magnetic transitions were characterized using a SQUID magnetometer and the presence of an ordered antiferromagnetic moment was confirmed separately using muon spin rotation [26] and neutron scattering [25]. DC resistivity measurements were performed in an Oxford Maglab system using a four-probe geometry; the estimated error due to sample configuration and geometry is 20%, which is consistent with the variation in measurements in the literature [4, 28]. Optical measurements were performed using an SPS 200 Martin-Puplett Fourier-transform interferometer for reflectance measurements below 20 meV and a Bruker IFS 66v/s FTIR spectrometer for measurements from 15 meV to 4.5 eV. Absolute reflectance was measured using a standard gold evaporation technique [29], and the optical conductivity was obtained by performing a Kramers-Kronig analysis on the absolute reflectance data.

Figure 1 shows the absolute reflectance of

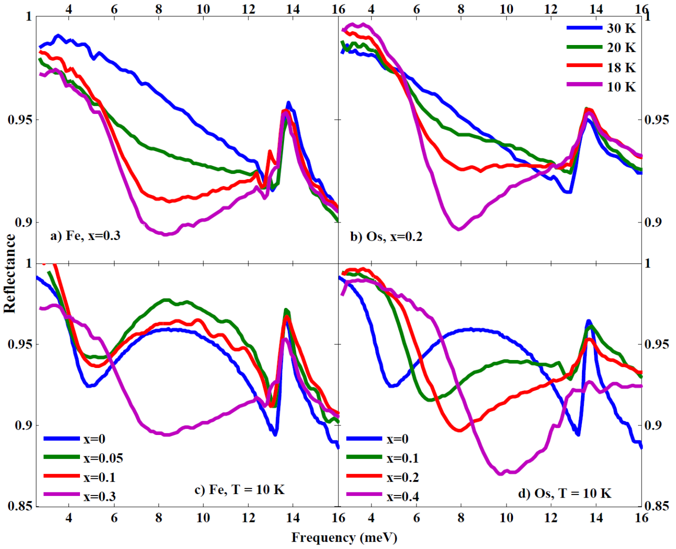

FIG. 1. Temperature and substitution dependence of the reflectance of samples of $URu_{2-x}(Fe,Os)_xSi_2$. The top panels shows the absolute reflectance for a) Fe, b) Os substitution, both in the AFM phase as a function of temperature. The bottom panels show the absolute reflectance as a function of x for c) Fe and d) Os substitution. The prominent depression of reflectance that develops in the 5 to 10 meV region in all the samples is a signature of a gap in the density of phases. Adding Fe and Os causes the reflectance minimum to move to higher frequency but the signature of the gap, a single minimum of reflectance, does not change with substitution.

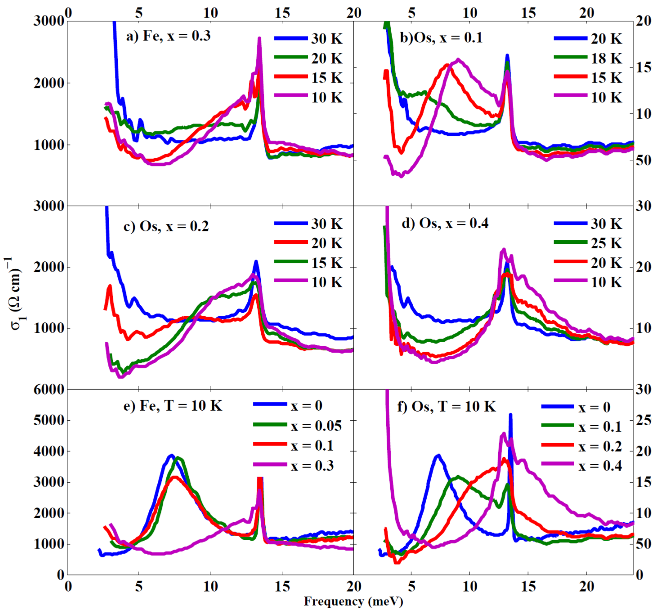

FIG. 2. Optical conductivity of $URu_{2-x}(Fe,Os)_xSi_2$ in the antiferromagnetic phase. Panels a) to d) show the optical conductivity changes with temperature for: a) Fe x=0.3, b) Os x=0.1, c) Os x=0.2, and d) Os x=0.4. Panel e) shows the dependence of the conductivity on the concentration for Fe substitution, with the parent material shown for comparison; panel f) shows the same for Os substitution. The parent compound conductivities have been reduced by a factor of 0.5 to allow easier comparison. The sharp peak at 13.6 meV is an optical phonon.

$URu_{2-x}(Fe,Os)_xSi_2$ in the AFM phase (panels a and b) and at different concentrations x for Fe substitution (panel c) and for Os (panel d). The parent compound with $x = 0$, which is in the HO phase, is shown as well. In all the curves a single strong minimum develops as the temperature is lowered below the transition. As x is increased the reflectance minimum moves to higher frequencies.

The characteristic absorption that signifies the opening of the HO gap in the parent compound is still present in the AFM phase, remarkably unchanged except for a shift to higher energies. There is no evidence of a second, different gap due the AFM phase. Previously [30] we have shown that when two gaps are present in URu_2Si_2, as in the case of the c-axis conductivity, it is possible to see the characteristic change in the absorption due to this effect if the gap energies differ sufficiently. The absence of a second gap here strongly argues for a common gap-forming mechanism in the HO and AFM phases.

Figure 2 shows the AC conductivity of $URu_{2-x}(Fe,Os)_xSi_2$. In the paramagnetic phase, above the HO and AFM transition temperatures, the conductivity consists of a Drude peak and an incoherent continuum. As in the unsubstituted sample [30], the continuum develops a gap-like minimum at the phase transition. This minimum is unaltered in overall character between the HO and the AFM phases: both show a characteristic depletion of spectral weight in the gap region followed by a recovery in the frequency range immediately above the gap. The Drude peak that develops in the hybridization regime narrows but is otherwise unaffected by the emergence of the ordered phases. The principal effect of Os and Fe substitution is an increase in the energy of the gap, in tandem with the increase in transition temperature.

We can characterize the gap in the electronic density of states at the Fermi level Δ using the method described in reference [30] for the parent material, giving a reasonable estimate for the size of the gap and its temperature evolution. Results of this analysis are shown in Table 1. While the absolute value for the energy gap is somewhat model-dependent, we estimate the relative accuracy of the gap values between samples to be ±0.2 meV. The ratio $2\Delta/k_BT_0$, where T_0 is the transition temperature to the ordered phase (HO or AFM), has two values, a lower value of 4.2 for the parent compound and small Fe substitution and a somewhat higher value of 5.2 in the more heavily-substituted AFM phase. The charge gap closely tracks the transition temperature in both the AFM and HO phases, regardless of whether Fe or Os is used to induce antiferromagnetism. In particular, the value of

Fe	Δ (meV)	T_0 (K)	$2\Delta/k_BT_0$	phase
x = 0	3.2	17.5	4.2	HO
x = 0.05	3.3	18.2	4.2	HO/AFM
x = 0.1	3.4	18.5	4.3	HO/AFM
x = 0.3	5.1	23	5.2	AFM
Os	**Δ (meV)**	**T_0 (K)**	**$2\Delta/k_BT_0$**	**phase**
x = 0	3.2	17.5	4.2	HO
x = 0.1	4.4	19.5	5.2	AFM
x = 0.2	5.1	23	5.2	AFM
x = 0.3	6.6	29	5.3	AFM

TABLE I. Gap values for the various levels of substitution by Fe and Os. The gap and the critical temperature increase monotonically in tandem with substitution. T_0 was determined from both resistivity and SQUID magnetization measurements. The phase of the x=0.05 and x=0.1 samples with Fe substitution may be a mix of HO and AFM (see reference [25] for a discussion of the phase diagram).

$2\Delta/k_BT_0$ has nearly the same value deep in the AFM phase for both Fe and Os substitution. This implies that the AFM phase is the same for all samples and is not specific to Fe or Os, in agreement with μSR studies of the two systems [26].

It is worth comparing these results to those obtained by other techniques in the antiferromagnetic phase. Resistivity measurements on $\mathrm{URu_2Si_2}$ performed under pressure by Jeffries *et al.* [31] and specific heat measurements with Fe substitution by Das *et al.* [25] suggest that, as the transition temperature rises, the gap in the electronic excitations remains constant in the HO phase, then rises to higher values in the AFM phase. In contrast, as the table shows, our measurements clearly demonstrate that the gap tracks the rising transition temperature in both the HO and AFM phases.

We now turn to the excitations in the paramagnetic normal state above the ordered HO and AFM phases. Below 70 K, the conductivity in the 5 meV to 40 meV region decreases monotonically with decreasing temperature forming the so-called “hybridization gap” [32]. The spectral weight lost in the hybridization gap is transferred to much higher frequencies [33, 34] while in contrast both HO and AFM phases shift their spectral to a new hump feature *immediately* above the gap. Another common feature of the HO and AFM phases is the “arrested hybridization”. In both phases the hybridization gap stops changing below the HO/AFM transition temperature.

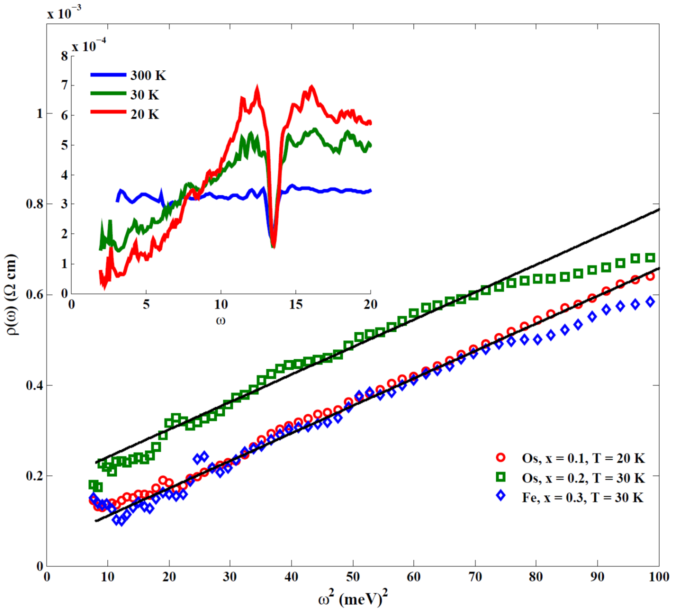

FIG. 3. The optical resistivity is linear when plotted against the square of the frequency. The closer to the transition the temperature at which $\rho(\omega)$ is measured, the higher in frequency the linear fit is valid. In all samples, regardless of the temperature of the transition or whether it was to an AFM or HO phase, the scattering is quadratic frequency immediately above the transition. The same behavior is seen in the parent compound, shown as an inset, which has linear scattering at 30 K that becomes quadratic closer to T_0. As the transition temperature rises with substitution, the temperature at which Fermi liquid behavior appears rises as well.

Figure 3 shows the AC resistivity as a function of ω^2 for the substituted compounds at temperatues just above the phase transition to the ordered state. It is linear in the low frequency regime $\omega \lesssim 8.5$ meV, indicating quadratic dependence of the scattering rate on frequency. This is true at temperatures well above the range where quadratic scattering rates are observed in the parent compound, indicating that $\mathrm{URu_{2-x}(Fe,Os)_xSi_2}$ is a coherent (though anomalous [32, 35], see below) Fermi liquid in the normal state in a narrow temperature range above the transition regardless of whether the transition is to the HO or the AFM phase.

The unsubstituted compound is shown as an inset to Figure 3. At 30 K the scattering rate varies linearly with frequency, *i.e.* it is non Fermi liquid like. At 20 K coherence has developed with $1/\tau < \omega$ and the scattering rate varies as ω^2. We show that with substitution the same behavior obtains: the ordered state, regardless of the order parameter, always emerges from a Fermi liquid precursor. This fact is not immediately apparent from transport measurements alone as the Fermi liquid temperature range is too narrow to establish a conventional T^2 dependence; it is only by looking at the optical scattering rate that it becomes clear that this must be the case.

For a Fermi liquid, in addition to the ω^2 frequency dependence, one also expects a T^2 temperature dependence of the resistivity. It was shown that the full resistivity is given by [36, 37]:

$$\rho(\omega, T) = C(\omega^2 + b\pi^2T^2) \tag{1}$$

where the value of the coefficient C depends on the band

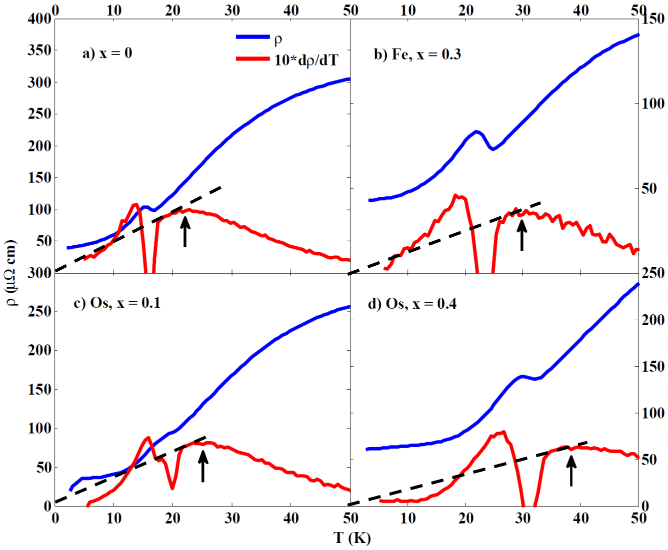

FIG. 4. The DC resistivity and its first derivative for $\mathrm{URu}_{2-x}(\mathrm{Fe,Os})_x\mathrm{Si}_2$. The transition at T_0 to the ordered state is marked by a sudden sharp minimum in the resistivity. The resistivity of the parent compound has the same hallmarks as that of the substituted material. As the transition is approached from above the derivative reaches a maximum indicated by arrows in the figure, that always precedes the transition. The effect of substitution is to move the whole structure to higher temperatues preserving its overall features. The dashed line denotes Fermi liquid behavior where $d\rho(T)/dT = 2AT$.

structure but $b = 4$ for umklapp scattering [37] independent of the details of a particular material. It was pointed out recently that for many strongly correlated systems the b coefficient varied from 1.0 up to 2.5 and in particular for $\mathrm{URu}_2\mathrm{Si}_2$ it had a value of $b = 1.0$ in a narrow range of temperatures above the hidden order transition [32]. Maslov and Chubukov showed that this anomalous behavior can be the result of resonant elastic scattering [37]. In the case at hand the scattering centers would be the unhybridized f electrons.

Figure 4 shows the DC resistivity and its temperature derivative for $\mathrm{URu}_{2-x}(\mathrm{Fe,Os})_x\mathrm{Si}_2$. The resistivity bears many of the hallmarks of the resistivity of the parent compound [32], with the transition marked by the same peak like feature that shifts up in temperature with x. The first derivative of the resistivity is characterized by a broad asymmetric peak above the transition. The transition itself is signaled as a sudden sharp drop in the derivative to negative values. With increasing x this pattern shifts upwards in temperature. It is noteworthy that the turnover in the derivative has the same character in samples with a HO transition and those with an AFM transition. This is analogous to the behavior of the resistivity under pressure [31].

Because the temperature range of Fermi liquid behavior is the narrow region between onset of coherence and the transition to the ordered state, we cannot use the usual method of plotting $\rho(T) = AT^2$ to determine the coefficient A and then from it b. Instead we adopt the following procedure. Assuming that Eq. 1 holds we can determine C from the slope of the frequency dependence as shown in Fig. 3. To find A we draw a straight line from the experimental resistivity derivative line to the origin as shown in Fig. 4b (dashed line), in effect assuming that $d\rho/dT = 2AT$ where, in our notation, $A = Cb\pi^2$. Using this procedure we find that in the normal state at 19 K $b = 1.1$ in the parent compound, while for the Fe $x = 0.3$ material, just above the AFM transition at 30 K, $b = 1.35$. So, in both materials, above the transition, there is a coherent Fermi liquid with anomalous b. At the same temperature, in the parent material, the frequency dependence is not Fermi liquid like and the transport is incoherent, *i.e.* $1/\tau > \omega$. Thus we conclude that substitution with Fe and Os moves both the second order transition temperature and the region where we observe coherent ω^2 Fermi liquid behavior in concert to higher temperatures.

This observation indicates that regardless of the nature of the transition (AFM or HO) or the temperature at which it occurs, the dominant scattering mechanism for the charge carriers is due to scattering of coherent quasiparticles from resonant impurities. This was previously shown [32] to be the case for the parent material. We conclude that the emergence of this anomalous Fermi liquid scattering is a precondition for the occurrence of the ordered state. Coherence and a well developed Femi surface are necessary conditions for a nesting induced density wave. What we have *not* observed in the normal state in $\mathrm{URu}_2\mathrm{Si}_2$ is scattering by discrete bosonic excitations; such excitations would be characterized by a distinct onset of scattering rather than the smooth ω^2 dependence that we observe. (Such as for example the 41 meV magnetic resonance in the cuprates [38]).

In summary, we have studied two ordered phases of $\mathrm{URu}_2\mathrm{Si}_2$ spectroscopically: the hidden order phase and the antiferromagnetic phase. The two phases show few differences other than an overall smooth increase in the gap and the transition temperature with substitution of Fe and Os. In the ordered states the gap and the transfer of spectral weight are characteristic of density waves and consistent with a partial gapping scenario [5]. The normal states are also very similar: they are Fermi liquid like with a scaling factor $b \approx 1.0$ characteristic of a Fermi liquid dominated by resonant impurity scattering. Models that include nesting-induced density waves are consistent with our observations: efficient nesting is promoted by coherent well-defined Fermi surfaces.

We thank P. Coleman, G. Kotliar, D.L. Maslov, S.S. Lee, B.D. Gaulin, and A.M. Tremblay for helpful discussions. This work was supported by the Natural Science and Engineering Research Council of Canada and by the Canadian Institute for Advanced Research. The research at UCSD was supported by the U.S. Department of Energy, Office of Basic Energy Sciences, Division of Materials Sciences and Engineering under Grant No. DE-FG02-04ER46105 (sample synthesis) and the National Science Foundation under Grant No. DMR-1206553 (sample characterization). MJ acknowledges financial support by the Alexander von Humboldt foundation.

---

[*] Present address: State Key Laboratory of Surface Physics, Department of Physics, Fudan University, Shanghai 200433, China

[†] Present address: MPA-CMMS, Los Alamos National Laboratory, Los Alamos, New Mexico 87545, USA

[1] H. Amitsuka, M. Sato, N. Metoki, M. Yokoyama, K. Kuwahara, T. Sakakibara, H. Morimoto, S. Kawarazaki, Y. Miyako, and J. A. Mydosh, Phys. Rev. Lett. **83**, 5114 (1999).

[2] F. Bourdarot, A. Bombardi, P. Burleta, M. Enderlec, J. Flouquet, P. Lejay, V. M. N. Kernavanoisc, L. Paolasinib, M. Zhitomirskya, and B. Fak, Physica B **359-361**, 986 (2005).

[3] K. Matsuda, Y. Kohori, T. Kohara, H. Amitsuka, K. Kuwahara, and T. Matsumoto, Journal of Physics: Condensed Matter **15**, 2363 (2003).

[4] T. T. M. Palstra, A. A. Menovsky, and J. A. Mydosh, Phys. Rev. B **33**, 6527 (1986).

[5] M. B. Maple, J. W. Chen, Y. Dalichaouch, T. Kohara, C. Rossel, M. S. Torikachvili, M. W. McElfresh, and J. D. Thompson, Phys. Rev. Lett. **56**, 185 (1986).

[6] C. R. Wiebe, J. A. Janik, G. J. MacDougall, G. M. Luke, J. D. Garrett, H. D. Zhou, Y.-J. Jo, L. Balicas, Y. Qiu, J. R. D. Copley, Z. Yamani, and W. J. L. Buyers, Nature Phys. **3**, 96 (2007).

[7] A. F. Santander-Syro, M. Klein, F. L. Boariu, A. Nuber, P. Lejay, and F. Reinert, Nature Phys. **5**, 637 (2009).

[8] A. R. Schmidt, M. H. Hamidian, P. Wahl, F. Meier, A. V. Balatsky, J. D. Garrett, T. J. Williams, G. M. Luke, and J. C. Davis, Nature **465**, 570 (2010).

[9] P. Aynajian, E. H. da Silva Neto, C. V. Parker, Y.-K. Huang, A. Pasupathy, J. A. Mydosh, and A. Yazdani, Proceedings of the National Academy of Sciences **107**, 10383 (2010).

[10] E. Hassinger, G. Knebel, T. D. Matsuda, D. Aoki, V. Taufour, and J. Flouquet, Phys. Rev. Lett. **105**, 216409 (2010).

[11] K. Haule and G. Kotliar, Nat. Phys. **5**, 796 (2009).

[12] Y. Dubi and A. V. Balatsky, Phys. Rev. Lett. **106**, 086401 (2011).

[13] P. Chandra, P. Coleman, and R. Flint, Nature **493**, 621 (2013).

[14] P. S. Riseborough, B. Coqblin, and S. Magalhaes, Physical Review B **85**, 165116 (2012).

[15] T. Das, Physical Review B **89**, 045135 (2014).

[16] M. W. McElfresh, J. D. Thompson, J. O. Willis, M. B. Maple, T. Kohara, and M. S. Torikachvili, Phys. Rev. B **35**, 43 (1987).

[17] P. G. Niklowitz, C. Pfleiderer, T. Keller, M. Vojta, Y.-K. Huang, and J. A. Mydosh, Phys. Rev. Lett. **104**, 106406 (2010).

[18] H. Amitsuka, K. Matsuda, I. Kawasaki, K. Tenya, M. Yokoyama, C. Sekine, N. Tateiwa, T. Kobayashi, S. Kawarazaki, and H. Yoshizawa, Journal of Magnetism and Magnetic Materials **310**, 214 (2007).

[19] F. Bourdarot, S. Raymond, and L.-P. Regnault, Philosophical Magazine **94**, 3702 (2014).

[20] E. Hassinger, G. Knebel, K. Izawa, P. Lejay, B. Salce, and J. Flouquet, Physical Review B **77**, 115117 (2008).

[21] M. Nakashima, H. Ohkuni, Y. Inada, R. Settai, Y. Haga, E. Yamamoto, and Y. Onuki, Journal of Physics: Condensed Matter **15**, S2011 (2003).

[22] S. Elgazzar, J. Rusz, M. Amft, P. M. Oppeneer, and J. A. Mydosh, Nature Materials **8**, 337 (2009).

[23] P. M. Oppeneer, S. Elgazzar, J. Rusz, Q. Feng, T. Durakiewicz, and J. A. Mydosh, Phys. Rev. B **84**, 241102 (2011).

[24] N. Kanchanavatee, M. Janoschek, R. E. Baumbach, J. J. Hamlin, D. A. Zocco, K. Huang, and M. B. Maple, Phys. Rev. B **84**, 245122 (2011).

[25] P. Das, N. Kanchanavatee, J. S. Helton, K. Huang, R. E. Baumbach, E. D. Bauer, B. D. White, V. W. Burnett, M. B. Maple, J. W. Lynn, and M. Janoschek, Phys. Rev. B **91**, 085122 (2015).

[26] M. Wilson, A. Hallas, T. Medina, T. Munsie, G. Luke, T. Williams, S. Cheung, B. Frandsen, L. Liu, and Y. Uemura, in *APS Meeting Abstracts*, Vol. 1 (2015) p. 22005.

[27] N. Kanchanavatee, B. White, V. Burnett, and M. Maple, Philosophical Magazine **94**, 3681 (2014).

[28] J. R. Jeffries, N. P. Butch, B. T. Yukich, and M. B. Maple, Phys. Rev. Lett **99**, 217207 (2007).

[29] C. C. Homes, M. Reedyk, D. Cradles, and T. Timusk, Applied optics **32**, 2976 (1993).

[30] J. S. Hall, U. Nagel, T. Uleksin, T. Rõõm, T. Williams, G. Luke, and T. Timusk, Phys. Rev. B **86**, 035132 (2012).

[31] J. R. Jeffries, N. P. Butch, B. T. Yukich, and M. B. Maple, J. Phys. Cond. Matt. **20**, 095225 (2008).

[32] U. Nagel, T. Uleksin, T. Rõõm, R. P. S. M. Lobo, P. Lejay, C. C. Homes, J. Hall, A. W. Kinross, S. Purdy, T. J. Williams, G. M. Luke, and T. Timusk, Proceedings of the National Academy of Sciences **109**, 19161 (2012).

[33] W. T. Guo, Z. G. Chen, T. J. Williams, J. D. Garrett, G. M. Luke, and N. L. Wang, Phys. Rev. B **85**, 195105 (2012).

[34] J. S. Hall and T. Timusk, Phil. Mag. **94**, 3760 (2014).

[35] M. R. Movassagh, Master's thesis, McMaster University (2014).

[36] R. Gurzhi, Soviet Physics JETP **35**, 673 (1959).

[37] D. L. Maslov and A. V. Chubukov, Phys. Rev. B **86**, 155137 (2012).

[38] J. Hwang, T. Timusk, E. Schachinger, and J. Carbotte, Physical Review B **75**, 144508 (2007).

Chapter 9

Disscussion and concluding remarks

The hidden order remains as elusive as ever and just as intensively investigated. The phenomenology is very well studied, to the point that it is becoming increasingly challenging to think of new experiments to perform. The rapid proliferation of new models testifies to the controversy around the order parameter and the nature of the ordering.

In the years that I have been studying this material, more experiments and theories have been put forward that have informed one another and that have had bearing on the current understanding of the hidden order transition. On the theoretical side, the current controversy primarily surrounds whether the electrons should be considered localized or fully itinerant; DMFT calculations are usually predicated on the idea that the electrons are fully hybridized and delocalized. This view is supported primarily by Mydosh and Oppeneer (Mydosh and Oppeneer, 2014), who point the the absence of crystal field effects as evidence for delocalization. They have also been able to show that the g-factor anisotropy that is often pointed to as evidence for localization can be reproduced in DMFT calculations.

On the other hand, the argument for localization of the *f* electrons is that the g-factor anisotropy is difficult to account for in purely itinerant models. The absence of any magnetism, likewise, is difficult to account for in itinerant models, which will tend to form density waves or other long-range orders. The localized models that have received the most attention recently are those of Dubi and Balatsky (Dubi and Balatsky, 2011), Chandra, Flint, and Coleman (Chandra *et al.*, 2013), and Haule and Kotliar (Haule and Kotliar, 2009). None of these has unequivocally established itself as the prime candidate for hidden order, however, and each has problems: Haule and Kotliar's proposal relies on crystal field effects which haven't been observed, and Chandra *et al.* suggest there should be an in-plane magnetic moment that has been ruled out experimentally.

Experimentally, the situation is no less murky despite the enormous amount of information. The results of Park *et al.* (Park *et al.*, 2012) are now widely accepted as spurious (though not universally), but even without worrying about hidden order onset above the transition temperature there is plenty to wonder about. The similarity of the Fermi surface in the HO and AFM states begs the question of what it is that causes one to have long range magnetic order but suppresses it in the other state. The question of symmetry breaking in the HO state is still open, with torque magnetometry, x-ray diffraction, and polar Kerr effect measurements all weighing in with varying conclusions.

The situation as it relates to optics is rather more clear. The existence of strong incommensurate fluctuations (Wiebe *et al.*, 2007) which become gapped at the hidden order transition are a strong sign of Fermi surface nesting at the incommensurate wave vector. DMFT calculations (Elgazzar *et al.*, 2009) reach the same conclusion. STM (Schmidt *et al.*, 2010) and ARPES (Santander-Syro *et al.*, 2009) give good indications of the behaviour of the electronic structure. Earlier optical studies have established the basic structure of the hidden order gap (Bonn *et al.*, 1988).

The observation that the heavy mass of the carriers is much smaller than the specific heat effective mass is only one of several areas in which optics and specific heat disagree. The specific heat measurements suggest a much larger value for the HO gap of 12 meV, which cannot be reconciled with optical measurements. The conservation of the Drude weight also indicates that the effective mass is constant throughout the hybridization, which suggests that the coherent state is not fully established above the HO transition. The suggestion that hybridization becomes complete only at the transition is therefore in agreement with our data, although the gap that emerges in the HO state is very different in character from the hybridization gap above the transition.

The hybridization itself is the subject of considerable interest and the search for precursor states has led to intense investigation. In contrast with the data of Park *et al.* and Levallois *et al.* (Levallois *et al.*, 2011) we do not detect any evidence for the onset of a precursor state in the hybridization gap regime. This effectively rules out the idea that changes in the electronic structure related to the development of a pseudogap are driving the hidden order state. It does not exclude the possibility of order parameter fluctuations above the transition, but the pseudogap created by the hybridization and the onset of coherent scattering is not a signature of it.

Analysis of the spectral weight associated with the hybridization gap shows the energy range over which spectral weight is lost and the energy at which it is recovered. The distinctive structure, of loss of spectral weight across a broad low-frequency range above the Drude peak with recovery at much higher frequencies, is very different from the gap that occurs in the hidden order state. The different gap structures point to different gapping mechanisms, suggesting that while the hybridization may not be complete until the transition occurs there are nevertheless different mechanisms responsible for the formation of the two gaps. This argues against models of hybridization waves and other hybridization based hidden order parameters.

The anisotropy of the hidden order gap and the presence of a second, smaller gap in the *c* axis conductivity shows that different parts of the Fermi surface respond to the onset of order in different ways. Subsequent ARPES measurements (Boariu *et al.*, 2013) were able to identify two different sections of the Fermi surface with different gaps as well, and showed that they were unrelated to the hybridization. The relationship between the different gaps and their magnitudes neatly tied together some of the different measurements and different estimates of the gap values.

The temperature evolution of the gaps do not follow mean field theory, indicating that the gap in the electronic density of states is not related to the order parameter, or that it closes in a non-BCS-like fashion, or that the order parameter is non-BCS-like. The exact explanation for this is unclear. As there are different gaps with different magnitudes that all open at the same temperature, they clearly cannot all preserve the BCS relation $2\Delta = 3.53 k_B T_o$ and therefore it is not necessarily to be expected that the gap should close in a single-gap mean field manner, even if the energy gap does track the order parameter overall.

The fact that we were able to closely fit the optical conductivity using a Dynes model for the density of states is strong evidence that mean field theory is at least approximately appropriate for describing the electronic excitation spectrum. The models appropriate for a density wave, in particular, in which case I coherence factors are in evidence, argues that the BCS theory does describe the density of states in the hidden order state. The optical conductivity therefore appears to depict a density wave. Its absence from other measurement techniques is baffling given how accurate the density wave model is for the electronic spectrum.

The similarity of the gap structure, indeed the fact that it is identical, between the HO and AFM states makes the puzzle all the more confusing. It shows that the same mechanism gaps the Fermi surface in both the HO and AFM states, yet only one of these states possesses long range magnetic order. The characteristic hidden order gap structure is very different from the hybridization gap and persists long after the hidden order state has been destroyed and replaced by antiferromagnetism. The continued presence and gapping of the incommensurate magnetic excitation seen in neutron scattering likewise argues strongly for the close relationship between these phenomena in the HO and AFM states, suggesting that Fermi surface nesting is at the origin of the formation of the gap. The question of why this fails to produce a spin density wave in the HO state despite the clear optical signature of a density wave is a puzzle awaiting a solution, but one which future models of the HO state must address.

The hybridization is arrested at the hidden order transition, as the changes in the electronic structure that are characteristic of the hybridization pseudogap cease at the onset of the transition. As the transition is pushed to higher temperatures by substitution and even once the transition becomes antiferromagnetic, this remains true; hybridization ceases once hidden order or antiferromagnetism occur.

The Fermi liquid scattering that precedes the transition is only visible in spectroscopic measurements, as it occurs over a temperature range that is far too narrow to be convincing in transport measurements. The identification of a material in which optics provides the signature of Fermi liquid scattering rather than resistivity measurements suggests that other systems may require optical investigation in order to assess their Fermi liquidity. The scaling between the frequency and temperature dependent terms is anomalous, and this appears to be a generic feature of correlated electron systems. This demonstrates that electron-electron scattering cannot be responsible for the scattering of the carriers in these systems. Up until this point, ”Fermi liquid scattering”, ”quadratic temperature dependence”, and ”electron-electron scattering” have been used interchangeably; we have shown that this is no longer appropriate. The discovery that other scattering mechanisms can lead to a quadratic dependence of the scattering rate on both frequency and temperature was quite unexpected and the full implications of this finding are still being absorbed by the community.

The fact that Fermi liquid scattering precedes the transition even as the transition temperature rises, and even as the ordered state itself changes, is likewise wholly unexpected. The material seems to ”know” that it is about to undergo a phase transition several degrees above the actual transition temperature. The Fermi liquid scattering remains anomalous even as the temperature at which Fermi liquid behaviour begins to occur rises. Furthermore, the Fermi liquid scattering continues even when the transition has shifted to antiferromagnetism. This suggests one of three possible scenarios: either the Fermi liquid background is a necessary precondition for the order to occur and pressure/doping raises the temperature of onset, or a common mechanism is responsible for the scattering and the emergence of the ordered state, or fluctuations of the order parameter above the transition are causing anomalous Fermi liquid scattering to occur.

It is tempting to consider a scenario in which a common order parameter is responsible for both the HO and AFM states. Indeed, several of the theories proposed (Chandra *et al.*, 2015; Haule and Kotliar, 2009) include such a composite, complex order parameter which neatly ties the two states together. This data can be taken as support of this idea in broad terms, although it is not conclusive.

This work has contributed to a greater understanding of the mysterious hidden order state in URu_2Si_2. We have shown that an understanding of anomalous Fermi liquid scattering is both a generic problem in condensed matter physics and crucial to the particular case of hidden order in URu_2Si_2. We have also shown that the hidden order state is gapped in the manner characteristic of a spin density wave, and that the antiferromagnetic state has the same gap structure. The gap tracks the increased transition temperature but does not change in character.

Bibliography

Amato, A., Graf, M. J., de Visser, A., Amitsuka, H., Andreica, D., and Schenck, A. (2004). *J. Phys.: Condens. Matter*, **16**, S4403.

Amitsuka, H., Sato, M., Metoki, N., Yokoyama, M., Kuwahara, K., Sakakibara, T., Morimoto, H., Kawarazaki, S., Miyako, Y., and Mydosh, J. A. (1999). Effect of pressure on tiny antiferromagnetic moment in the heavy-electron compound uru$_2$si$_2$. *Phys. Rev. Lett.*, **83**, 5114–5117.

Aoki, D., Bourdarot, F., Hassinger, E., Knebel, G., Miyake, A., Raymond, S., Taufour, V., and Flouquet, J. (2009). *J. Phys. Soc. Jpn.*, **78**, 053701.

Aynajian, P., da Silva Neto, E. H., Parker, C. V., Huang, Y.-K., Pasupathy, A., Mydosh, J. A., and Yazdani, A. (2010). *PNAS*, **107**, 10383.

Boariu, F. L., Bareille, C., Schwab, H., Nuber, A., Lejay, P., Durakiewicz, T., Reinert, F., and Santander-Syro, A. F. (2013). *Phys. Rev. Lett.*, **110**, 156404.

Bonn, D., Garrett, J., and Timusk, T. (1988). Far-infrared properties of uru 2 si 2. *Physical review letters*, **61**(11), 1305.

Bourdarot, F., Bombardi, A., Burleta, P., Enderlec, M., Flouquet, J., Lejay, P.,

N. Kernavanoisc, V. M., Paolasinib, L., Zhitomirskya, M., and Fak, B. (2005). *Physica B*, **359-361**, 986.

Bourdarot, F., Hassinger, E., Raymond, S., Aoki, D., Taufour, V., Regnault, L.-P., and Flouquet, J. (2010). *J. Phys. Soc. Jpn.*, **79**, 064719.

Broholm, C., Kjems, J. K., Buyers, W. J. L., Matthews, P., Palstra, T. T. M., Menovsky, A. A., and Mydosh, J. A. (1987). *Phys. Rev. Lett.*, **58**, 1467.

Broholm, C., Lin, H., Matthews, P., Mason, T., Buyers, W. J. L., Collins, M., Menovsky, A. A., Mydosh, J. A., and Kjems, J. (1991). *Phys. Rev. B*, **46**(16), 12809.

Buhot, J., Masson, M.-A., Gallais, Y., Cazayous, M., Sacuto, A., Lapertot, G., and Aoki, D. (2014). *Phys. Rev. Lett.*, **113**, 266405.

Chandra, P., Coleman, P., and Flint, R. (2013). *Nature*, **493**, 621.

Chandra, P., Coleman, P., and Flint, R. (2015). *arXiv:1501.01281.*

Chatterjee, S., Trinckauf, J., Hänke, T., Shai, D. E., Harter, J. W., Williams, T. J., Luke, G. M., Shen, K. M., , and Geck, J. (2013). *Phys. Rev. Lett.*, **110**, 186401.

Cooper, S. L., Klein, M. V., Maple, M. B., and Torikachvili, M. S. (1987). *Phys. Rev. B*, **36**, 5743.

Dakovski, G. L., Li, Y., Gilbertson, S. M., Rodriguez, G., Balatsky, A. V., Zhu, J.-X., Gofryk, K., Bauer, E. D., Tobash, P. H., Taylor, A., Sarrao, J. L., Oppeneer, P. M., Riseborough, P. S., Mydosh, J. A., , and Durakiewicz, T. (2014). *Phys. Rev. B*, **84**, 161103.

Das, P., Baumbach, R., Huang, K., Maple, M., Zhao, Y., Helton, J., Lynn, J., Bauer, E., and Janoschek, M. (2013). *New J. Phys.*, **15**, 05303.

Das, P., Kanchanavatee, N., Helton, J. S., Huang, K., Baumbach, R. E., Bauer, E. D., White, B. D., Burnett, V. W., Maple, M. B., Lynn, J. W., and Janoschek, M. (2015). Chemical pressure tuning of uru$_2$si$_2$ via isoelectronic substitution of ru with fe. *Phys. Rev. B*, **91**, 085122.

Degiorgi, L. (1999). The electrodynamic response of heavy-electron compounds. *Reviews of Modern Physics*, **71**(3), 687.

Degiorgi, L., Ott, H., Dressel, M., Grüner, G., Geibel, C., Steglich, F., and Fisk, Z. (1995). *Physica B*, **206**, 441.

Degiorgi, L., Dressel, M., Schwartz, A., Alavi, B., and Grüner, G. (1996). *Phys. Rev. Lett.*, **76**, 3838.

Degiorgi, L., Anders, F., and Grüner, G. (2001). Charge excitations in heavy electron metals. *The European Physical Journal B-Condensed Matter and Complex Systems*, **19**(2), 167–170.

Dordevic, S., Basov, D. N., Dilley, N. R., Bauer, E. D., and Maple, M. B. (2001). *Phys. Rev. Lett.*, **86**, 684.

Dubi, Y. and Balatsky, A. V. (2011). *Phys. Rev. Lett.*, **106**, 086401.

Elgazzar, S., Rusz, J., Amft, M., Oppeneer, P. M., and Mydosh, J. A. (2009). *Nature Materials*, **8**, 337.

Fisher, R., Kim, S., Wu, Y., Phillips, N. E., McElfresh, M. W., Torikachvili, M. S., and Maple, M. B. (1990). *Physica B*, **163**, 419.

Grüner, G. (1988). The dynamics of charge-density waves. *Reviews of Modern Physics*, **60**(4), 1129.

Grüner, G. (1994). *Rev. Mod. Phys.*, **66**, 1.

Hall, J. S., Nagel, U., Uleksin, T., Rõõm, T., Williams, T., Luke, G., and Timusk, T. (2012). *Phys. Rev. B*, **86**, 035132.

Haraldsen, J. T., Dubi, Y., Curro, N. J., and Balatsky, A. V. (2011). *Phys. Rev. B*, **84**, 214410.

Hassinger, E., Knebel, G., Matsuda, T. D., Aoki, D., Taufour, V., and Flouquet, J. (2010). Similarity of the fermi surface in the hidden order state and in the antiferromagnetic state of uru$_2$si$_2$. *Phys. Rev. Lett.*, **105**, 216409.

Haule, K. and Kotliar, G. (2009). *Nat. Phys.*, **5**, 796.

Ito, T., Kumigashira, H., Takahashi, T., Haga, Y., Yamamoto, E., Honma, T., Ohkuni, H., and Ōnuki, Y. (1999). *Phys. Rev. B*, **60**, 13390.

Janik, J., Zhou, H., Jo, Y., Balicas, L., MacDougall, G., Luke, G., Garrett, J., McClellan, K., Bauer, E., and Sarrao, J. (2009). Itinerant spin excitations near the hidden order transition in uru2si2. *Journal of Physics: Condensed Matter*, **21**(19), 192202.

Jeffries, J. R., Butch, N. P., Yukich, B. T., and Maple, M. B. (2007). *Phys. Rev. Lett*, **99**, 217207.

Kambe, S., Tokunaga, Y., Sakai, H., Matsuda, T., Haga, Y., Fisk, Z., and Walstedt, R. (2011). *Science*, **331**, 430.

Kanchanavatee, N., Janoschek, M., Baumbach, R. E., Hamlin, J. J., Zocco, D. A., Huang, K., and Maple, M. B. (2011). *Phys. Rev. B*, **84**, 245122.

Kanchanavatee, N., White, B., Burnett, V., and Maple, M. (2014). *Philosophical Magazine*, **94**(32-33), 3681–3690.

Kung, H.-H., Baumbach, R. E., Bauer, E. D., Thorsmlle, V. K., Zhang, W.-L., Haule, K., Mydosh, J. A., and Blumberg, G. (2014). *arXiv:1410.6398*.

Lee, P., Rice, T., and Anderson, P. (1973). Fluctuation effects at a peierls transition. *Phys. Rev. Lett.*, **31**, 462.

Levallois, J., Levy-Bertrand, F., Tran, M. K., Stricker, D., Mydosh, J. A., Huang, Y.-K., and van der Marel, D. (2011). *Phys. Rev. B*, **84**, 4420.

Liu, M. K., Averitt, R. D., Durakiewicz, T., Tobash, P. H., Bauer, E. D., Trugman, S. A., Taylor, A. J., and Yarotski, D. A. (2011). *Phys. Rev. B*, **84**, 161101.

Lu, X., Ronning, F., Tobash, P. H., Gofryk, K., Bauer, E. D., and Thompson, J. D. (2012). *Phys. Rev. B*, **85**, 020402.

Luke, G., Keren, A., Le, L. P., Uemura, Y. J., Wu, W. D., Bonn, D., Taillefer, L., Garrett, J. D., and =Onuki, Y. (2004). *J. Phys.: Condens. Matter*, **16**, S4403.

Maple, M. B., Chen, J. W., Dalichaouch, Y., Kohara, T., Rossel, C., Torikachvili, M. S., McElfresh, M. W., and Thompson, J. D. (1986). *Phys. Rev. Lett.*, **56**, 185.

Martin, D. and Puplett, E. (1970). Polarised interferometric spectrometry for the millimetre and submillimetre spectrum. *Infrared Physics*, **10**(2), 105–109.

Maslov, D. L. and Chubukov, A. V. (2012). *Phys. Rev. B*, **86**, 155137.

Matsuda, K., Kohori, Y., Kohara, T., Kuwahara, K., and Amitsuka, H. (2001). Spatially inhomogeneous development of antiferromagnetism in uru 2 si 2: Evidence from s 29 i nmr under pressure. *Physical review letters*, **87**(8), 087203.

Matsuda, K., Kohori, Y., Kohara, T., Amitsuka, H., Kuwahara, K., and Matsumoto, T. (2003). The appearance of homogeneous antiferromagnetism in uru2si2 under high pressure: a 29si nuclear magnetic resonance study. *Journal of Physics: Condensed Matter*, **15**(14), 2363.

Matsuda, T., Aoki, D., Ikeda, S., Yamamoto, E., Haga, Y., Ohkuni, H., Settai, R., and =Onuki, Y. (2008). *J. Phys. Soc. Jpn.*, **77**, 362.

McElfresh, M. W., Thompson, J. D., Willis, J. O., Maple, M. B., Kohara, T., and Torikachvili, M. S. (1987). Effect of pressure on competing electronic correlations in the heavy-electron system uru_2si_2. *Phys. Rev. B*, **35**, 43–47.

Millis, A. J. and Lee, P. A. (1987). *Phys. Rev. B*, **35**, 3394.

Mydosh, J. A. and Oppeneer, P. M. (2011). *Rev. Mod. Phys.*, **83**, 1301.

Mydosh, J. A. and Oppeneer, P. M. (2014). Hidden order behaviour in uru2si2 (a critical review of the status of hidden order in 2014). *Philosophical Magazine*, **94**(32-33), 3642–3662.

Nagel, U., Uleksin, T., Rõõm, T., Lobo, R. P. S. M., Lejay, P., Homes, C. C., Hall, J., Kinross, A. W., Purdy, S., Williams, T. J., Luke, G. M., and Timusk, T. (2012). *PNAS*, **109**, 19161.

Okazaki, R., Shibauchi, T., H.J. Shi, Y. H., Matsuda, T., Yamamoto, E., Onuki, Y., Ikeda, H., and Matsuda, Y. (2013). *Phys. Rev. Lett*, **110**, 246406.

Oppeneer, P. M., Elgazzar, S., Rusz, J., Feng, Q., Durakiewicz, T., and Mydosh, J. A. (2011). *Phys. Rev. B*, **84**, 241102.

Palstra, T. T. M., Menovsky, A. A., van den Berg, J., Dirkmaat, A. J., Kes, P. H., Nieuwenhuys, G. J., and Mydosh, J. A. (1985). *Phys. Rev. Lett.*, **55**, 2727.

Palstra, T. T. M., Menovsky, A. A., and Mydosh, J. A. (1986). *Phys. Rev. B*, **33**, 6527.

Park, W. K., Tobash, P. H., Ronning, F., Bauer, E. D., Sarrao, J. L., Thompson, J. D., and Greene, L. H. (2012). *Phys. Rev. Lett.*, **108**, 246403.

Purdy, S. K. (2010). Master's thesis, McMaster University.

S. Barker, J., Halperin, B. I., and Rice, T. M. (1968). *Phys. Rev. Lett.*, **20**, 384.

Santander-Syro, A. F., Klein, M., Boariu, F. L., Nuber, A., Lejay, P., and Reinert, F. (2009). *Nature Phys.*, **5**, 637.

Schemm, E. R., Baumbach, R. E., Tobash, P. H., Ronning, F., Bauer, E. D., and Kapitulnik, A. (2015). *arXiv:1410.1479.*

Schmidt, A. R., Hamidian, M. H., Wahl, P., Meier, F., Balatsky, A. V., Garrett, J. D., Williams, T. J., Luke, G. M., and Davis, J. C. (2010). *Nature*, **465**, 570.

Shirer, K., Haraldsen, J., Dioguardi, A., Crocker, J., Roberts-Warren, N., Shockley, A., Lin, C.-H., Nisson, D., Cooley, J., Janoschek, M., Huang, K., Kanchanavatee, N., Maple, M., Graf, M., Balatsky, A., and Curro, N. (2012). *Phys. Rev. B*, **88**, 094436.

Shirer, K. R., J. T. Haraldsen and, . A. P. D., Crocker, J., apRoberts Warren, N., Shockley, A. C., Lin, C.-H., Nisson, D. M., Cooley, J. C., Janoschek, M., Huang, K., Kanchanavatee, N., Maple, M. B., Graf, M. J., Balatsky, A. V., and Curro, N. J. (2013). *Phys. Rev. B*, **88**, 094436.

Takagi, S., Ishihara, S., Saitoh, S., ichiro Sasaki, H., Tanida, H., Yokoyama, M., and Amitsuka, H. (2007). *J. Phys. Soc. Jpn.*, **76**, 033708.

Tateiwa, N., Matsuda, T. D., nuki, Y., Haga, Y., and Fisk, Z. (2012). *Phys. Rev. B*, **85**, 054516.

Tonegawa, S., Kasahara, S., Fukuda, T., Sugimoto, K., Yasuda, N., Tsuruhara, Y., Watanabe, D., Mizukami, Y., Haga, Y., Matsuda, T. D., Yamamoto, E., Onuki, Y., Ikeda, H., Matsuda, Y., and Shibauchi, T. (2014). *Nature Communications*, **5**, 4188.

Tripathi, V., Chandra, P., and Coleman, P. (2005). *J. Phys.: Condens. Matter*, **17**, 5285.

Tripathi, V., Chandra, P., and Coleman, P. (2007). *Nature Physics*, **3**, 78.

Villaume, A., Bourdarot, F., Hassinger, E., Raymond, S., Taufour, V., Aoki, D., and Flouquet, J. (2008). *Phys. Rev. B*, **78**, 012504.

Wiebe, C. R., Janik, J. A., MacDougall, G. J., Luke, G. M., Garrett, J. D., Zhou, H. D., Jo, Y.-J., Balicas, L., Qiu, Y., Copley, J. R. D., Yamani, Z., and Buyers, W. J. L. (2007). *Nature Phys.*, **3**, 96.

Wilson, M. N. and Luke, G. M. (2015). *In preparation.*

Yang, S.-H., Kumigashira, H., Yokoya, T., Chainani, A., Takahashi, T., Oh, S.-J., Sato, N., and Komatsubara, T. (1996). *J. Phys. Soc. Jpn.*, **65**, 2685.

Yokoyama, M., Amitsuka, H., K. Kenya, K. Watanabe, S. K. H. Y., and Mydosh, J. A. (2005). *Phys. Rev. B*, **72**, 214419.

Zhu, Z., Hassinger, E., Xu, Z., Aoki, D., Flouquet, J., and Behnia, K. (2009). *Phys. Rev. B*, **80**, 172501.